Influence of Mechanical Surface Treatments on the Water Droplet Erosion Performance of Ti-6Al-4V

Abdullahi Kachalla Gujba

A Thesis

In

The Department

Of

Mechanical and Industrial Engineering

Presented in Partial Fulfilment of the Requirements for the Degree of Doctorate in Philosophy (PhD) (Mechanical Engineering)

At

Concordia University

Montreal, Quebec, Canada

August 2016

CONCORDIA UNIVERSITY

School of Graduate Studies

This is to certify that the thesis prepared

By: Abdullahi K. Gujba

Entitled: Influence of Mechanical Surface Treatments on the Water Droplet Erosion Performance of Ti-6Al-4V

and submitted in partial fulfillment of the requirements for the degree of

DOCTOR OF PHILOSOPHY (Mechanical Engineering)

complies with the regulations of the University and meets the accepted standards with respect to originality and quality.

Signed by the final examining committee:

_____	Chair
Dr. Pouya Valizadeh	
_____	External Examiner
Dr. Vladimir Brailovski	
_____	External to Program
Dr. Saifur Rahaman	
_____	Examiner
Dr. Sivakumar Narayanswamy	
_____	Examiner
Dr. Mehdi Hojjati	
_____	Thesis Supervisor
Dr. Mamoun Medraj	

Approved by _____

Chair of Department or Graduate Program Director

August, 2016 _____

Dr.   , Dean

Faculty of Engineering & Computer Science

Abstract

Influence of Mechanical Surface Treatments on the Water Droplet Erosion Performance of Ti-6Al-4V

Abdullahi K. Gujba, PhD
Concordia University, 2016

In an attempt to enhance the water droplet erosion (WDE) performance of Ti-6Al-4V, a typical material used for compressor blades in gas turbines, this work studies the WDE performance/behaviour of reference untreated and surface treated Ti-6Al-4V. Existing literature suggests that WDE is likened to fatigue-like damage due to the continuous liquid impacts in a cyclic fashion. Also, the crack initiation and propagation have been found to significantly influence WDE behaviour similar to fatigue. It is known that induced compressive residual stresses from mechanical surface treatments retard crack initiation and further propagation and improves fatigue life. Hence, mechanical surface treatments might enhance WDE performance. For this reason, this work employed two mechanical surface treatments, laser shock peening (LSP) and ultrasonic nanocrystalline surface modification (UNSM), for the first time. UNSM treatment induced high levels of compressive residual stresses into the material. Variation in grain size was observed across the modified layer and the microhardness of the UNSM condition was enhanced significantly compared to the As-M condition. Although, significant amount of compressive residual stress was induced via LSP, the treatment showed mild increase in microhardness and no noticeable changes in the microstructure. This was attributed to the low level of cold work (about 5 %) during LSP processing. The WDE performance tests were conducted in a rotating disc rig in accordance with ASTM G73 standard. Influence of impact speed (between 150 and 350 m/s) on WDE performance was explored on two different sample geometries (T-shaped flat and airfoil). First, to understand the WDE

behaviour of the reference or as-machined (As-M) Ti-6Al-4V before applying surface treatments, its WDE behaviour was studied. In the second and third parts of this study, the WDE performance of UNSM treated *versus* As-M Ti-6Al-4V and LSP treated *versus* As-M Ti-6Al-4V conditions was investigated, respectively. WDE results showed that the T-shaped flat UNSM samples had enhanced WDE performance at speeds 250, 275 and 300 m/s compared with the As-M condition. At 350 m/s, both UNSM and As-M conditions showed similar performance due to diminished effect of the UNSM treatment. UNSM airfoils showed mild enhancement in the WDE performance at 300 m/s during the advanced stage compared with the As-M condition. At 350 m/s, no enhanced performance was observed for the UNSM airfoil condition. LSP showed little or no beneficial effect at any stage of the WDE performance at all tested impact speeds for the T-shaped flat geometry. However, LSP airfoil samples showed only mild enhancement in the WDE performance at 300 m/s during the advanced stage compared with the As-M condition. At 350 m/s, no enhanced performance was observed for the LSP airfoil condition. It was concluded that the influence of mechanical surface treatments on the WDE performance of material depends in general on the erosion test condition, sample geometry, materials' properties and microstructure. However, for the mechanical treatment to be effective in improving WDE performance, it has to cause surface hardening and grain refinement. Compressive residual stresses alone are not sufficient to enhance WDE performance especially for the T-shaped flat geometry. For the airfoil, the induced compressive residual stresses show limited beneficial effect in mitigating erosion at the advanced erosion stage. This is due to the fact that compressive residual stresses are through the thickness of the airfoil. This is the case observed at relatively low speed of 300 m/s. However, at 350 m/s where the test condition is severe, the induced compressive residual stresses show no beneficial effect on the airfoil geometry.

Dedication

To my parents, brothers and sisters for their love and support

To my friends who always encouraged me

To my beloved wife and her family for their love, care and patience

Acknowledgements

Table of Contents

List of Figures

xiii

xiv

List of Tables

List of Abbreviations

As-M	As Machined
ASTM	American Society for Testing and Materials
DR	Deep Rolling
ER$_{max}$	Maximum Erosion Rate
HEL	Hugoniot Elastic Limit
ER$_{inst}$	Instantaneous Erosion Rate
HF	Hydrofluoric Acid
HNO$_3$	Nitric Acid
LPB	Low Plasticity Burnishing
LSP	Laser Shock Peening
OM	Optical Macrographs
SEM	Scanning Electron Microscopy (Micrographs)
UNSM	Ultrasonic Nanocrystalline Surface Modification
WC	Tungsten Carbide
WDE	Water Droplet Erosion
XRD	X-Ray Diffraction

Chapter 1 : Introduction

One of the Achilles' heels of advanced materials found in the power generation industry is the erosion of the leading edge of the compressor blades. This chapter introduces the leading cause of this erosion damage. Also, the layout of this thesis is presented.

1.1. Problem statement

In the electric power generation industry, the gas turbine efficiency is an important issue and is directly affected by the ambient temperature [1]. Rise in ambient temperature especially during hot summer times leads to loss of gas turbine output power [2]. The lower turbine efficiency is attributed to a decrease in air density leading to a decrease in the intake air mass [3]. This consequently results in high electricity cost [4] and high CO_2 emissions [3]. In order to augment the turbine efficiency, the ambient temperature must be kept as low as possible. This can be achieved by using the inlet air fog cooling technique shown in Figure 1-1. In this technique, water droplets are sprayed into the inlet of the gas turbine compressor to cool down the intake air, thereby increasing the intake mass. The sprayed droplets reduce the temperature and increase in power out is realized [5]. This is a cost effective method however, the impacting water droplets cause a severe erosion damage problem to the leading edge of the rotating compressor blades especially at high speed [6]. The damage also causes vibrations which lead to loss of efficiency and fatigue issues for the entire turbine. This damage is usually termed as the "water erosion by impingement or water droplet erosion (WDE)". Figure 1-2 shows a typical gas turbine engine with the compressor blades before and after the erosion damage. With the current state of the problem, industries have invested huge amount of resources in order to mitigate this undesirable phenomenon.

Material such as Ti-6Al-4V has been identified as prone to WDE phenomenon despite its remarkable physical and mechanical properties. For example, Figure 1-3 shows a real-life compressor blade damage caused by WDE.
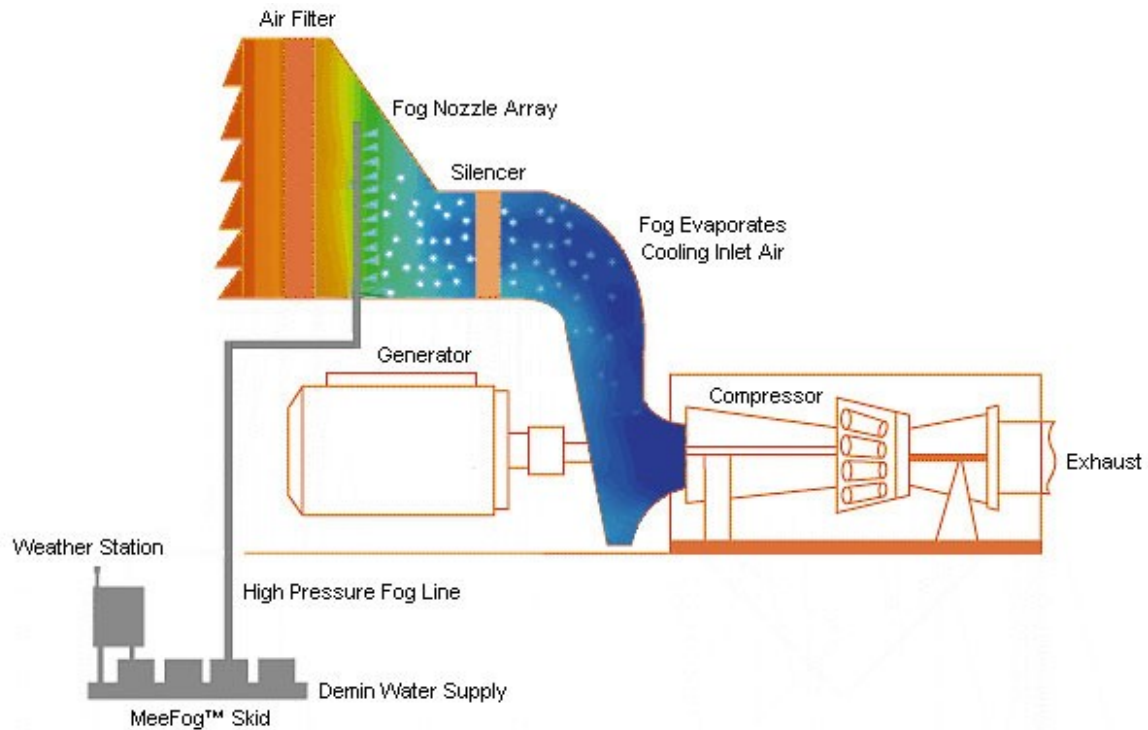
Figure 1-1: Schematic illustration of fogging system. Courtesy of Mee Industries
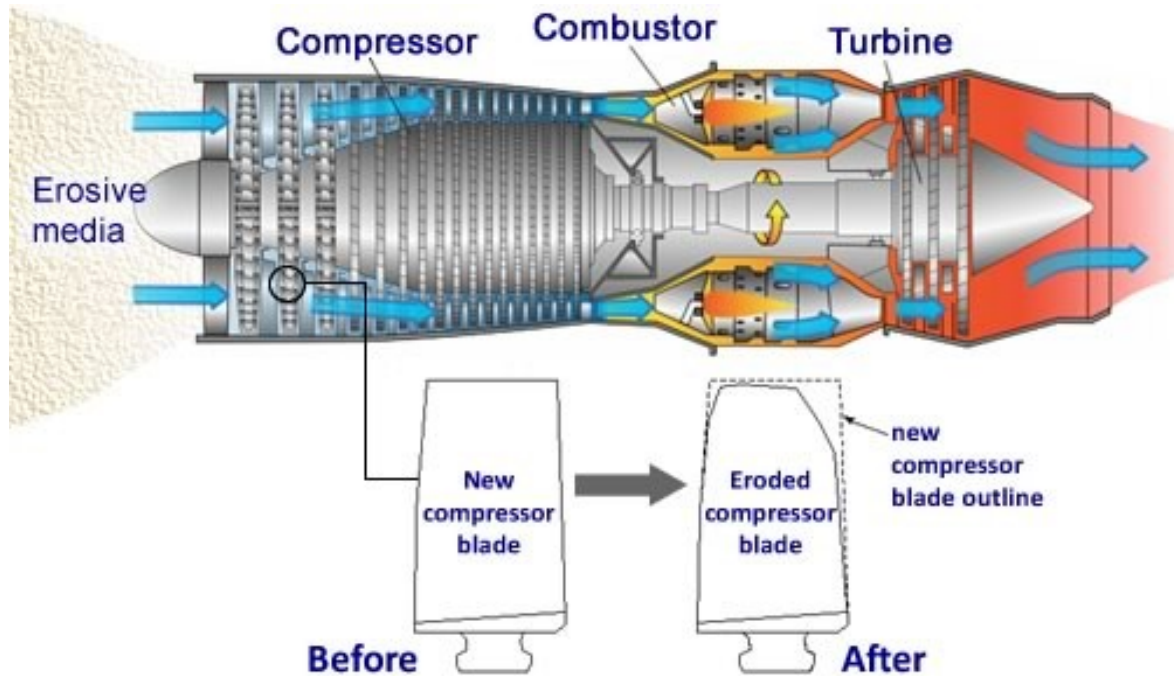
Figure 1-2: Gas turbine engine showing compressor blades before and after erosion damage. Courtesy of MSD Coatings Technologies Co.

Several surface treatment techniques such as surface coatings, nitriding, laser surface modifications have shown improvements in the WDE performance of Ti-6Al-4V. The

enhancements were attributed to different materials' properties such as hardness, toughness, ultimate resilience, work hardening rate and true stress at fracture. However, no single parameter has successfully been linked to the improved WDE performance of materials and there are still challenges that exist with the applied surface modifications such as presence of surface defects and microcracks. This shows that more investigations are still needed for better understanding of the erosion damage as well as to identify the best methods/techniques that can be employed to mitigate such damage.
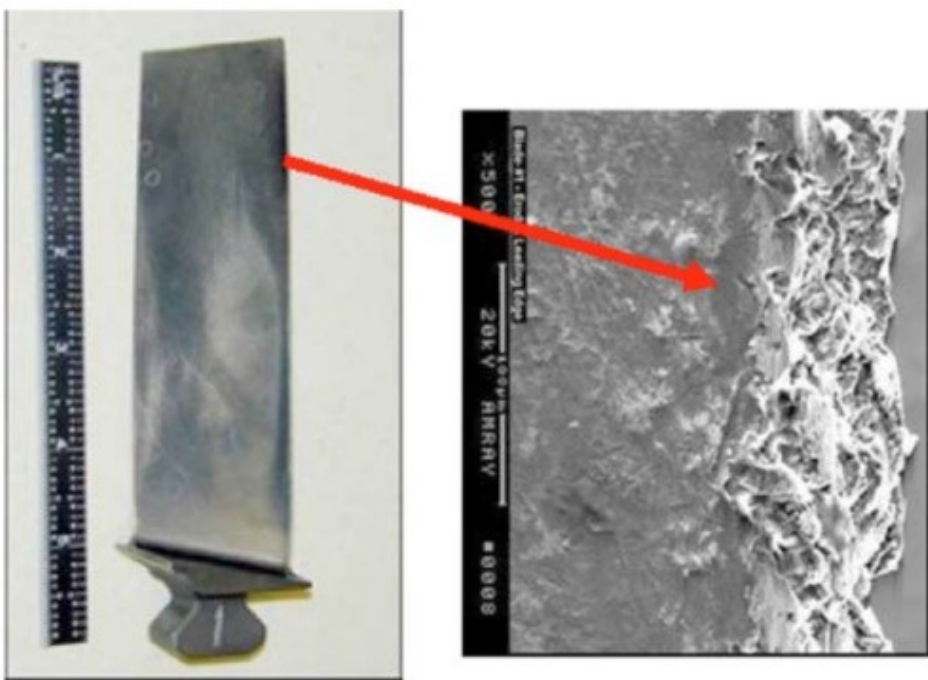
Figure 1-3: Water droplet erosion damage of compressor blade in LM6000 sprint gas turbine. Courtesy of General Electric.

1.2. Thesis layout

In this section, the thesis layout is outlined. Based on the approach followed in this research, the entire thesis is composed of six chapters. It is worth noting that the thesis is a manuscript based thesis containing three journal articles. Chapter 1 outlines the problem statement which is the erosion of the leading edge of compressor blades in gas turbines. Chapter 2 reviews the WDE phenomenon and a case study on Ti-6Al-4V which is the common compressor blade material is reviewed. The chapter also discusses some of the

potential methods used in mitigating the erosion. In the same chapter, mechanical surface treatments, LSP and UNSM processes, are reviewed. Research motivations and objectives are highlighted in relation to the literature findings and current work, respectively. In Chapter 3, the first article on water droplet erosion behaviour of Ti-6Al-4V and mechanisms of material damage at the early and advanced stages is presented. Chapter 4 presents the second article on the effect of ultrasonic nanocrystalline surface modification on the water droplet erosion performance of Ti-6Al-4V. In chapter 5, the third article addresses the water droplet erosion performance of laser shock peened Ti-6Al-4V. Finally, chapter 6 summarizes the contents and contributions in the present work and also, recommendations for future research are highlighted. For additional information regarding the entire thesis work, appendices are provided.

Chapter 2 : Literature Review and Research Motivations

Water droplet erosion of compressor blades of gas turbines is reviewed in this chapter. The causes and different stages of the erosion damage are reported. WDE behaviour of Ti-6Al-4V, a typical compressor blade material is presented. The need for more research work is emphasized based on the literature findings. Potential surface treatments employed to combat WDE are highlighted with specific emphasis on mechanical surface treatments on Ti-6Al-4V.

2.1. Water droplet erosion (WDE) and its causes

WDE is the progressive loss of material from a solid surface due to accumulated impacts by liquid droplets [7]. WDE is a complex phenomenon that existed for considerable long period of time and the reason for this is the number of parameters involved during the erosion process. These parameters include: impact speed, impact angle, droplet size, droplet density, frequency of impacts, liquid film formation, mechanical properties and conditions of the target material. More information on the influence of WDE parameters such as droplet size, impact speed, impact angle have been reported in [8,9]. WDE damage is predominantly caused by two main factors; (1) the high pressure exerted by the water droplet on the exposed area of the solid surface and (2) the radial liquid flow (lateral jetting) along the surface at high speed, which occurs after the initial droplet pressure lessens [10]. Figure 2-1 shows a typical droplet impact and its radial outflow (lateral jetting). The high pressure is usually termed as "water hammer pressure". The water hammer pressure is the induced pressure exerted by the "arrested" liquid droplet on the solid surface. This is an important factor that influences the surface damage especially at the incubation stage [11]. According to Heymann [12,13], this pressure can be considerably higher than the yield strength of many alloys especially at high impact speeds. Due to the continuous liquid impacts, the hammer pressure and lateral jetting lead to the formation of compression and shear waves (stress waves). The phenomenon of compression and shear waves is also paramount in understanding the erosion damage.
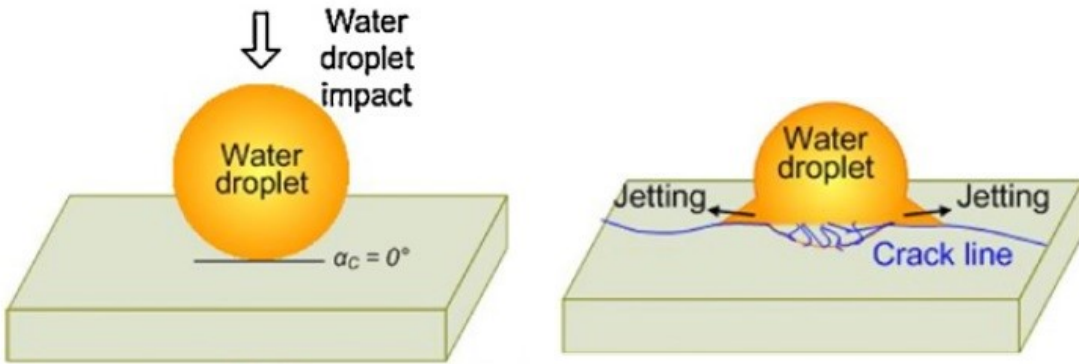
Figure 2-1: Water droplet impact and the radial outflow (lateral jetting) [14].

According to the elastic wave theory of solids [15], "when an impulse loading acts on a solid surface, a compression and a shear wave are generated in the bulk solid and on the surface, a Rayleigh surface wave is generated" [16]. As the compression wave travels through the solid, shear wave is formed. The shear wave offsets the stresses caused by the compression wave [16]. In water droplet impacts, the liquid impact causes the compression wave while the liquid lateral jetting causes the shear wave especially during advanced stage of water erosion damage. This is schematically shown in Figure 2-2. Also, at high impact speeds, the magnitude of these waves is high, causing significant damage. The effects of the compression and shear waves in understanding the mechanisms of material damage during erosion process have been addressed in this research.

The continuous impacts and lateral jetting reveal several damage features depending on the erosion damage stage, nature of material and most importantly the erosion condition. Based on the literature findings, typical WDE damage features and their possible cause(s) are summarized in Table 2-1. It should be noted that erosion damage features result from synergistic effects; however, only the main causes are highlighted here. The different stages of the erosion damage are discussed in the following section.
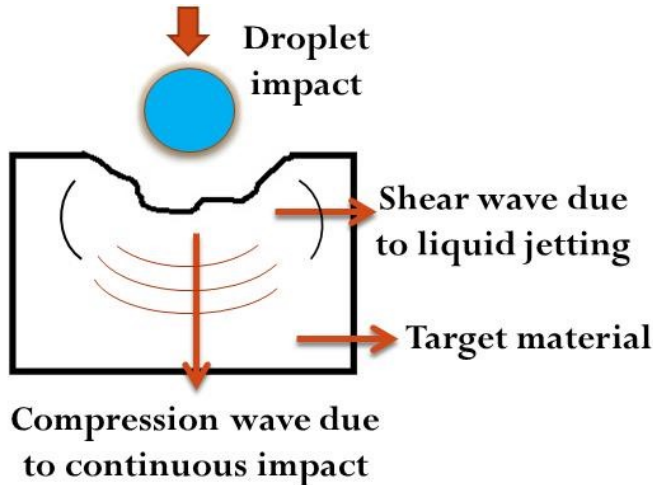
Figure 2-2: Schematic illustration of compression and shear waves during droplet impacts.

Table 2-1: Typical WDE damage features and their cause(s)

Erosion Features	Main Cause(s)	References
Surface asperities	Impact and liquid lateral jetting	[17,18]
Surface micro-cracks	Water hammering and stress waves	[11]
Surface depressions	Hydraulic pressure caused by droplet impacts	[17,19–23]
Internal or Sub-surface cracks	Interaction of the transmitted and reflected stress waves	[11]
Surface slip bands	Shear stress waves	[11]
Fatigue striations	Repeated droplet impacts in a cyclic fashion	[9,11]
Material folding and upheaval	Shear stress waves from the lateral jetting	[11]
Hydraulic penetration	Continuous liquid impact into the existing pits or craters	[11,24–27]
Side wall cracking	Liquid lateral jetting	[9,28]
Inter/transgranular cracking	Repeated impacts causing interaction between transmitted and reflected waves	[9,11,28]

2.1.1. Stages of WDE damage

Due to the time dependence of the erosion damage, different stages as shown in Figure 2-3 have been reported [12]. Figure 2-3a shows the cumulative erosion *versus* cumulative exposure duration, while Figure 2-3b shows the instantaneous erosion rate *versus* the

cumulative exposure duration. The different stages have been described as: A – the incubation stage during which little or no mass loss is observed, although surface roughening and metallurgical changes might be seen; B - the acceleration stage where the erosion rate increases up to a maximum; C – the maximum erosion stage where the erosion is at its peak and sometimes, it is reported as a single number; D – the deceleration or attenuation stage during which erosion rate is declining to a fraction of maximum erosion rate. Often, the fraction is ¼ to ½ of the maximum erosion rate; lastly, E – the terminal or final steady stage during which the rate remains constant.
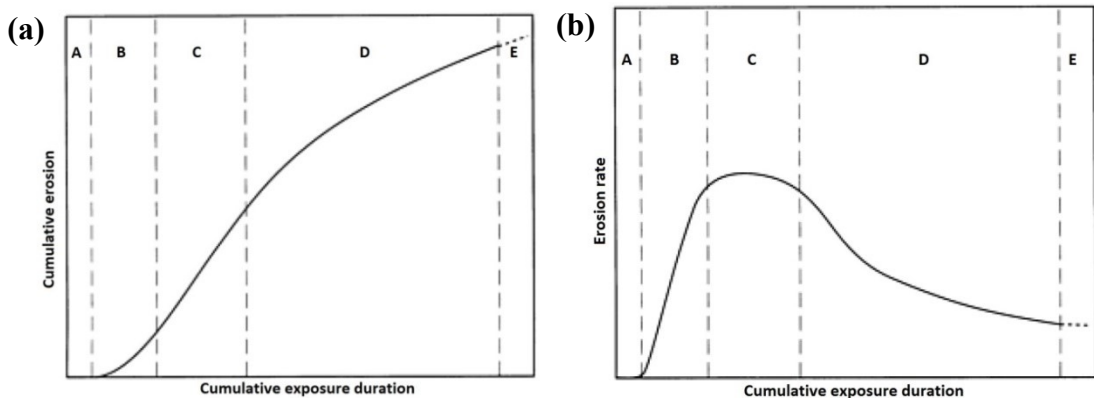
Figure 2-3: Characteristic erosion-time curves showing different stages on (a) cumulative erosion *versus* cumulative exposure duration and (b) instantaneous erosion rate *versus* the cumulative exposure duration [12].

The shape of erosion curves shown in Figure 2-3 depends on the target material and erosion conditions [29]. For instance, material with a well-behaved erosion curve has an S-shaped erosion curve with distinct erosion stages [29]. These characteristic curves are further affected by surface roughness [17,30], surface properties, microstructure [10], geometry [30], combination of impact speed and droplet size [30]. The next section discusses how these parameters affect the WDE behaviour of Ti-6Al-4V.

2.2. Factors affecting WDE behaviour of Ti-6Al-4V

WDE behaviour of Ti-6Al-4V (ASTM B265, Grade 5) alloy, a typical material for compressor blades in gas turbines has been studied in the literature. Different facilities, test

parameters and surface conditions have been employed in order to investigate the WDE behaviour of Ti-6Al-4V.

2.2.1. Surface roughness

It has been reported that the presence of surface asperities or irregularities prior to erosion test accelerates the erosion initiation [30]. Kirols *et al.* [17] studied the effect of initial surface roughness on the WDE behaviour of Ti-6Al-4V. Ti-6Al-4V samples with average initial surface roughness values (Ra) of 0.30, 0.12 and 0.04 μm were tested. During WDE tests, impact speed of 300 and 350 m/s and droplet size of 464 μm were employed. Figures 2-4a and b show their [17] WDE curves.
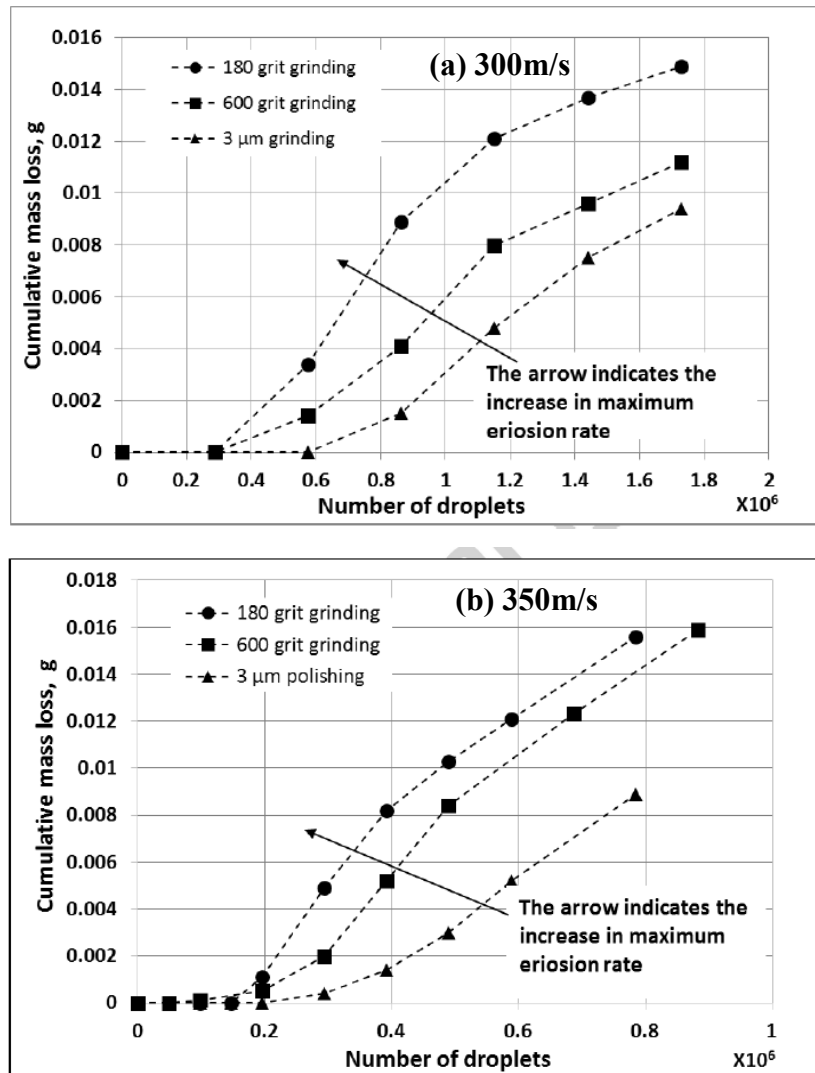
Figure 2-4: WDE behaviour of Ti-6Al-4V having three surface conditions tested at (a) 300 m/s and (b) 350 m/s using 464 μm droplet size [17].

From Figures 2-4a and b, it can be seen that merely polishing the surface prior to WDE tests delayed the erosion initiation and decreased the maximum erosion rates. They [17] studied the effect of surface roughness using only two impact speeds (300 and 350 m/s). More erosion tests are still needed at a wide range of impact speeds in order to have a full understanding of the effects of surface roughness. Also, monitoring the effect of initial surface roughness on various surface treatments and substrate materials prior to testing is paramount. In the current work, much attention has been given to the aforementioned points. For instance, the surface roughness of treated and untreated samples was similar prior to testing. This provides a better understanding of the influence of surface treatments on WDE behaviour.

2.2.2. Impact speed

Impact speed is one of the most important parameters that influence the WDE behaviour of Ti-6Al-4V. For instance, from Figures 2-4a and b, reducing the impact speed from 350 to 300 m/s delayed erosion initiation and reduced the erosion rate. In another study, Kamkar [9] reported the influence of impact speed on the WDE behaviour of Ti-6Al-4V. Impact speeds of 250, 300 and 350 m/s were employed. Figure 2-5 shows the cumulative mass loss *versus* impingement number. Also, it can be seen in Figure 2-5 that increase in impact speed corresponds to faster erosion initiation and greater erosion rate. However, in this work [9], x-axis was not represented accurately because the number of droplets impacting the sample was not taken into account. Instead, the number of impingement is simply taken as the number of sample rotations. Thus, the information presented in [9] underestimates the number of impingements to erosion initiation. More information regarding the number of droplets impacting the sample is needed for better understanding and representation of test data. This has been addressed in the current research through the use of a high speed camera in order to capture the number of droplets impacting the surface.
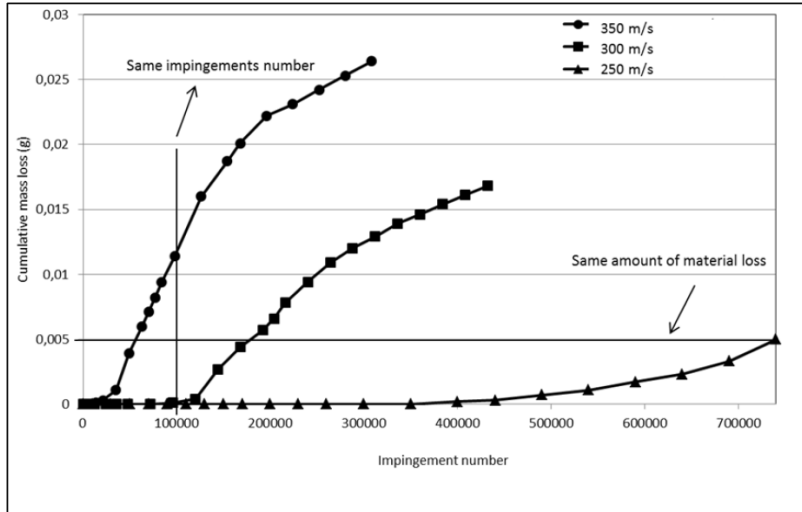
Figure 2-5: Cumulative mass loss *versus* impingement number [9].

Gerdes *et al.* [31] studied the WDE behaviour of Ti-6Al-4V compared with 12% Cr hardened steel. A rotating arm apparatus was used and three water streams were introduced parallel to specimen surface. They [31] reported the WDE behaviour for both materials at 300, 400 and 500 m/s impact speeds, as shown in Figure 2-6. From this figure, it is evident that at relatively low speed of 300 m/s, both materials have similar water erosion behaviour as compared to those tested at higher speeds of 400 and 500 m/s. At higher speeds, 12% Cr hardened steel showed better WDE behaviour compared to Ti-6Al-4V. Again, in this work [31], the number of impingements was not defined and initial surface roughness was not mentioned. Furthermore, information regarding initiation time and erosion rate were not reported. These details are needed for better interpretation of the observed WDE behaviour as recommended by ASTM standard [29]. In this research, guidelines in the standard [29] has been used for the erosion testing and the interpretation of test data. Also, testing at a wide range of impact speed is paramount. For instance, test at 250 m/s might reveal different WDE behaviour for both materials.

Based on the works in [9,17,31], no information was provided regarding the first threshold speed/velocity. This is the speed below which no apparent damage is seen. This threshold speed is often neglected in the literature due to the fact that a narrow range of

11

impact speeds is employed. In order to capture the threshold speed, tests at a wide range of speeds is required. In this work, a range of impact speed from 150 to 350 m/s is employed.
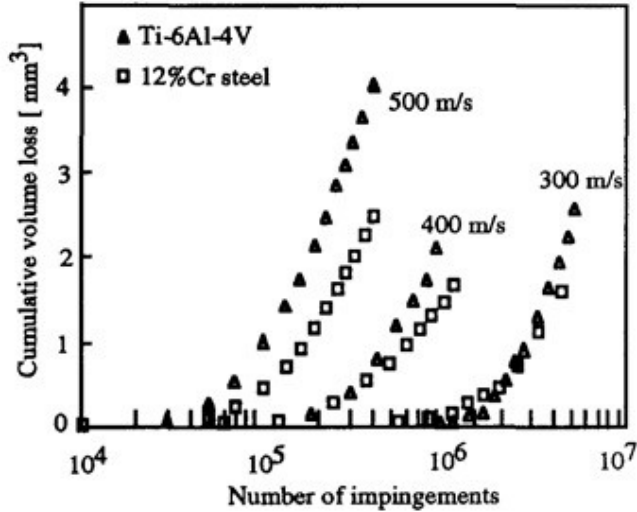
Figure 2-6: Cumulative volume loss *versus* number of droplet impingements for untreated Ti-6Al-4V and 12% Cr stainless steel at various speeds [31].

2.2.3. Sample geometry

The sample geometry is another factor that can influence WDE behaviour, however the studies presented in [9,17,31] considered only one sample geometry, rectangular flat samples. The effect of sample geometry on the WDE behaviour was not considered. Thus, more studies are still needed in order to address the effect of sample geometry on the erosion behaviour. Sample geometries similar to the leading edge of compressor blades could be used. This work tackled this issue by employing two different sample geometries (T-shaped flat and airfoil) during erosion tests. The airfoil geometry is similar to the leading edge of compressor blades.

Despite the efforts to understand the erosion behaviour of Ti-6Al-4V investigations are still needed in order to fully understand its WDE behaviour. These investigations include methods of accurately representing test data, understanding the influence of sample geometry, testing at wide range of impact speed and employing potential surface treatments to combat WDE damage. The following section discusses some surface treatments employed in the literature to mitigate WDE damage.

12

2.3. Surface treatments for WDE mitigation

The two most effective means of mitigating erosion damage are to minimize the main factors causing the erosion damage or to enhance the surface and mechanical properties of blades' materials [32]. Enhancement of surface and mechanical properties of blades' materials has received considerable attention due to cost effectiveness. Despite the efforts to combat or mitigate the erosion damage, it has not been possible to predict or identify and/or quantify a single parameter for WDE resistance [29]. Significant attempts have been made to attribute the surface hardness [10], toughness [10], work hardening [31] and ultimate resilience [25] to the WDE resistance. However, a synergistic effect of these parameters is expected to be a more appropriate term to explain the WDE behaviour. Different surface treatments such as coatings [24,33] and laser surface treatments [25,31] have been employed to mitigate WDE. However, attaining this objective still remains a puzzle due to the presence of surface defects, interface defects and microcracks after surface modification. To fully understand the influence of surface treatments on WDE behaviour of materials, other surface treatments such as mechanical treatments need to be explored. This work explores the influence of two mechanical surface treatments, ultrasonic nanocrystalline surface modification (UNSM) and laser shock peening (LSP), on WDE behaviour for the first time. The next section discusses the potentials of mechanical surface treatments in understanding WDE damage.

2.3.1. Mechanical surface treatments

In mechanical surface treatments, deep levels of compressive residual stresses are induced while improving the surface and sub-surface properties. These treatments are usually employed to enhance the fatigue life of components due to the deep levels of induced compressive residual stresses [34]. Also, WDE damage is likened to fatigue-like damage due to fatigue striation marks caused by the cyclic nature of the liquid droplet impacts [11,18,35].

One would expect mechanical surface treatments to combat WDE damage. However, this is not the case for mechanical surface treatments such as shot peening and deep rolling or low plasticity burnishing [11]. For instance, Ma *et al.* [11] studied the water impingement erosion performance of deep rolled Ti-6Al-4V. Different rolling parameters were used and the samples with the deepest compressive residual stress levels were WDE tested. Different droplet sizes (464 μm and 603 μm) and impact speeds (250 m/s and 350 m/s) were employed. Their [11] WDE results showed that no enhanced WDE performance was observed for the DR treated condition at all tested conditions. They [11] attributed this behaviour to two competing mechanisms at the initiation stage which balance out one another. This is in accord with the explanation given by Frederick and Heymann [10]. They [10] mentioned that mechanical processes might not be very effective in enhancing the WDE behaviour of materials especially during the initiation stage. This is because the mechanical processes plastically deform the surface and induce strain hardening. Repeated droplet impacts strain harden the material further, causing early crack initiation and erosion [10]. Interestingly, Heymann [18] stated that certain degree of work hardening prior to exposure to erosion might be beneficial. However, excessive work hardening might show detrimental effects. To shed more light on this and help resolve this contradiction, UNSM and LSP mechanical surface treatments were selected because they induce large and deep compressive residual stresses but significantly different levels of strain hardening. While, UNSM increases the surface and in-depth hardness [36–39], LSP barely cause any significant change in hardness [40,41]. Hence, it is worthwhile to explore the UNSM and LSP techniques in relation to WDE damage. The following sections briefly discuss the UNSM and LSP techniques and the pertinent literature investigations so far.

2.3.1.1. Ultrasonic nanocrystalline surface modification (UNSM)

UNSM technique is relatively a new surface modification technique that uses ultrasonic vibration energy which converts harmonic oscillations of an excited body into resonant impulses of high frequency [42]. The generated energy from these oscillations are used to impact the work piece at high frequency of up to 20 kHz [42]. Ball tip made of tungsten carbide (WC) [36,43] or silicon nitride ceramic (Si_3N_4) [42,44] attached to an ultrasonic horn is used to strike/impact the work piece surface. Typical impacts on the work piece surface ranges from 20,000 to 40,000 shots per square millimeter [42]. Figure 2-7 shows a schematic illustration of the UNSM process. The high frequency striking leads to severe plastic deformation of the surface, thereby introducing high dislocations density [36]. Thus, nanocrystalline surface layer is formed beneath the specimen surface as shown in Figure 2-7. Other process parameters include; static load, number of impacts/strikes, intervals, amplitude and diameter of the ball tip. Hence, the top surface and in-depth of the work piece are modified which in turn, improves the mechanical properties. The strengthening effect is due to the plastic strain and refined microstructure [37]. The microstructural refinement after UNSM treatment improves mechanical properties according to the Hall-Petch relationship [45]. The UNSM treatment has also been applied successfully on a wide range of materials such as AISI 304 Stainless steel [37–39], S45C steel [45], Ti-6Al-4V [36,42], Pt coated Ni alloy [46], Cu based alloy [47] and AZ91D Magnesium alloy [48] and SiC [44]. Increased surface/in-depth hardness [36–39], reduced grain size [46,48], improved surface quality [37] and deep levels of compressive residual stresses [37,39,42,49] have been reported. Based on the aforementioned attributes, UNSM has shown enhanced fatigue life [37–39,49], enhanced cyclic oxidation behaviour of coated Ni-based superalloy (CM247LC) [46], enhanced tribological properties such as wear resistance [42,44,47,48] and lowering of friction coefficients [42,44,47,48] of materials.
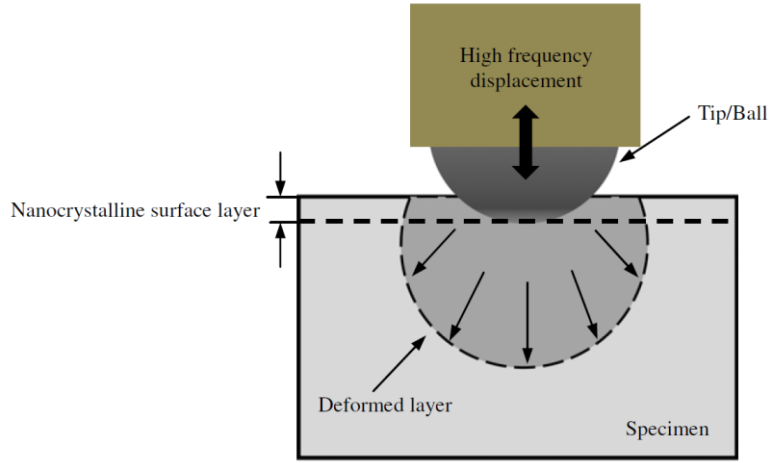
Figure 2-7: Schematic illustration of the UNSM process [48].

However, to date, no study could be found in the literature regarding the effectiveness of UNSM and its associated attributes on the WDE performance/behaviour of Ti-6Al-4V or other alloys. In the current work, the observed microhardness, surface quality and induced compressive residual stresses after UNSM processing are used to understand the WDE performance of treated Ti-6Al-4V.

2.3.1.2. Laser shock peening (LSP)

LSP which dates back to late 60s and early 70s [40,50–56] has been described as a mechanical process where pulses hit the surface with high power intensity generating shock (pressure) waves [54,55,57,58]. These waves plastically deform the surface and compressive stresses are extended into the material [55,58–62]. The basic steps for laser shock wave generation can be described as: firstly, the target surface is covered with an absorbent (sacrificial) coating. This layer vaporizes, forming plasma on the surface with short duration pulse pressure. Absorbent layer prevents melting and laser ablation while maintaining high surface quality [63] and without this layer, the energy conversion from pressure to shock cannot be made effectively [54]. This layer can be aluminum [58,64–66], copper [67], lead [53], vinyl tape [68–70], zinc [66] or black paint [54,59,71]. Hong *et al.* [68] showed experimentally that black paint has the best absorption ability to laser, i.e. almost 100% laser

16

energy is absorbed by black paint as compared to 80% absorption by Al layer. This means that when a target is irradiated, almost 100% of the laser intensity is used to generate the plasma. However, the choice of absorbent layer depends on the target material and other peening parameters. Moreover, LSP is still possible without this layer [72–78]. In this work, the choice of this layer was based on the material and geometrical constraints. For instance, Al layer was used for the thick flat (T-shaped) geometry, whereas no layer was used for the thin membered airfoil geometry. The presence of this layer increases the intensity of the treatment which causes distortion of thin membered sections. For this reason, no layer was used and both sides of the airfoil were treated. Secondly, transparent overlay is applied to prevent the plasma from expanding away from the surface, thereby increasing the intensity of the shock wave. These overlays, also known as the confining medium, can be water [58,59,69,71,79], quartz [40,53,68,80] or glass [68,81,82]. Water is mostly used not to cool the surface but as confining medium as investigated by Kruusing [79]. Water can also be suitable for peening complex geometries [34] and in this work, water is used due to the special geometry employed. Other confining media are K9 glass [83], Pb glass [68], Perspex [68] or silicon rubber which has been studied by Hong *et al.* [68]. Finally, plastic deformation occurs when the shock wave pressure exceeds the dynamic yield strength of the metal [54,56,58,84,85]. This process is schematically shown in Figure 2-8.
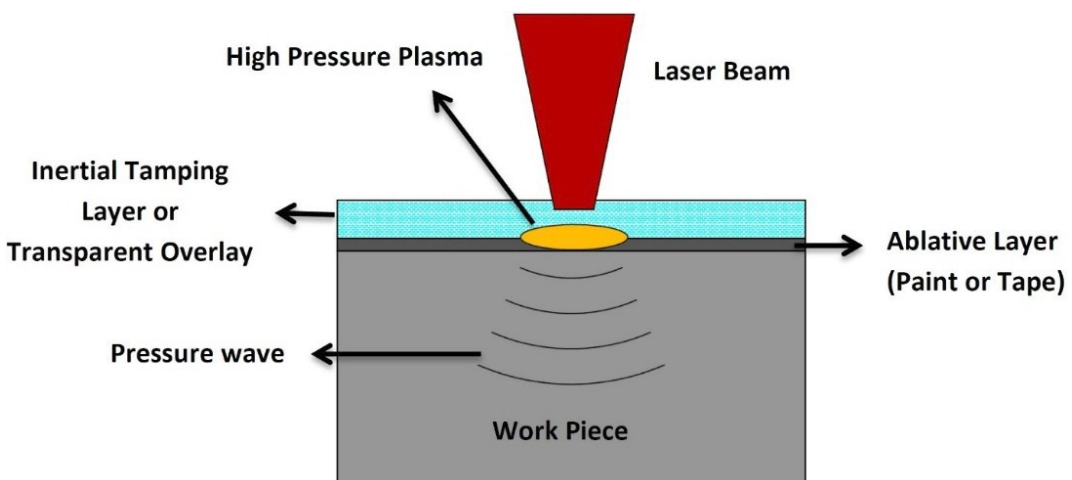
Figure 2-8: Schematic illustration of the LSP process [34].

The plastic deformation results in dislocation multiplication and movements which could possibly affect the microstructure as well as the properties of the material [54]. This is due to the low level of cold working from the laser peening process [34,86]. Reports have shown that the level of cold working in LSP is around 5 % compared to 30-50 % in the conventional shot peening [86–88]. Moreover, it has been reported that multiple laser shocks can increase the percentage of cold work from 5 to 7 % [88]. Hence, changes in microstructure and materials' properties might not be significant due to the small amount of cold work induced during LSP process.

The description of how shock waves are generated is simple compared to the complexity of the process parameters and optimization. Effective shock peening process depends on the material (target), laser and beam parameters as well as the absorbent and transparent overlays [89]. Typical requirements are: Q-switched laser system based on neodymium doped:Glass (Nd:Glass), yttrium aluminum garnet (Nd:YAG) lasers. Different laser wavelengths of 1064 nm (infra-red), 532 nm (green), and 355 nm (ultraviolet) are common. Additionally, time duration for shock wave pressure (laser pulse length) ranges from 10-100 ns [54,79] with energy of 1-100+ J per shot, and spot size of 1-6 mm. A frequency of less than 1 kHz and power density (I) of $0.1\text{-}10^6$ GW/cm^2 [54] are also used. In the current work, Nd:Glass, 18 ns and 10 GW/cm^2 are used. To perform and control the peening process, different equations have been used in the literature. Appendix A summarizes the different equations applied during LSP processing. The parameter selection can be achieved by experimental work and simulations. LSP technique is considered to be a potential substitute to the conventional shot peening (SP) process because of higher depth of residual stresses into the material reaching about 4-5 times deep and high intensity with uniformity across the surface. Furthermore, the LSP provides good surface finish as compared to SP where the roughness needs to be reduced by surface grinding or polishing for typical processes and applications that encounter wear

[54,71,84,90]. Areas such as notches and fillets not accessible during SP can be treated by LSP [91,92]. The applications of the LSP include improvement of fatigue life [54,60,61,71,78,93,94], stress corrosion cracking resistance [95–97], corrosion resistance [56,73,74,98,99], wear resistance [100]. Another application is the surface enhancement of thin membered sections as reported by [91,101] and Mannava *et al.* [102,103] in their patent reports. Even though significant works have been achieved by applying LSP, no study addressed the issue of the influence of LSP process on the WDE performance of Ti-6Al-4V or other alloys. Since LSP process is known to enhance fatigue life of blades' materials and researchers [9,11] ascribed WDE damage to fatigue-like mechanism, studying WDE of LSP treated Ti-6Al-4V is worthwhile.

2.3.1.3. Comparisons between UNSM and LSP treatments

UNSM and LSP surface treatments are different techniques with unique features. However, both process share similar trends in terms of the realized attributes after processing. For instance, deep levels of compressive residual stresses have been reported for both and both processes enhance fatigue life of components which is the primary objective of mechanical treatments. Most importantly, both processes have been employed successfully on Ti-6Al-4V to enhance its fatigue life. To date, no studies were found in the literature regarding the effectiveness of UNSM and LSP on the WDE performance of materials such as Ti-6Al-4V or other alloys. Due to the cyclic nature of the continuous liquid droplet impacts, researchers [9,11] linked WDE to fatigue. If fatigue is the dominating mechanism in WDE, one would expect UNSM and LSP processes to mitigate WDE damage. Besides, studying WDE behaviour of such process that result in different surface attributes in terms of microhardness and microstructure from these processes may enhance the understanding of WDE problem. This forms an integral part of the objectives of this work and the next section highlights the objectives.

2.4. Objectives

The main objective of this work is to investigate the influences of mechanical surface treatments on the WDE performance of Ti-6Al-4V. LSP and UNSM techniques are explored and surface/in-depth characterizations are carried out using X-Ray diffraction (XRD) for residual stress measurement, surface roughness, scanning electron microscopy (SEM) and microhardness. A state-of-the-art rotating disc water erosion rig is used for the WDE testing. Relationships between the WDE performances and the surface/in-depth characteristics are discussed. The specific objectives include:

(1) Study the WDE behaviour of bare (As-M) Ti-6Al-4V and mechanisms of material damage at the early and advanced stages. The influence of impact speed 150 to 350 m/s on the WDE behaviour is elaborated. Determination of the actual number of droplets impacting the surface is detailed.

(2) Investigate the effect of UNSM on the WDE performance of Ti-6Al-4V. Microstructure, compressive residual stress and microhardness are used to understand the WDE performance of UNSM treated Ti-6Al-4V.

(3) Study the effect of LSP process on the WDE performance of Ti-6Al-4V. Effect of LSP and its associated attributes on WDE performance is elucidated.

(4) Establish a relationship between the influence of sample geometries and the effectiveness of these mechanical surface treatments on the WDE performance of Ti-6Al-4V. Two sample geometries, T-shaped flat and airfoil, are used.

Chapter 3 : Water Droplet Erosion Behaviour of Ti-6Al-4V and Mechanisms of Material Damage at the Early and Advanced Stages

A. K. Gujba[a], L. Hackel[b], D. Kevorkov[a], M. Medraj[a,c,*]

[a]Department of Mechanical and Industrial Engineering, Concordia University, 1455 De Maisonneuve Blvd. W. Montreal, Quebec, Canada, H3G 1M8.
[b]Metal Improvement Company-Curtiss Wright Corporation, 7655 Longard Rd, Livermore, California, United States CA 94551.
[c]Department of Mechanical and Materials Engineering, Masdar Institute, Masdar City, P.O. Box 54224, Abu Dhabi, United Arab Emirates.
*Author to whom correspondence should be addressed; E-Mail: mmedraj@encs.concordia.ca; Tel.: +1-514-848-2424 (ext. 3146); Fax: +1-514-848-3175.

ABSTRACT

In this study, the water droplet erosion (WDE) behaviour of Ti-6Al-4V and mechanisms of material damage were investigated. The WDE test was conducted in an advanced rig in accordance with ASTM G73 standard. The influence of impact speed between 150 and 350m/s on the WDE behaviour was explored and the cumulative mass losses *versus* the exposure time/number of impingements were plotted. It was observed that the higher the impact speed the faster the erosion initiation time and greater the maximum erosion rate (ER_{max}). ER_{max} was also found to be related to the impact speed with an exponent of 9.9 in a log-log scale. SEM images showed that the early stages of erosion damage were mainly limited to the formation of microcracks, asperities and isolated pits of irregular shapes. It was found that the most profound mode of material removal during the advanced stage of water droplet erosion was hydraulic penetration. Sub-surface, side wall cracking and material folding/upheaving were also features observed.

Keywords: Water droplet erosion; impact speed; incubation stage; advanced stage; Ti-6Al-4V

3.1. Introduction

In the electric power generation industry the gas turbine efficiency is an important issue and is directly affected by the ambient temperature. Meher-Homji and Mee [1] reported that a rise of $1^{\circ}F$ results in a turbine efficiency decrease of 0.3-0.5%. This adverse temperature effect is obviously a season dependent phenomenon. For instance, in the United States, a 9% loss of gas turbine output power was recorded in summer versus winter periods [2]. The lower turbine efficiency is attributed to a decrease in air density leading to a decrease in the intake air mass [3]. The lower efficiency results in high electricity cost [4] and high CO_2 emissions [3]. To keep the ambient temperature as low as possible, the inlet air fog cooling technique is used [1]. In this technique, water droplets are sprayed into the inlet of the gas turbine compressor to cool down the intake air thereby increasing the intake mass. The water droplets reduce the temperature leading to an increase in the output power [5]. However, an overspray can occur when all droplets are not being evaporated [5,6]. Despite the cost effectiveness of this fogging method, droplets cause a severe erosion damage problem for the leading edge of the compressor blades and consequently a significant fatigue cracking issue for the full blades, especially at high speeds. Khan [6] stated that the erosion damage phenomenon was featured as the synergy of the impacting water droplets and rotating blade. This is usually termed as the "water erosion by impingement or water droplet erosion (WDE)".

Water erosion by impingement is a special form of erosion produced by repetitive impingement of high velocity liquid droplets on a solid surface [104]. The mechanism of the erosion process is complex by virtue of the many parameters involved, including: impact velocity, impact angle, droplet size, droplet density, frequency of impacts, liquid film formation and mechanical properties and conditions of the target material. However, this erosion phenomenon has also been found in several industrial applications including cooling

pipes of nuclear plants [105], sewage plants and sea water systems [106], aerodynamic surfaces of aircrafts and missiles [29] flying through rainstorm at subsonic and supersonic speeds [10]. The WDE damage is predominantly caused by two main factors; (1) the high pressure exerted by the water droplet on the exposed area of the solid surface and (2) the radial liquid flow along the surface at high speed, which occurs after the initial droplet pressure lessens [10]. Moreover, this erosion damage reduces the efficiency of mechanical components due to aerodynamic losses [107]. Despite the efforts to combat or mitigate the erosion damage, it has not been possible to identify or quantify an absolute parameter for WDE resistance [29]. This is due to the fact that erosion rate is not constant with time and therefore, no single value can quantify the erosion test. Significant attempts have been made to attribute the hardness [10], toughness [10], work hardening [31], and ultimate resilience [25] to the WDE resistance. More so, a synergistic effect of these parameters would be a more appropriate term. For this reason, material (rating) ranking system which is somewhat semi-quantitative has been developed by Heymann [108]. He [108] proposed sets of comparative studies in order to evaluate erosion resistance under different sets of conditions. In this system, the normalized erosion resistance, which is the maximum rate of volume loss of a reference material divided by the maximum rate of volume loss of material being evaluated. However, the major setback here is the lack of precision in projecting the erosion damage. ASTM standard [29] mentioned that for bulk materials, the incubation period and the maximum erosion rate determined from empirical relationships could be used for the material rating. This is provided that the principal liquid impingement parameters such as droplet size, impact velocity are known. Also, due to the variation of erosion rate with exposure time and synergy of different interacting WDE parameters such as impact speed and droplet size, different WDE behaviours and damage mechanisms will prevail. Thus, predicting or projecting the erosion damage becomes difficult. In this case, the experimental

23

investigations become paramount. The mechanism by which material is removed or chipped out is an important aspect of the WDE damage. However, the challenge lies in defining the hydrodynamic conditions that cause particular erosion and material detachment effects [10]. Nevertheless, it is paramount to fully understand the WDE behaviour of materials and the mechanism by which material is removed when exposed to an erosive medium. To understand this, the concept of water hammer pressure, stress wave propagation, liquid outflow and hydraulic penetration as well as material response must be comprehended.

In this study, the WDE behaviour of Ti-6Al-4V and the mechanism of material removal during the early and advanced stages of erosion damage were investigated. Special attention was given to the influence of impact speed of the erosion behaviour. Cumulative mass loss, number of impingements, erosion initiation time and maximum erosion rate (ER_{max}) with respect to the impact speed were derived. Study on the mechanism of material removal was conducted with the aid of a scanning electron microscope (SEM). Here, the as-eroded surface and polished cross sectional views were investigated.

3.2. Experimental procedure

3.2.1. Material and geometry

For the present study, Ti-6Al-4V (ASTM B265, Grade 5) alloy, used for compressor blades in gas turbine, was investigated. Typical room temperature physical and mechanical properties are: elastic modulus (113GPa), Poisson's ratio (0.342), melting point temperature range (1604-1660°C) and tensile strength (880MPa). T-shaped coupons, as shown in Figure 3-1, were machined using a CNC Haas machine under flood coolant in accordance to the WDE testing rig geometry. Figure 3-2 shows the starting microstructure of the Ti-6Al-4V alloy which contains α and β phases.
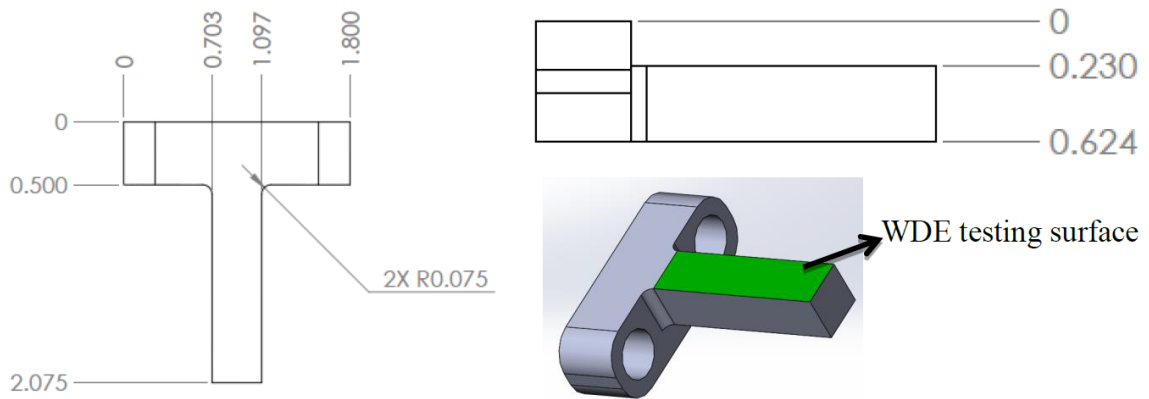
Figure 3-1 : Typical T-shaped Ti-6Al-4V sample (dimensions are in inches).
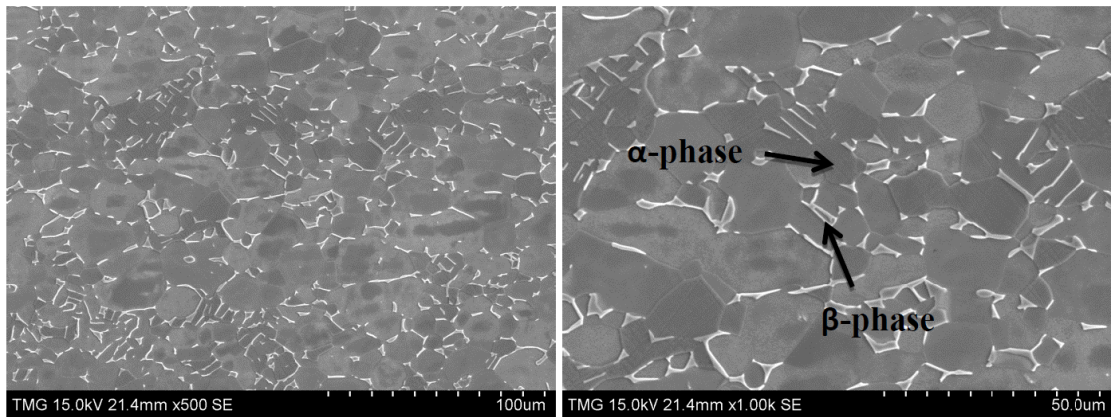
Figure 3-2: SEM micrographs showing the initial Ti-6Al-4V microstructure.

3.2.2. WDE testing, mass loss measurement and characterization of eroded coupons

A state-of-the-art rotating disc rig at Concordia University, shown in Figure 3-3, was used for studying the WDE behaviour of the Ti-6Al-4V alloy. The test was carried out in accordance with ASTM G73 standard [29]. This is a unique testing rig that reaches up to 500 m/s linear speed (equivalent to 20,000 rpm rotational speed). It has a working chamber coupled with a vacuum system, a compressed air driven turbine and a water droplet generating system. The rig has a user friendly control system allowing monitoring of the vibration level, vacuum level, chamber temperature, turbine bearing temperature as well as the rotational speed. Coupons are fixed at the opposite ends of the rotating disc as depicted in Figure 3-3.
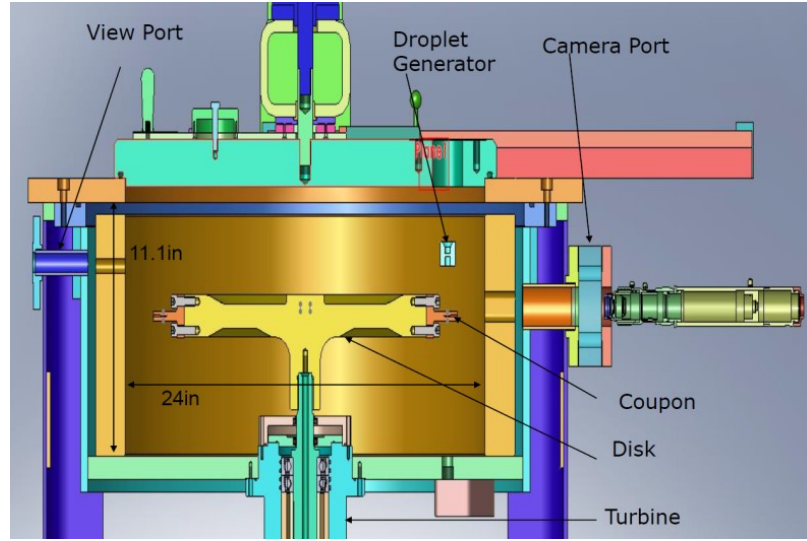
Figure 3-3: Schematic illustration of the water erosion rig used in the present work.

To avoid friction between the rotating disc and air, that cause significant temperature rise, a 30-50 mbar vacuum is maintained during the experiment. Thus, favourable working temperature was maintained and water evaporation avoided. This vacuuming approach further allows for WDE testing at very high impact speeds. It is worth mentioning that a separate setup using a transparent chamber was used to simulate the water droplets behaviour inside the rig. The droplet size distribution was monitored using a high speed camera (9000 frames per second) with the aid of this setup. Furthermore, the number of droplets was counted which was essential for computing other parameters such as the volume of impinging water. Similar water droplet generation and size distribution determination has been reported [11,17,28]. Typical WDE testing parameters are summarized in Table 3-1. Once a desired rotational speed was attained, the water droplets (de-ionized water) were introduced while controlling the flow rate. The setup enabled the droplets to impact the coupons at 90° in a repetitive fashion. The impact angle of 90º causes the most severe water erosion damage. The erosion exposure time depended on the impact speed used. However, timings at 30 second intervals were used in order to capture the first stage of the erosion process (incubation period). Also, longer times (1, 2, 3 up to 840 minutes) were employed as the test progressed to the advanced stage of the erosion process.

26

Table 3-1: WDE test parameters used in this work

Process parameter	Variable
Impact speed (m/s)	150, 200, 250, 275, 300, 325, 350
Rotational speed x 10^3 (rpm)	6, 8, 10, 11, 12, 13, 14
Flow rate (liter/min)	0.05
Nozzle distance from coupon (mm)	5
Average droplet size (μm)	463
Initial pressure (mBar)	30-50
Impact angle (°)	90

Coupons were weighed using a balance and pictures were taken with a standard stereo optical microscope, at each interval. Typical erosion curves such as cumulative mass loss *versus* exposure time/number of impingement and ER_{max} *versus* impact speed were plotted. For accurate determination of incubation period and maximum erosion rate, a three line representation method was used as demonstrated in Figure 3-4 [12]. The mechanism of material removal during the incubation and advanced stages was monitored and the damages were characterized using SEM. Here, the as-eroded surface and polished cross sectional views were investigated. Microcracks, stress wave propagation, crack initiation sites, formation of pits and removal of cavity were primarily investigated. Results and discussion are presented in the next section.
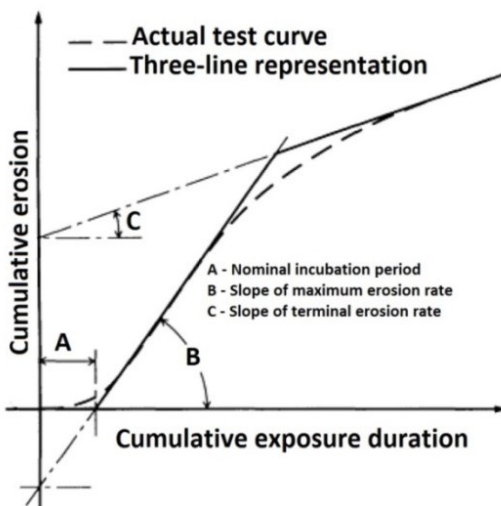
Figure 3-4: Typical three line representation for WDE curve characterization [12].

3.3. Results and discussion

3.3.1. Droplets generation and size distribution

Prior to the WDE tests, several experiments were performed with an impact angle of 90° in order to establish and calibrate the erosion test conditions, such as initial pressure, flow rate and droplet size distribution. Droplet generating system and a nozzle were used to produce a streak of water droplets. The generated droplets and sizes depend on the water line pressure, nozzle diameter and flow rate [17]. In this study, water line pressure of 1psi, flow rate of 0.05 liter/min and nozzle diameter of 400 μm were used. The diameters of the droplets were measured and a statistical distribution of 200 droplet diameter counts was derived as shown in Figure 3-5a. Figure 3-5a indicates that the droplet size range was between 400-527 μm with an average size of 463 μm. In addition, the observed droplet size range is within the spectrum of size ranges (50-1500 μm) encountered by components subjected to WDE [32,109] and used in similar investigations [11,17,28,31]. During the off-situ droplet size monitoring and with the aid of a high speed camera, the equivalent number of droplets hitting the coupon surface per revolution was obtained. The number of droplets hitting the surface depends on the dimension of the exposed surface. For instance, Figure 3-5b shows that 6 droplets would be hitting the exposed surface of an 8 mm thick coupon per revolution.
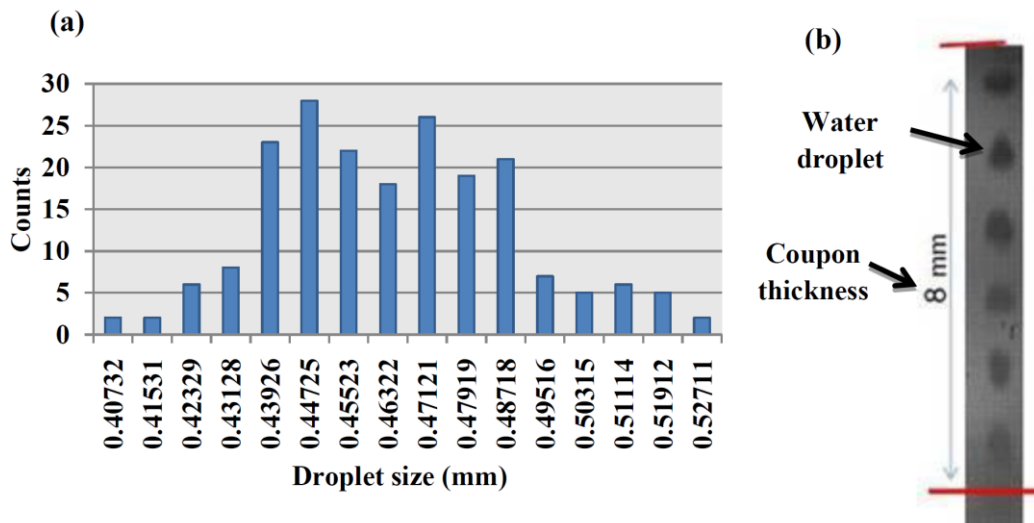
Figure 3-5: (a) Statistical distribution of droplet size range and (b) equivalent number of droplets hitting the coupon.

This observation and finding indicate that the total number of droplets or volume of water impinging the coupon during testing can be quantified with reasonable degree of accuracy.

3.3.2. WDE curves and characterization

Water erosion results are typically reported as cumulative material loss *versus* cumulative exposure time [29]. However, "number of impingements" was preferred to cumulative exposure time in this paper. This is because the number of droplets impinging the coupon at a particular time was known (Figure 3-5b). Moreover, the exposure time does not quantify the amount of water used, thus, number of impingements could be employed successfully in representing the experimental results and data. Per contra, this was not the case in earlier WDE studies such as in [9,25,33]. Moreover, the number of impingements was obtained using Equation 3-1.

$$N_{imp} = R \times E_t \times N_{droplets} \qquad\qquad (3-1)$$

Where N_{imp} is the number of impingement, R is the rotational speed (rpm), E_t is the erosion exposure time (minutes) and $N_{droplets}$ is the number of droplets hitting the coupon per revolution which is 6 as per Figure 3-5b. Contrarily, Kamkar [9] defined the number of impingement as "the number of times the sample intersects the water stream". This definition would render the x-axis cumulative exposure duration inaccurate or underestimated, since only $R \times E_t$ were considered while neglecting $N_{droplets}$. It is worth noting that the number of droplets impacting the sample varies with droplet size thus, rendering [9]'s estimation more inaccurate. Therefore, it will be difficult to quantify the volume of water injected at a particular time from [9] and the number of impingements to erosion initiation will be underestimated.

The cumulative mass loss can be described as the sum of material loss due to exposure to an erosive medium such as water at a particular time. For better quantification of the mass loss measurement, tested coupons were weighed after each interval. For instance, 30 seconds

intervals up to 2 minutes were taken initially in order to capture the incubation period (period of negligible mass loss) [12]. It is worth mentioning that the measurable mass losses are mostly observed when the first threshold velocity (endurance limit) is exceeded after a certain number of impacts [30]. Therefore, the first threshold velocity is the velocity below which no damages (significant mass losses i.e. > 0.2 mg) are observed. The cumulative mass loss *versus* the exposure time/number of impingements graphs for the varied speed tests are reported in this work. The WDE curves for impact speeds of 150, 200, 250, 275 and 300, 325, 350 m/s are shown in Figures 3-6a and 3-6b, respectively. Figures 3-6a and 3-6b show that reducing the impact speed delayed the erosion initiation time and reduced the erosion rate. At an impact speed of 150 m/s no erosion was observed after long exposure to the erosive medium. Only an erosion trace line was observed under the optical microscope as shown in the inset macrograph in Figure 3-6a. This indicates that the first threshold velocity (impact speed) of the material is greater than or equal to 150 m/s. On the other hand, increasing the speed showed faster erosion initiation and greater erosion rates. More on the effect of speed on the erosion initiation and maximum erosion rate has been discussed in sections 3.3.2.1 and 3.3.2.2, respectively. It is well known that the shape of erosion curves depends on the target material and the erosion condition [29]. For instance, material with a well-behaved erosion curve has an S-shaped erosion curve with distinct erosion stages [29]. These stages are: incubation period with negligible mass loss; acceleration stage (energy accumulation zone [110]) to a maximum rate stage; deceleration (attenuation) stage with declining erosion rate and terminal or final steady state with constant erosion rate [12,30]. These characteristic curves are further affected by surface roughness [17,30], surface properties, microstructure [10], geometry [30], combination of impact speed and droplet size [30]. For instance, Kirols *et al.* [17] reported that merely polishing the surface prior to WDE tests delayed the erosion initiation and in some cases, the maximum erosion rates in 12 % Cr-Steel and Ti-6Al-4V.
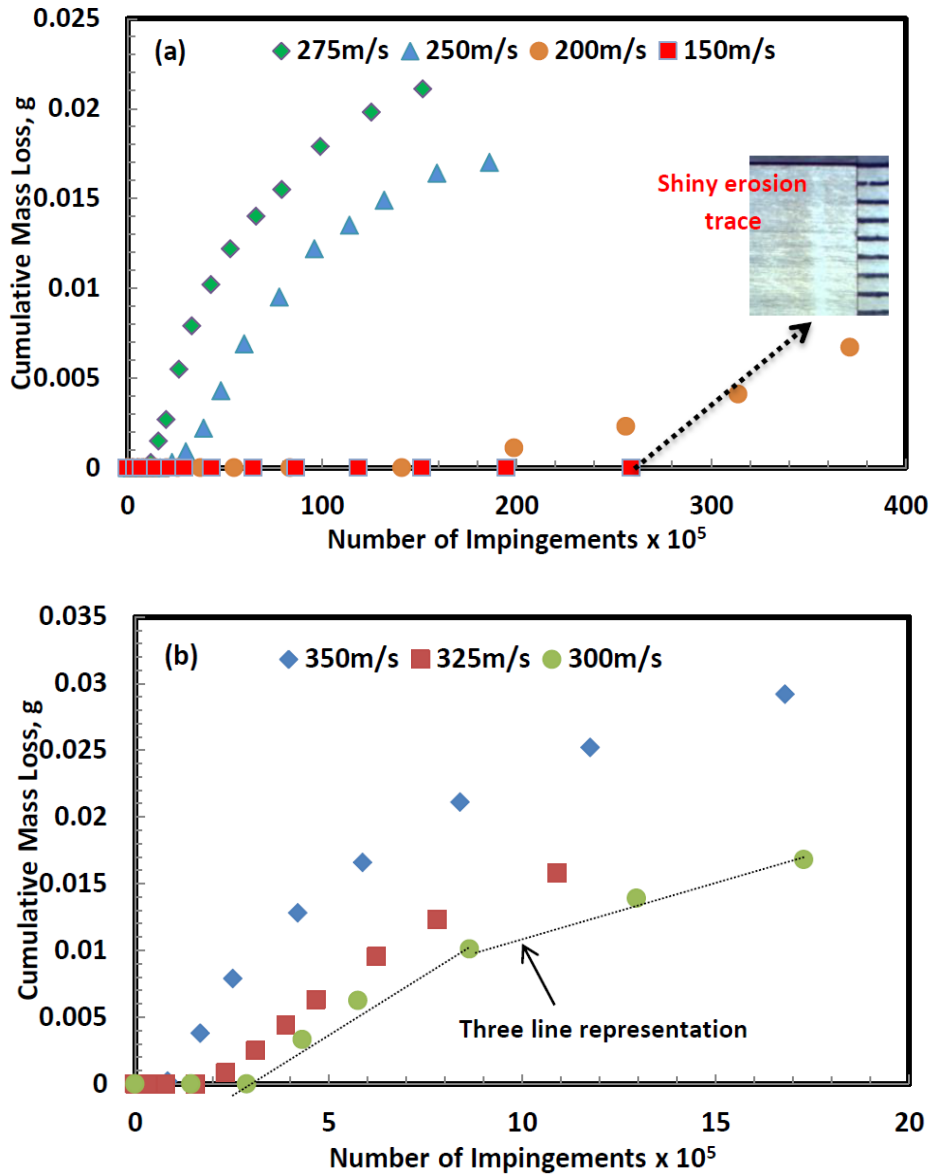
Figure 3-6: WDE curves for (a) 150 to 275 m/s and (b) 300 to 350 m/s impact speed tests.

It can be seen from Figure 3-6a that the erosion stages were different after 50×10^5 impingements for impact speeds of 200 and 250 m/s. The stages attained were incubation and maximum erosion for 200 and 250 m/s. This is also consistent with the WDE results of forged Ti-6Al-4V [9]. In this present study, the surface quality/roughness, microstructure and geometry were kept constant. Furthermore, employing the three line representation according to Figure 3-4, the erosion curves were characterized and the initiation time and maximum erosion rate were calculated.

3.3.2.1. Effect of impact speed on the incubation period

The initiation of erosion is an important stage in the erosion process though it is often affected by several factors, such as: surface roughness, impact pressure, velocity and erosion conditions. According to Hoff *et al.* [111], the predominant factor in the WDE material damage is the impact velocity of the specimen. This was attributed to the increased kinetic energy with increase in impact velocity (V^2). In real life applications, however, the impact velocity comes from both the movement of the droplet and the rotation of blades. Kiel *et al.* [112] reported that the kinetic energy transferred into the material results in plastic deformation. However, this stage is still not well understood as to the definition of the stage, which solely depends on the observer. For this work, the incubation period was defined as the period where mass loss is negligible. At the early stages of the erosion damage (end of incubation period), isolated pits are observed which result in measurable mass loss. The early damage mechanism is discussed in section 3.4. Table 3-2 shows the typical incubation period (erosion initiation time) and number of impingements to erosion initiation as well as the maximum erosion rates observed at various speeds. From the three line representation analysis, the general trend is that the higher the speed the shorter the incubation period. This was the case for impact speeds from 200 up to 325 m/s. However, it was observed that the incubation periods for speeds of 325 and 350 m/s were close and in the range of seconds. This can be attributed to the severity of the test and the resulting high induced stresses. The observed trends can also be attributed to the increased water hammer pressure and impact energy with increased impact speed. This observation is in accord with the explanation given by Thiruvengadam and Rudy [110], Ma *et al.* [11], Mahdipoor *et al.* [24] and Kamkar [9]. The water hammer pressure is the induced pressure exerted by the "arrested" liquid droplet on the solid surface. This is an important factor that influences the surface damage especially at the incubation stage [11]. According to Heymann [12,13], this pressure can be

32

considerably higher than the yield strength of many alloys especially at high impact speeds. Equations 3-2 to 3-4 show the different water hammer pressure representations in the literature [12,13].

$$P = \rho CV \qquad (3\text{-}2)$$

$$P = \rho CV \left(1 + \frac{KV}{C}\right) \qquad (3\text{-}3)$$

$$P = \rho CV \left(2 + \frac{(2K-1)V}{C}\right) \qquad (3\text{-}4)$$

Where P is the pressure, ρ is the density of the liquid (1000 kg/m^3), C is the acoustic velocity of the liquid (1500 m/s – for water), V is the impact velocity (m/s) and $K = 2$ for water.

These equations are approximations that satisfy wide range of impact speeds on solid surfaces. Equation 3-2 represents one dimensional water hammer pressure developed for liquid-solid impact on a rigid surface. Equation 3-3 incorporates the shock wave velocity variable for rigid and elastic surface. Moreover, Equation 3-4 provides a reasonably critical impact pressure with the condition that Mach number is greater than 0.2 as reported by Heymann [13]. Therefore, impact speeds equal to or greater than 300 m/s will satisfy the assumption of [13]. Table 3-2 shows the calculated impact pressure values based on Equation 3-4 for different impact speeds. One can see that the impact pressure is proportional to the impact speed and at higher speeds the pressure induces stress that exceeds the yield strength of the material. Sanada *et al.* [113] also reported that different pressure distributions is produced at different Mach number (*Mi*) ranges. They [113] concluded that the difference in pressure at the center and edge of the droplet is minimized for low *Mi* (between 0.1 and 0.4). For high *Mi* (>0.4), the edge pressure is 3 times that of the center when jetting starts [16,114]. Therefore, the initiation period will be influenced greatly by the exerted impact pressure as shown in Figure 3-7. Figure 3-7 also shows that the impact pressure is inversely proportional to the number of impingements to erosion initiation. Zhou *et al.* [115] showed a linear

relationship between water hammer pressure and droplet size. However, in this present work the average droplet size was kept constant.

Table 3-2: Data from three line characterization of erosion curves for various speeds

Impact speed (m/s)	Rotational speed (rpm)	Water hammer pressure (MPa)**	Erosion initiation time (minutes)	Number of impingement to initiation x 10^5	ER_{max} x 10^{-5} (g/minute)
150	6000	506	840*	302.40*	*
200	8000	705	340	163.20	1.54
250	10000	919	45	27.00	12.00
275	11000	1032	20	13.20	25.00
300	12000	1148	4	2.88	125.00
325	13000	1268	2.5	1.95	172.00
350	14000	1392	1	0.84	333.00

*WDE test was stopped due to prolonged testing without any erosion,**from equation (3-4).
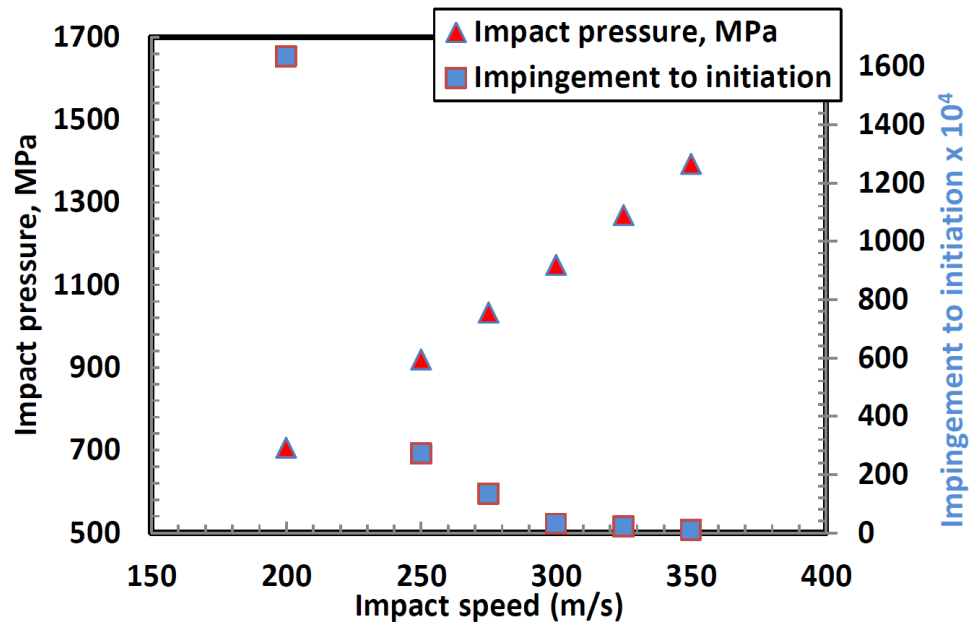
Figure 3-7: Relationship between impact speed, impact pressure and erosion initiation.

Figure 3-6 shows that reducing the impact speed delayed the erosion initiation time and this was attributed to the reduced impact pressure and impact energy at lower speeds. It is important to note that when lower speeds were used, the erosion time intervals were

increased. Therefore, prolonged erosion time corresponding to more water impingements was adapted. For instance, this can be seen for speed test of 200 m/s (Figure 3-6a) where the erosion started after 340 minutes (16.32 million impingements). Even though the reduction of impact speed showed prolonged initiation times, such speeds cannot be used in the mitigation of erosion. These low speeds are not practical in running compressor blades in gas and steam turbines. The present study covered a wide range of impact speeds (150 to 350 m/s) however, very low speeds (<150 m/s) and very high speeds (>350 m/s) were not tested. The extrapolation of initiation times and maximum erosion rates using the current data might give unsatisfactory results. This is due to the fact that liquid characteristics and target responses vary significantly with impact speeds. Since the erosion rate is not constant with time, prediction of erosion damage would also be difficult. In this case, experimental investigation becomes paramount.

Another point of interest is the threshold speed range (150 m/s $\leq V_{threshold}$ <200 m/s) that was observed after prolonged time of exposure (up to 840 minutes for test at 150 m/s). This velocity is the so-called first threshold while the velocity at which mass loss is measurable is the second threshold [30]. However, there is a challenge in understanding this velocity due to the target response, erosion facility, surface quality and the water droplet characteristics such as size, density, impact angle and the frequency of impact. The forgoing point has been mentioned by Rein [116]. Table 3-3 shows the experimental $V_{threshold}$ values for different materials and applications.

One might suggest that for every reported threshold speed, the test conditions should be clearly stated. This is because the first threshold velocity by one researcher might correspond to the second velocity by another researcher. For instance, Thiruvengadam and Rudy [110] defined their threshold velocity as the velocity at which detectable indentations are observed using a 10x magnifier under suitable lighting. They [110] reported the relationship between

the impact (threshold) velocity and the number of impacts after which detectable indentations are observed on Al 1100 and 316SS alloys. After several repeated observations, they [110] showed that the threshold velocities corresponding to 10 million impacts were 15 m/s for Al 1100 and 45 m/s for 316SS (Table 3-3). In this work, it was found that using average droplet size of 464 μm and flow rate of 0.05 litre/min, the threshold velocity was in the range of 150 m/s $\leq$ V$_{threshold}$ <200 m/s after 840 minutes of exposure time which corresponds to approximately 30 million impingements. Here, only a shiny erosion line trace was observed under the optical macrograph as shown in the inset of Figure 3-6a.

Table 3-3: Experimental threshold velocities and n[th] power of velocity by different authors

S/No	Material	First threshold speed (m/s)	n[th] power of velocity	Ref.
1	S15C-Carbon steel[1]	80	6	[117]
2	STPA22- Alloy steel[1]	90	7	[117]
3	SUS304-Stainless steel[1]	120	7	[117]
4	Al1070, Al5056, C3604, SS400, S20C[1]	-	7*	[118]
5	Al-1100[2]	15	5	[110]
6	316SS[2]	45	5	[110]
7	TiAl[3]	200-250	11-13	[28]
8	Ti-6Al-4V[3]	-	9	[9]
9	Ti-6Al-4V[3]	-	7-9	[28]
10	Ti-6Al-4V[3]	150 ≤ V< 200	>9	Present study

[1]Liquid impingement erosion for pipe wall thinning, [2]Liquid jet impact, [3]Water droplet erosion for compressor blade applications, *Average value for all materials with a scattering from 5-9 depending on material.

3.3.2.2. Effect of impact speed on the maximum erosion rate

Immediately after the energy accumulation (acceleration) stage the material loss rate becomes significant up to a maximum. This stage is the zone during which the measured mass loss is at its peak due to fracture and deep craters [110] thus, huge chunks of materials are removed. From Table 3-2, the influence of impact speed on the maximum erosion rate showed that greater ER$_{max}$ values were recorded at higher speeds. Oka *et al.* [119] also

reported similar trend of maximum damage (erosion) rate at higher impact speeds. For lower speed tests, more exposure time/impingements were required to have an equal mass loss than when using higher speeds. Moreover, it can be suggested here that each impinging droplet causes its own damage during the very high impact speed. Whereas, water accumulation might have decreased the erosion rates in low impact speed test. However, experimental proofs are needed to verify this hypothesis. More so, the energy level is greatly attenuated at lower impact speed than higher impact speed. The ER_{max} and impact speed relationship has been discussed in the literature [110,117]. That is the power law relationship where speed exponents were determined. This dependency between the ER_{max} and impact velocity is derived using Equation 3-5.

$$E_R \propto V^n \qquad\qquad (3-5)$$

Where E_R is the erosion rate, V is the impact speed and n is the speed exponent. Typical speed exponent values for metal are in the range of 5-7 as reported in the literature [110,111,120]. Table 3-3 shows speed exponent value for various materials in comparison with the present work. Based on Table 3-3 and Figure 3-8, a different exponent value higher than 9 which is in accord with Kamkar [9] and Mahdipoor *et al.* [28]. Thus, this can be attributed to the test conditions, set-up and erosive medium characteristics. Having different material microstructures could reveal different exponent values. The method of ER_{max} determination could also have played a role in this difference [28]. For instance, using the instantaneous erosion rate approach which is the slope between two consecutive points on the WDE curve could give a difference value than that observed when using Figure 3-4. Even though erosion rate is sensitive and proportional to the impact speed (generally erosion conditions) [28], no satisfactory explanation for the dependency between the erosion rate and impact velocity has been provided in the literature yet. This could be due to the fact that other parameters such as droplet size, droplet velocity and the target materials properties are also

playing significant roles in the erosion process. For instance, Mahdipoor *et al.* [28] reported different speed exponent values for Ti-6Al-4V tested with different droplet sizes. Values of 8.9 and 7.7 were observed for droplet size of 463 and 603 μm, respectively. Also, Ikohagi [121] mentioned the influence of liquid film on the erosion rate. He [121] studied the numerical simulation of single droplet (100 μm size) impingement on a solid surface. He [121] found that the exponent value (n) increased from 5.3 to 7.7 for the solid surface with a liquid film of 2.5 μm thickness. Fujisawa *et al.* [122] further showed in their experimental work combined with theoretical consideration that increase in the liquid film thickness increases the damping effect of the impact pressure. Hence, thicker liquid film shows reduced erosion rates and this is in accord with the suggestion by Ikohagi [121]. The works in [28,121,122] clearly indicate that speed exponent is function of droplet size and the entire testing conditions. Therefore, accounting for the effect of all these parameters might be tedious. Thus, different exponent values might be observed.

$$ER_{max} = 2x10^{-23}V^{9.9}$$
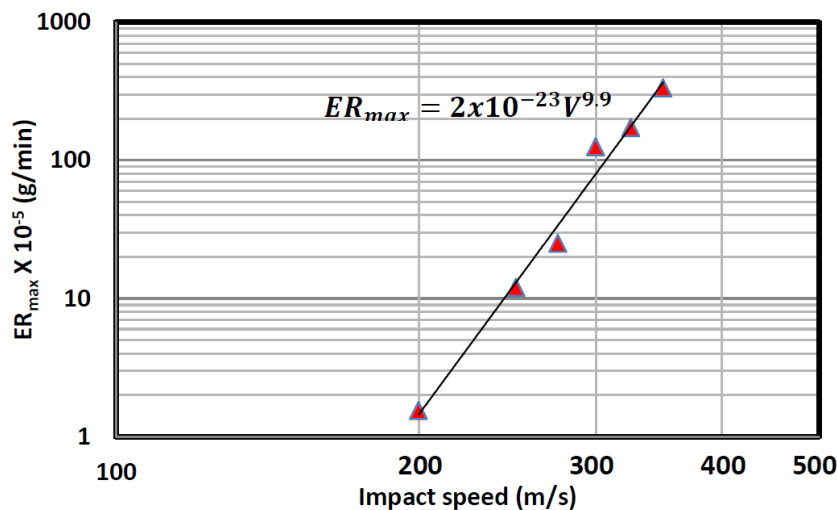
Figure 3-8: Log-log graph of ER$_{max}$ *versus* impact speed.

3.3.3. Optical macrographs of eroded coupons

To demonstrate and understand how the erosion process evolved and progressed, optical macrographs were taken after each interval during testing. This is also the interval during which the coupon is weighed and the mass loss is recorded. Figure 3-9a-c shows the erosion

38

evolution and procession for the tested Ti-6Al-4V coupons at impact speeds of 250, 300 and 350 m/s, respectively. Normally, the erosion process initiates with an erosion trace line due to impingement of droplets [11,17]. Figure 3-9a shows this initiation process after 20 minutes of exposure time at 250 m/s where the mass loss is negligible. This stage is reported as the region of local plastic deformation that causes grain displacement leading to formation of microcracks [112] and depressions [22]. After a few additional impacts, small pits are formed along the erosion trace line and with further impacts, large isolated pits are formed and gradual pit growth is observed. This is the situation seen in Figure 3-9a after 50 minutes of exposure time where mass loss of 0.0007 g was recorded. After 65 minutes, acceleration stage was reached where significant mass loss of 0.0026 g was observed due to the pit coalescence and secondary cracks intersecting thereby, detaching larger pieces of material [9,10]. The maximum erosion rate (0.000213 g/min) was reached after 80 minutes where material damage was at its peak and complete crater has been formed. The material damage was due to high pressure exerted and the liquid lateral jetting. The jetting is the radial outflow of the liquid droplets after impact which is identified as a major cause of the erosion damage [18]. This jetting also interacts with surface discontinuities [16], thereby forming surface cracks and surface asperities. This leads to significant removal of material during the advanced erosion stages. It is important to note that with increased exposure time and a severe erosion test (for instance, increase in impact speed), both depth and width of the craters are increased [11]. For instance, crater width of less than 1 mm and more than 1 mm were observed after 65 and 310 minutes, respectively (Figure 3-9a). This observation is also true when comparing the crater width/depth for different speeds at the same exposure time and this is in accord with the findings of [9]. Similarly, Figures 3-9b and 3-9c show that increasing the impact speed accelerated the erosion evolution and progression as compared to Figure 3-9a. For instance, measureable mass losses were observed after 8 and 2 minutes of

39

exposure only at 300 m/s (Figure 3-9b) and 350 m/s (Figure 3-9b), respectively. Maximum erosion rates were 0.001125 g/min and 0.00245 g/min after 12 and 5 minutes of exposure at 300 m/s and 350 m/s, respectively. Full crater was formed after 3 minutes at 350 m/s compared to the full crater formation after 80 minutes at 250 m/s. Therefore, Figures 3-9a-c show the influence of changing the impact speed on the erosion behaviour. The early erosion initiation and progression at high impact speed is attributed to the increased impact pressure which induced significant stresses.
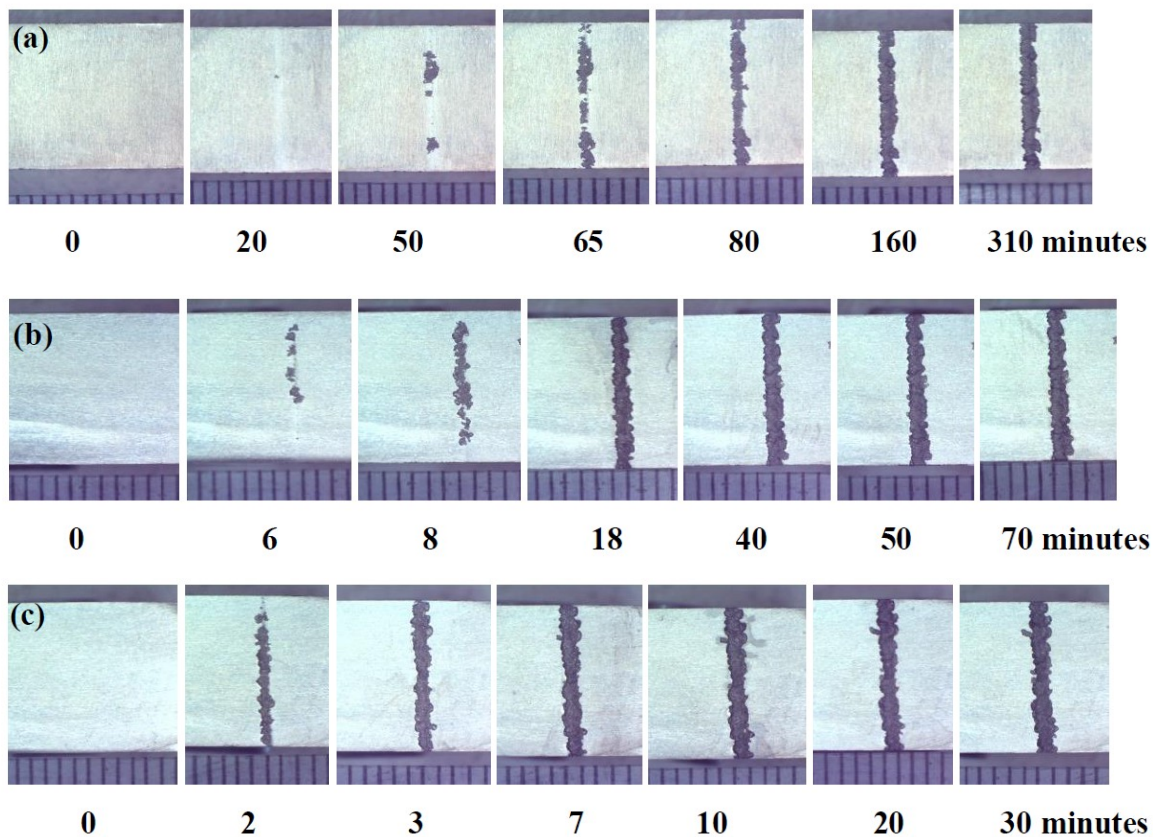
Figure 3-9: Optical macrographs showing the erosion evolution and progression on Ti-6Al-4V coupon tested at (a) 250 m/s (b) 300 m/s and (c) 350 m/s. The scale at the bottom of each image is in mm.

To further understand the influence of impact speed on the erosion crater behaviour; the accumulated material loss, crater width and depth were observed after certain exposure times/number of impingements at different impact speeds. Figure 3-10 shows the polished cross-sectional views of the erosion craters at impact speeds of 250, 300 and 350 m/s halted after 415, 70 and 30 minutes, respectively. Prolonged exposure time was chosen for low

impact speed (250 m/s) in order to have significant mass loss for better comparison. The crater widths and depths were measured with the aid of a microscope. The accumulated material losses, crater widths and depths are presented in Table 3-4. It can be seen from Table 3-4 that increasing only the impact speed showed significant mass loss and increase in crater dimensions even with fewer number of impingements/exposure time. For instance, test at 350 m/s which was halted after 30 minutes (after 25 x 10^5 impingements) showed 48.9 % and 31.2 % increase in mass loss as compared to test at 250 m/s (after 249 x 10^5 impingements) and 300 m/s (after 50 x 10^5 impingements), respectively. Similarly, increasing the impact speed from 250 m/s to 350 m/s showed a 32 % and 100 % increase in crater width and depth, respectively. It is worth noting that the number of impingements for test at 250 m/s is 10 times more than test at 350 m/s. It should also be noted that the crater depth might vary depending on the location of the cross-section. This is the case shown in Figures 3-10b-c where 350 m/s test showed less depth compared to 300 m/s test. Based on several cross-sectional views taken, similar trends were observed especially for the accumulated mass loss and crater depth. For instance, another set of craters were sectioned after 18.6 x 10^5, 50 x 10^5 and 30 x 10^5 impingements at 250, 300 and 350 m/s, respectively. Accumulated mass losses were 0.0170, 0.0264 and 0.0391 g, respectively. Crater depths of 0.392, 0.769 and 0.841 mm were observed, respectively. This observation is in general agreement with the data in Table 3-4 which indicates a linear relationship between the impact speed and observed crater depth. Moreover, the significant mass losses observed at high impact speed (350 m/s) could suggest that the crater dimensions are highly representative. As mentioned previously, this is attributed to the increased test severity, which induces high stresses. This can also be attributed to the change in droplet properties with increase in test severity [17].
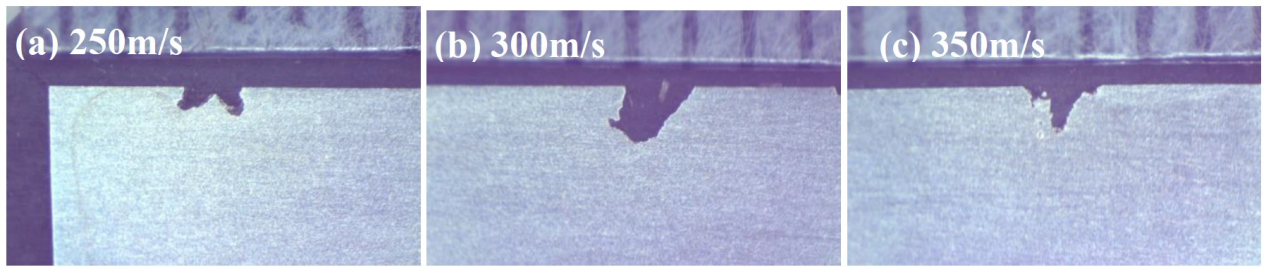
Figure 3-10: Macrographs showing the influence of impact speeds on the observed crater width and depth.

Table 3-4: Summary of the observed accumulated material loss, crater width and depth at different speeds

Impact Speed (m/s)	Experiment stopped after		Accumulated material loss (g)	Crater width (mm)	Crater depth (mm)
	Exposure time (minutes)	No. of impingements x 10^5			
250	415	249	0.0237	1.09	0.50
300	70	50	0.0269	1.28	1.08
350	30	25	0.0353	1.44	1.00

3.4. Erosion mechanism

WDE phenomenon sets-up different material removal mechanisms at various stages of the erosion process. This damage will also depend on the material nature whether it is brittle or ductile, for example. However, the material removal is not well understood due to the difficulty in accurately predicting the hydrodynamic condition that causes particular erosion damage [10]. The individual stages during the erosion process merge into one another without any noticeable transition. For this reason, the present investigation carefully explored the important stages of the erosion such as the early stage of erosion damage (damage initiation stages) and advanced stages as shown in Figure 3-11. Regions A and B in Figure 3-11a represent the early stages of the damage and advanced stages, respectively. Figures 3-11b and 3-11c show the isolated pits during the early stages. It is important to note that at a moderate impact speed test (200-300 m/s) more apparent features can be observed as compared to a severe test. Based on the forgoing point, SEM images revealed several features

obtained from different WDE tested conditions. This is to fully understand the mechanism of material removal during the erosion process.
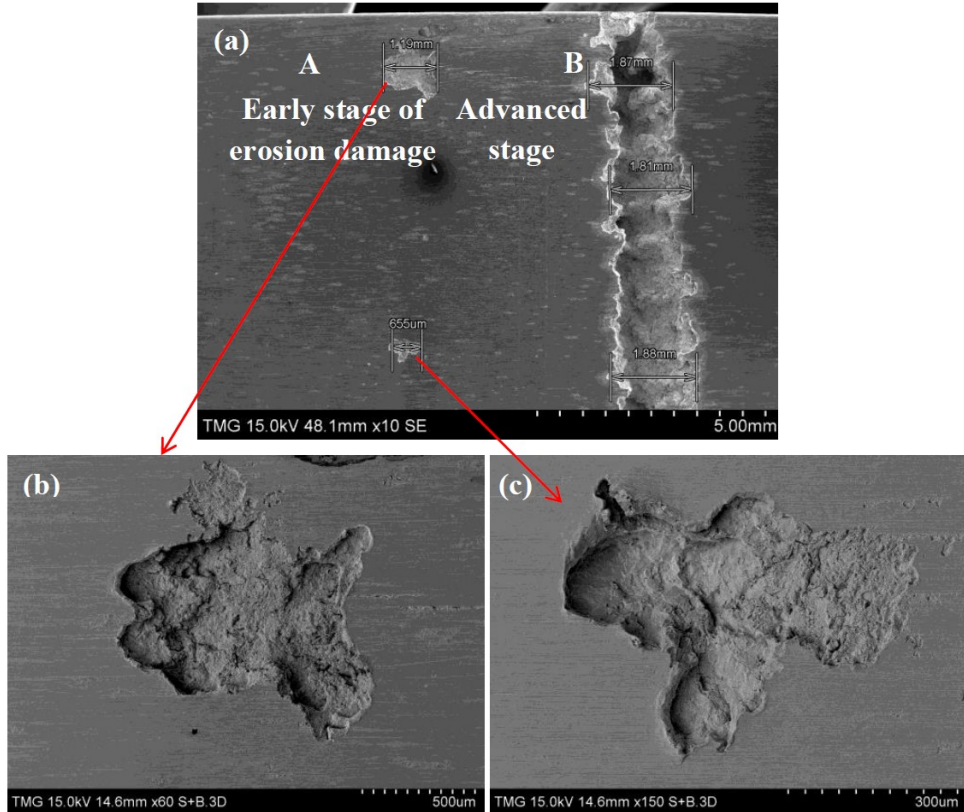
Figure 3-11: SEM showing (a) typical erosion initiation and advanced erosion stages and (b-c) isolated pits during early stages of erosion damage.

3.4.1. Early stages of erosion damage

Based on the SEM observations, it was found that the formation of a shiny erosion line, isolated erosion pits of different dimensions, asperity formation and network of microcracks were the predominant features during the damage initiation period. Other features such as grain tilting resulting in grain boundary damage were also reported by Kamkar [9]. Nevertheless, as pointed out earlier that the definition of incubation stage (start and end) depends on the observer and this might vary significantly. For instance, it was believed that when the plastic deformation limit is reached and with more energy (kinetic energy) supplied to the target, erosion initiation starts [18,123]. It is worth noting that for plastic deformation to occur, the dynamic yield strength of the target material must be exceeded [34]. The plastic

deformation induces high local concentration of crystalline defects, which induce high internal stresses [123]. With more droplet impacts surface damages such as the microcracks are observed. The initiation of microcracks is an important feature observed at the on-set of the erosion process. Rieger [123] reported that the crack formation occurs when the fracture strength is exceeded. Kamkar [9] reported that the cracks formed due to the high local deformation with conditions related to low cycle fatigue (LCF). Ma *et al.* [11] attributed the formation of surface microcracks to synergetic effect of water hammer pressure and stress waves. Figure 3-12a shows how the crack lines are formed due to the repeated droplet impacts. Figure 3-12b shows a typical network of microcracks that was observed and this can be attributed to the aforementioned reasons given by [9,11,123]. These microcracks chip out small amount of material leading to a stress raiser that initiates more rapid failure due to repetitive impacts with sufficient magnitude [30,124]. It is evident from Figure 3-12b that microcracks during the early stages of damage serve as potential sites for favourable pit coalescence and growth and crack propagation [107]. Thus, detachment of larger fragments occurs at later stages in the erosion process due to following impacts and liquid lateral jetting.
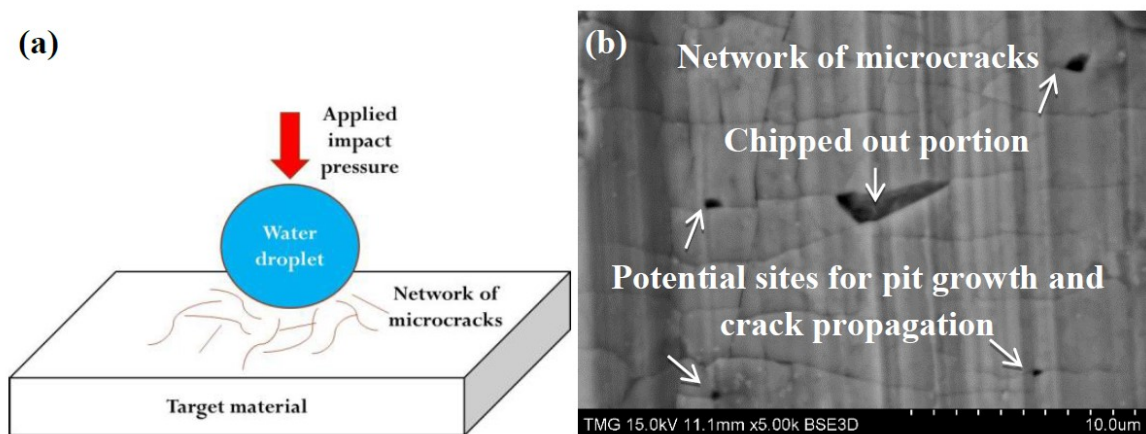
Figure 3-12: Shows the formation of cracks due to droplet impacts (a) and typical network of microcracks (b).

Also, water impingement results in surface depressions, which are typical trademarks associated with the incubation period [19–23]. These depressions are most likely to be observed at low impact velocities whose impact pressures induce stresses greater than the

yield strength of the material [125]. At high velocities, the formed depressions might not be seen due to the severity of the test. Field *et al.* [126] pointed out that these depressions are enlarged with further impacts and in turn produce surface asperities due to repeated liquid lateral jetting. Heymann [18] stated that the high speed lateral jetting interacts with surface irregularities or asperities, thereby causing further crack initiation and damage. Also, Hattori *et al.* [117] mentioned that these asperities are the reasons for the fatigue crack initiation and material removal. Figure 3-13a shows the formation of surface asperities as explained by [18]. Figures 3-13b-c show surface asperities observed during the early stages of the erosion damage after few droplet impacts and accumulated impacts. Figure 3-13c indicates that the asperities further open-up with increased impacts thus, leaving a large cavity on the surface that deepens with time [18]. Here, removal of material by the shearing or tearing mode was observed.
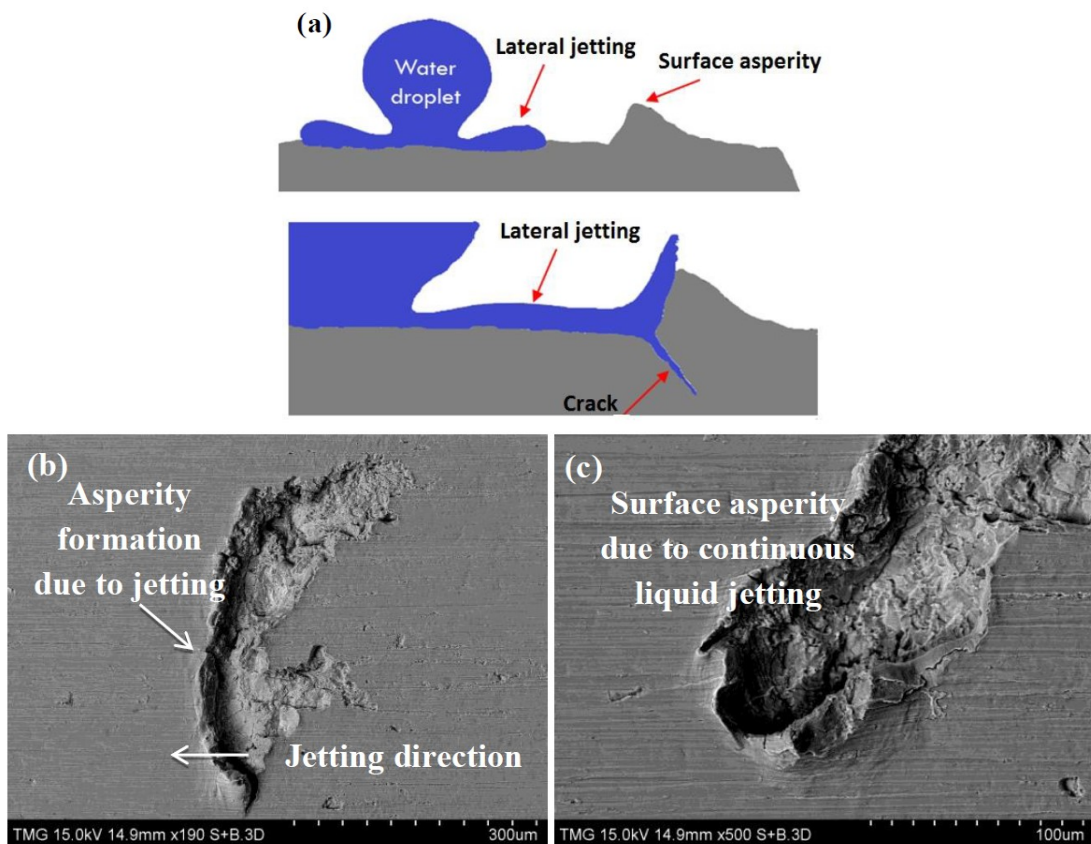
Figure 3-13: Formation of surface asperity [18] (a) typical surface asperities after few impacts (b) and accumulated impacts and continuous lateral jetting (c).

During the erosion initiation stage, isolated pits of irregular shapes and dimensions were found as shown in Figures 3-11b-c and 3-14a. This could possibly suggest the irregularity of the erosion process and the initial surface quality such as different surface imperfections. With repeated impacts on the pits, deeper and wider craters are formed thereby, leading to the advanced erosion stage where significant material is lost. The phenomenon of compression and shear waves is also paramount in understanding the erosion damage. According to the elastic wave theory of solids [15], "when an impulse loading acts on a solid surface, a compression and a shear wave are generated in the bulk solid and on the surface, a Rayleigh surface wave is generated" [16]. As the compression wave travels along a free surface, shear (head) wave is formed. The shear wave offsets the stresses caused by the compression wave. Shi and Dear [127] stated that the liquid lateral jetting causes energetic shear waves in the solid, thereby forming shear bands in sub-layer of materials. Field *et al.* [128] reported that the Rayleigh wave forms circumferential cracks as the liquid jets away. In this WDE study, the droplet impact causes the compression wave while the lateral jetting causes the shear wave. The material folding/upheaving shown in Figure 3-14b could be due to the shear waves. Also, fatigue striation marks are also shown which indicates the fatigue-like damage.
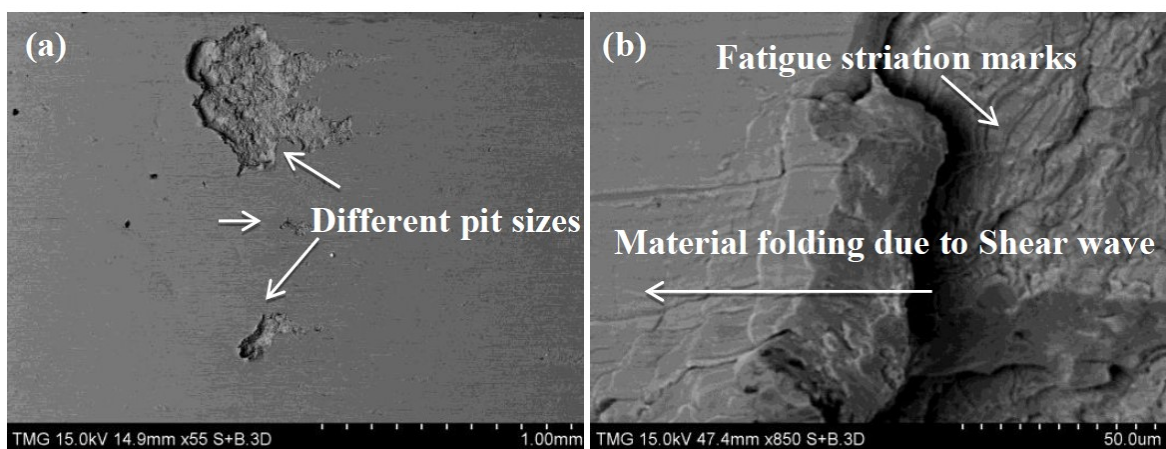
Figure 3-14: SEM micrographs showing (a) different pit sizes and (b) material folding and fatigue striation marks.

These fatigue striation marks are due to the fatigue-based damage caused by cyclic nature of the liquid droplets [9,11,117]. Similar features (material folding and striation marks) were

also observed at the advanced stages of the erosion process [11]. In general, the erosion initiation stage strongly depends on magnitude, duration and frequency of the localized loadings as well as the material's response [124], microstructure [18] and surface quality (roughness) [17,30].

3.4.2. Advanced erosion stage

The advanced stage in this study is shown as region "B" in Figure 3-11a. Figure 3-15 shows several damage features observed during the advanced erosion stage. Significant amount of material was lost due to water droplets impingements. This loss of large chunks of material was due to the hydraulic penetration as indicated by the arrow in Figure 3-15b. This is the penetration of liquid over pre-existing cracks or pits thus, forcing large chunks of material to be removed. Moreover, the hydraulic penetration phenomenon has been observed and reported as the most profound material removal mode in Ti-6Al-4V [11,24–27]. Figure 3-15b also revealed how a sub-surface crack emanated and propagated from beneath the erosion crater to the top surface. This could be due to the interaction of the impacting droplets with sub-surface defects such as cracks. Typical cracks were observed as indicated by the arrows in Figure 3-15c. These cracks could have originated from highly stressed points or damaged grain boundaries. It has been reported that materials are more susceptible to erosion damage if imperfections are present at the grain boundaries [14]. This causes large detachment of grains which leaves a deep void. Material upheaving at the edge of the crater was observed as shown in Figure 3-15d. Adler and Vyhnal [27] observed this material upheaving in their rain erosion experiment and attributed it to the merging of cracks which originated from the erosion pits. However, this can also be attributed to the shear wave propagation due to the lateral (radial) jetting of the liquid.
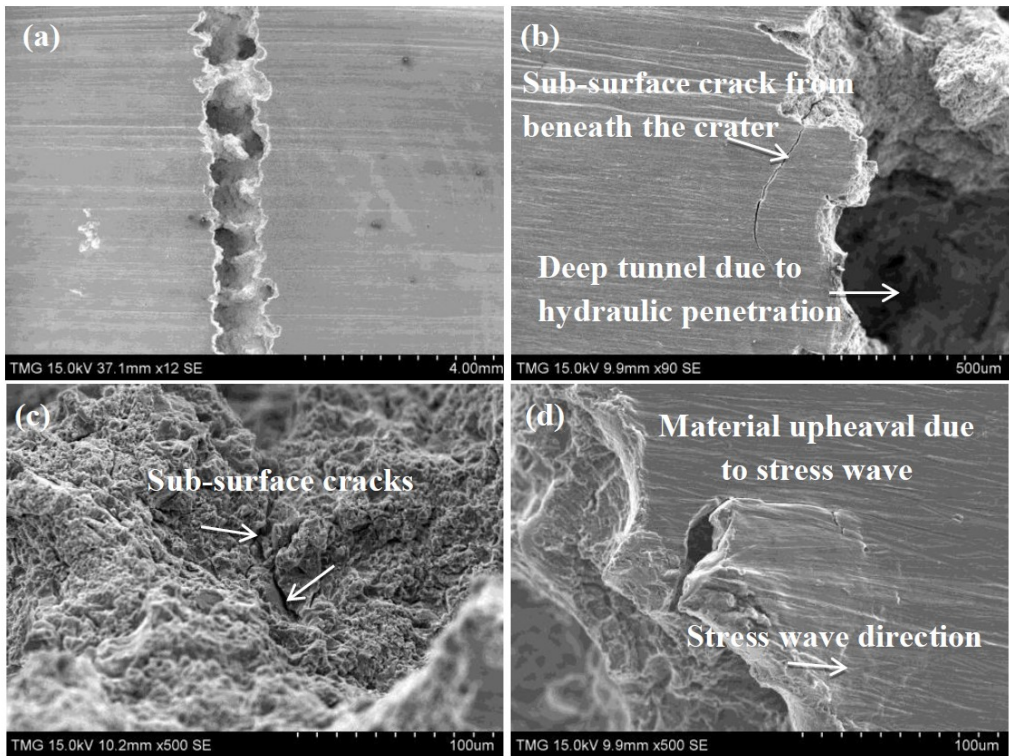
Figure 3-15: SEM showing eroded Ti-6Al-4V coupon during the advanced erosion stage.

It is imperative to show the crater depths and possible interaction between the formed craters at longer erosion times. This approach of observing multiple craters presented in this study might give better understanding in regards to material removal mechanisms as WDE progresses. Hence, crater geometry, interactions and mean depth of craters can be observed fully. Figures 3-16a and 3-16b-c show the crater cross section A-A and the in-depth microstructural features, respectively. One can see different crater depths and geometries (spherical and V-shaped crater at points 1, 2 and 3). These can be attributed to the hydraulic penetration and the irregularity of the erosion process. The deeper craters might have been the initially damaged locations thereby, forming deeper pits and sub-tunnels due to accumulated impacts and lateral jetting, respectively. Other locations (point 4 for instance) showed relatively levelled surface as compared to points 1, 2 and 3. This also confirms the explanation given in section 3.3.3 that the crater depth might vary significantly. The variation in the crater geometries and depths could be additional contributions to the difficulty in fully understanding the process of material damage by erosion.
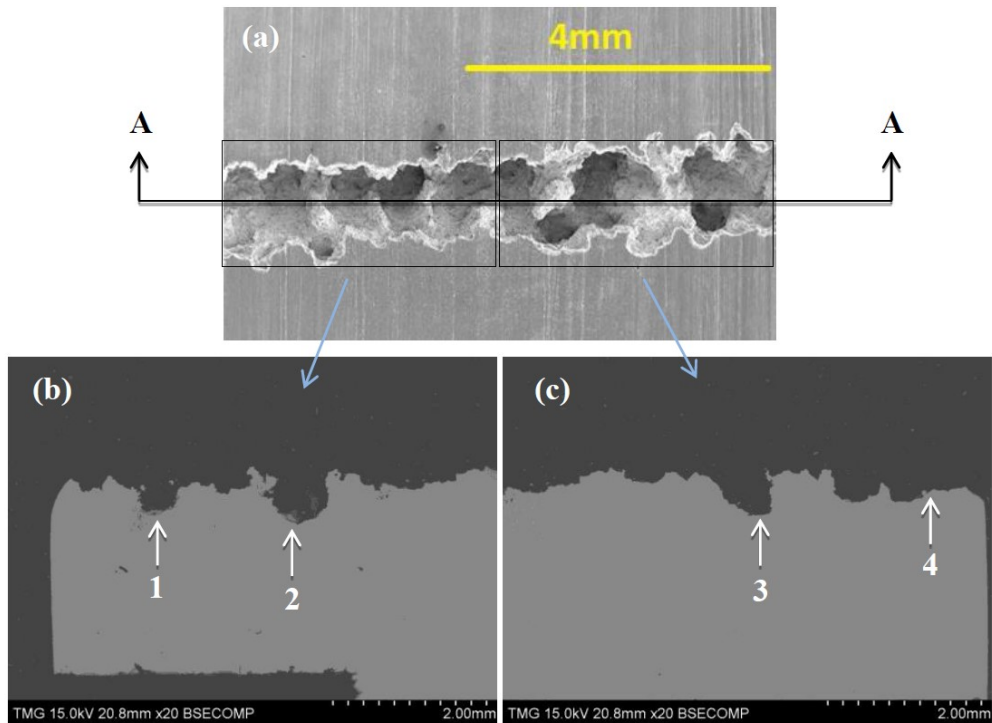
Figure 3-16: (a) the crater section A-A and (b) the in-depth microstructural view during the advanced erosion stage.

Looking closer at the craters shown in Figures 3-16b-c, several other features could be observed. For instance, sub-surface cracks and side wall cracks were observed as shown in Figures 3-17a-b. The sub-surface cracking is a direct consequence of the continuous droplet impact. The continuous impact allows for the interaction between the transmitted (compression) and reflected (tension) stress waves which occurs repeatedly [11]. This leads to the initiation of sub-surface cracks and the propagation of existing cracks. This cracking could be intergranular or transgranular or the combination of both in Ti alloys [14,28,129,130]. Also, due to repeated droplet impacts on existing cavities, secondary pits shown in Figure 3-17c are formed and these are termed as sub-tunnels within the craters [18]. This sub-tunnelling phenomenon has been described and observed by Hammitt and Heymann [10], Mahdipoor *et al.* [130] and Kamkar *et al.* [9]. Furthermore, Figure 3-17d shows the material upheaving/folding due to the stress wave and this is in accord with the top surface feature shown in Figures 3-14c and 3-15d.
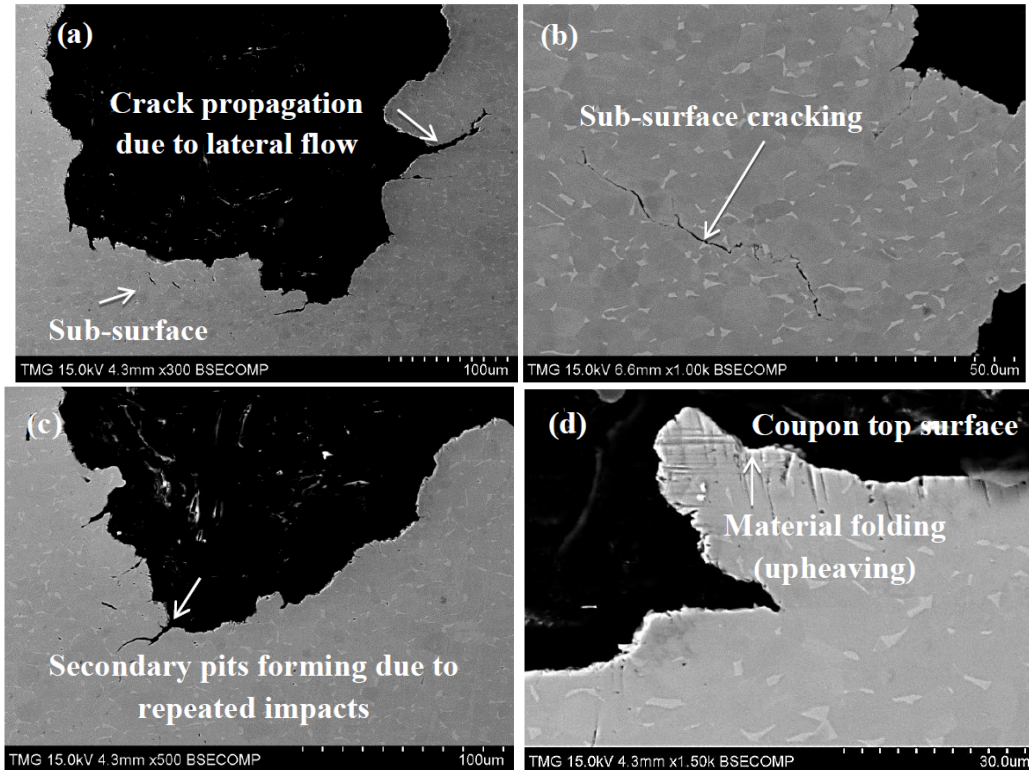
Figure 3-17: Erosion crater showing (a) sub-surface cracks and propagation on the sidewall and base, (b) sub-surface cracking (c) secondary pits formation due to high cumulative impacts, and (d) material upheaving/folding.

Figures 3-18a-c show micrographs taken after 54×10^5, 17×10^5 and 8.4×10^5 impingements at 250, 300 and 350 m/s, respectively. Figures 3-18a-c show side wall cracks which is caused by the liquid lateral jetting. With increased droplet impacts, these side wall cracks propagate removing large chunk of material. This could further highlight the reason why the crater dimensions (width and depth) were increased with increased exposure and severity. For instance, locations X, Y and Z in Figure 3-18 indicate vulnerable portions of the material to be removed with increased impacts. Location Z is the largest portion to be removed compared to X and Y. This could account for the significant mass losses observed when using high impact speeds. Depending on the severity of the test, the liquid jetting effect might show different crater geometries. Hence, observing the influence of the impact speed on this jetting will be paramount. It can be seen from Figures 3-18a-c that the lateral jetting is more apparent with increasing the impact speed even with relatively low number of impingements/less exposure time. For instance, Figure 3-18a shows that the liquid jetting

effect seems to be evenly distributed in the crater for mild erosion conditions ($\leq$250 m/s, for instance). However, Figures 3-18b-c show more jetting effect on one side for more severe test conditions ($\geq$300 m/s). This phenomenon has been observed in several micrographs taken at different erosion conditions. This observation is in accord with the claims made by Lesser and Field [131] that the response of liquid droplet changes corresponding to changes in impact speed. They [131] stated that "if the impact speed is sufficiently low for a given liquid, distinct shocks and high-speed jetting would not be expected" and vice versa.
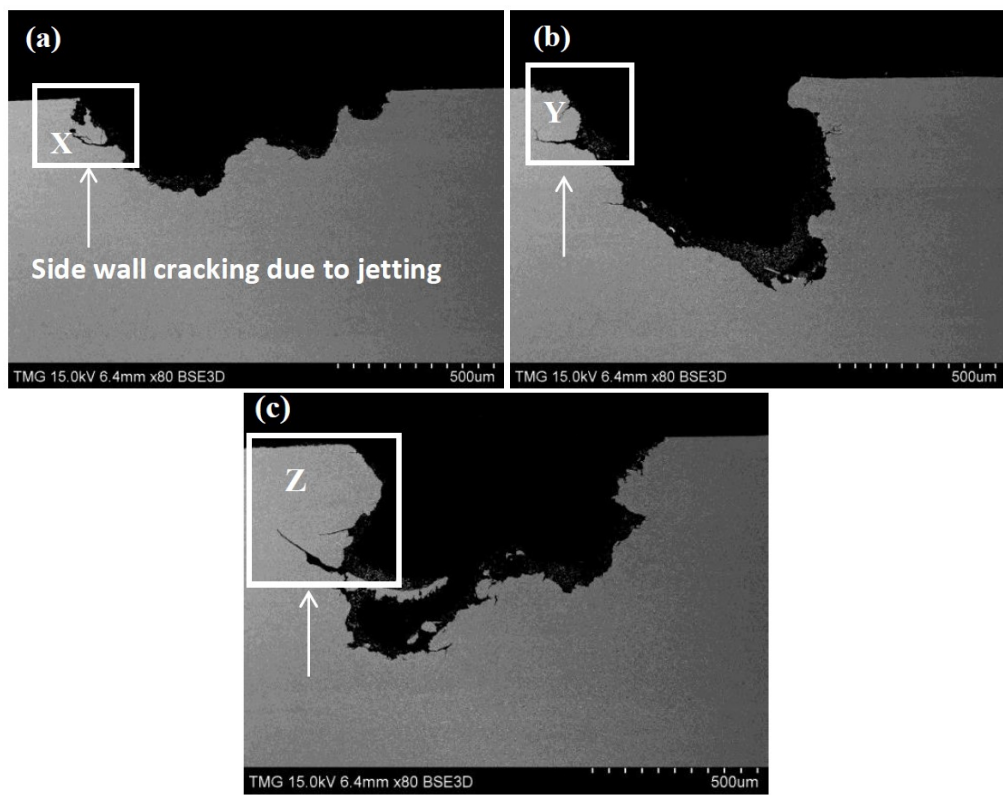
Figure 3-18: SEM micrographs showing craters at (a) 250 m/s (b) 300 m/s and (c) 350 m/s.

Comparatively, the material damage, crater dimensions and surface features during the early stages of erosion damage and advanced stages are different. For instance, during the advanced stage, the crater deepens further while the width has a slow increase with further impacts. This was not the case during the erosion initiation and subsequent stages where both the crater width and depth increased with more impacts.

3.5. Conclusion

The WDE behaviour of Ti-6Al-4V and the mechanism of material removal during the early and advanced stages of erosion damage were studied. The following conclusions could be drawn from this study:

(1) Increasing the impact speed decreases the erosion initiation time and increases the maximum erosion rates (ER_{max}). It was also observed that ER_{max} increases with the 9 to 10th power of impact speed. A threshold velocity range between 150 and 200 m/s was observed after 840 minutes of exposure time corresponding to 30 million impingements.

(2) Erosion crater dimensions were found to be increased with increasing impact speed even at significantly lower number of impingements/exposure time compared to low speed.

(3) Early stage of the erosion damage was mainly limited to the generation of microcracks, isolated pits and formation of asperities.

(4) During the advanced stage, the most profound mode of material removal was the hydraulic penetration. Fatigue striation, side wall cracks, sub-surface cracks, material folding and upheaving were also observed at the advanced stage. Impact speed significantly influences the liquid lateral jetting at the advanced water droplet erosion stage.

Chapter 4 : Effect of Ultrasonic Nanocrystalline Surface Modification on the Water Droplet Erosion Performance of Ti-6Al-4V

A. K. Gujba[a], Z. Ren[b], Y. Dong[b], C. Ye[b], M. Medraj[a,c,*]

[a]Department of Mechanical and Industrial Engineering, Concordia University, 1455 De Maisonneuve Blvd. W. Montreal, Quebec, Canada, H3G 1M8.
[b]Department of Mechanical Engineering, The University of Akron, Akron, OH 45325, USA.
[c]Department of Mechanical and Materials Engineering, Masdar Institute, Masdar City, P.O. Box 54224, Abu Dhabi, United Arab Emirates.
*Author to whom correspondence should be addressed; E-Mail: mmedraj@encs.concordia.ca; Tel.: +1-514-848-2424 (ext. 3146); Fax: +1-514-848-3175.

ABSTRACT

The effect of ultrasonic nanocrystalline surface modification (UNSM) on the water droplet erosion (WDE) performance of Ti-6Al-4V was studied. It was observed that UNSM induces deep levels of compressive residual stresses in both the scanning and transverse directions. The treated surface revealed microdimples in a micro-tracked fashion. Mechanical deformation marks were observed within the grains due to excessive plastic deformation and variation in grain size was observed across the ultrasonically modified layer. Microhardness of the UNSM condition was enhanced significantly as compared with the untreated (As-M) condition. The WDE performance tests for the UNSM and As-M conditions were conducted in a rotating disc rig in accordance with ASTM G73 standard. Influence of impact speed on WDE was explored on two different sample geometries (T-shaped flat and airfoil). WDE results showed that the flat UNSM samples had enhanced WDE performance at speeds 250, 275 and 300 m/s as compared with the As-M condition. At 350 m/s, both UNSM and As-M conditions showed similar performance. UNSM airfoil samples showed mild enhancement in the WDE performance at 300 m/s during the advanced stage as compared with the As-M condition. At 350 m/s, the UNSM airfoils do not show enhancement in WDE performance.

Keywords: UNSM; microhardness; compressive residual stress; WDE; impact speed; Ti-6Al-4V

4.1. Introduction

In the power generation industry, the fogging method employed to cool the intake air into the compressor poses severe erosion damage to the leading edge of the blades. This occurs due to the synergy of the impacting water droplets and rotating blades. This is usually termed as "water erosion by impingement (liquid impingement erosion) or water droplet erosion (WDE)" [6]. WDE is the progressive loss of material from a solid surface due to accumulated impacts by liquid droplets [7]. WDE is a complex phenomenon due to many interacting parameters such as impact speed, droplet size, impact angle and conditions of the target material such as mechanical properties and surface roughness. The main causes of WDE damage are the high pressure exerted by the relative speed between the droplets and the rotating blade and the liquid lateral jetting [10]. The jetting is the radial outflow of the liquid droplets after impact which is identified as a major cause of the erosion damage [18]. Heymann [12] proposed four primary modes of WDE damage, which are plastic deformation and asperity formation, stress waves propagation, lateral jetting and hydraulic penetration. WDE consists of several stages viz: incubation period where mass loss is negligible; acceleration stage (energy accumulation zone [110]) where mass loss is significant; maximum erosion rate stage where mass loss is at its peak and terminal or final steady state with erosion rate declining and remaining constant [12,30]. These stages are further affected by surface roughness [30], mechanical properties [18], microstructure [10], geometry [30] and combination of impact speed and droplet size [30]. In order to prolong the life span of components, the WDE performance of materials such as Ti-6Al-4V must be improved. Ryzhenkov *et al.* [32] stated that the methods of mitigating WDE can be classified into two distinct categories with certain conditions; (1) active (intrinsic) methods which basically minimize the main factors causing the erosion such as reducing the moisture content as well as decreasing the droplet sizes and; (2) passive (extrinsic) methods which aim at enhancing

the surface and mechanical properties of blades' materials. The passive method has been adopted due to its economic feasibility [132]. Despite the efforts to combat or mitigate the erosion damage, it has not been possible to identify or quantify an absolute parameter for WDE resistance [29]. This is due to the fact that erosion rate is not constant with time and therefore, no single value can quantify the erosion performance.

Several surface modification techniques such as coatings [24,33] and laser surface treatments [25,31] have been employed to combat WDE. However, achieving this goal still remains a challenge due to the presence of surface defects and microcracks after surface modification. Mechanical surface treatments such as deep rolling (DR) [11], has recently being explored in this regard. Mechanical treatments are usually employed to enhance the fatigue life of components due to the deep levels of induced compressive residual stresses [34]. However, more work is still needed in order to fully understand the effectiveness of mechanical treatments in combating erosion damage. WDE damage is likened to fatigue-like damage due to fatigue striation marks caused by the cyclic nature of the liquid droplet impacts [11,18,35]. Researchers [9,117,133] have shown that WDE damage mechanisms is influenced significantly by crack initiation and propagation. It is well known that mechanical surface treatments retard crack initiation and propagation as well as enhance fatigue life [34]. Thus, one would expect mechanical surface treatments to combat WDE damage. However, the effect of cold working (strain hardening) before exposing the surface to liquid droplet impacts has been questioned. This is because the mechanical treatments plastically deform the surface and induce strain hardening. Repeated droplet impacts strain harden the material further [10]. Frederick and Heymann [10] stated that the duplication of the work hardening process might show detrimental effects and in another report by Heymann [18], he suggested the opposite trend with the condition that too much cold working should be avoided. To shed more light with regards these claims, a relatively new

mechanical surface modification technique called ultrasonic nanocrystalline surface modification (UNSM) is explored. This technique harnesses ultrasonic vibration energy which converts harmonic oscillations of an excited body into resonant impulses of high frequency [42]. The generated energy from these oscillations is used to impact the work piece. Tungsten carbide (WC) [36,43] or silicon nitride ceramic (Si_3N_4) [42,44] ball tip that is attached to an ultrasonic horn is used to strike/impact the work piece surface at high frequency of up to 20 kHz [42]. Typical impacts on the work piece surface range from 20,000 to 40,000 shots per square millimeter [42]. Other process parameters include static load, number of impacts/strikes, intervals, amplitude and diameter of the ball tip. The high frequency striking of the ball leads to severe plastic deformation of the surface, thereby introducing high density of dislocations [36]. Hence, the top surface and in-depth of the work piece are modified, which improves the mechanical properties. The strengthening effect is due to the plastic strain and refined microstructure [37]. The microstructural refinement after UNSM treatment improves mechanical properties based on the Hall-Petch relationship [45]. Generally, UNSM treatment has shown increased hardness [36–39], reduced grain size [46,48], improved surface quality [37] and deep levels of compressive residual stresses [37,39,42,49]. Based on the aforementioned attributes, UNSM has shown enhanced fatigue life [37–39,49], enhanced cyclic oxidation behaviour of coated Ni-based superalloy (CM247LC) [46], enhanced tribological properties such as wear resistance [42,44,47,48] and lowering of friction coefficients [42,44,47,48] of materials. To this point, no study could be found in the literature regarding the effectiveness of UNSM and the associated attributes on the WDE performance of Ti-6Al-4V or other alloys. Since UNSM process is known to enhance fatigue life of materials and WDE damage is ascribed to fatigue-like mechanism, studying WDE performance of UNSM treated Ti-6Al-4V is worthwhile.

In this work, the effect of UNSM on the WDE performance of Ti-6Al-4V was investigated for the first time. The microstructure, microhardness, induced compressive residual stresses were discussed in relation to the WDE performance. Much attention was given to the influence of impact speed on the WDE performance. The sample geometry is another factor that can influence WDE behaviour, however only flat sample geometry has been explored in the literature [11,24,25,31,33] and the effect of sample geometry on the WDE behaviour could not be found in the literature. The current study addresses this issue by employing two different sample geometries (T-shaped flat and airfoil). Also, the influence of sample geometry and the effectiveness of UNSM treatment on the WDE performance of Ti-6Al-4V are addressed in this work. UNSM processing, sample characterizations and WDE tests are detailed in the following section.

4.2. Experimental procedure

4.2.1. Material and geometry

For the present study, Ti-6Al-4V (ASTM B265, Grade 5) alloy, a typical material for compressor blades in gas turbines, was investigated. Room temperature physical and mechanical properties of this alloy are: elastic modulus (113 GPa), Poisson's ratio (0.342), tensile strength (880 MPa) and melting temperature range (1604-1660 °C) [134]. T-shaped and airfoil samples, as shown in Figure 4-1, were machined in accordance to the sample's geometrical requirement of the WDE testing rig. The T-shaped sample represents the typical flat surfaces commonly used in the literature [11,24,25,31,33]. However, in real gas turbine compressor blade where damage is caused by droplet impacts, the airfoil (aerofoil) geometry represents the leading edge of the compressor blade. For this reason, the airfoil geometry was used in this work. Figures 4-2a and b show the starting microstructure of the Ti-6Al-4V alloy which contains α- and β-phases.
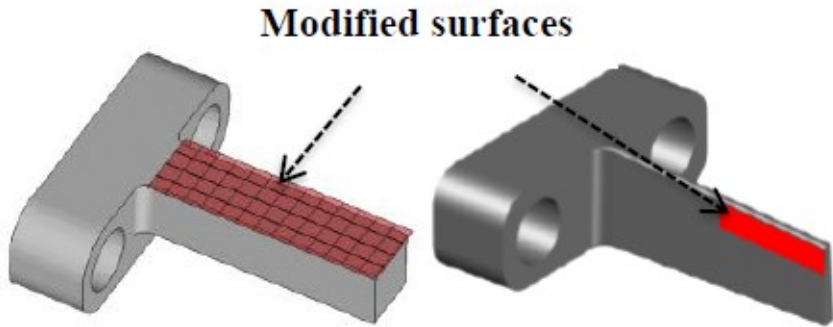
Figure 4-1: Typical T-shaped flat (left) and airfoil (right) samples machined.
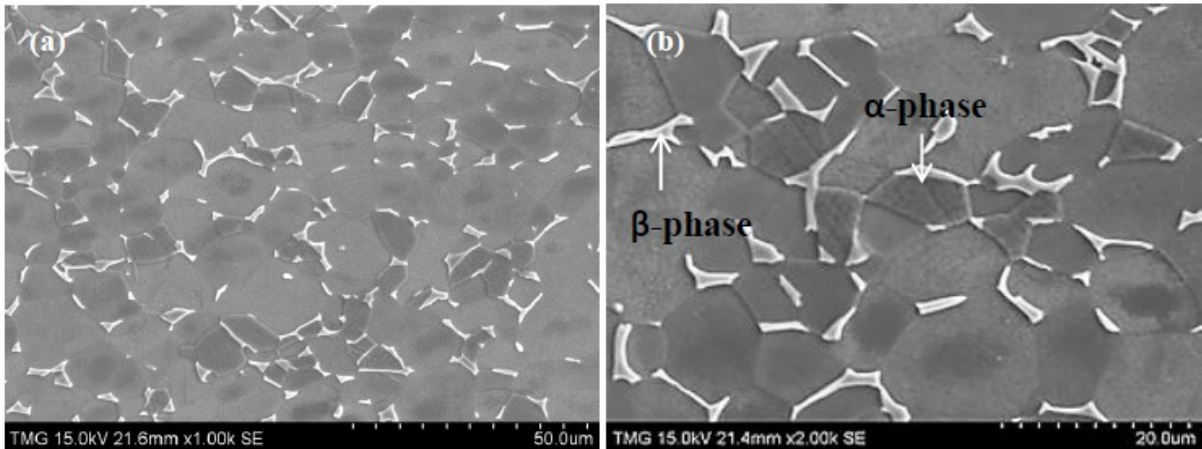
Figure 4-2: SEM micrographs showing the initial Ti-6Al-4V microstructure at (a) lower and (b) higher magnifications.

4.2.2. UNSM treatment and characterization

4.2.2.1. UNSM processing

The as-machined (As-M) samples (T-shaped and airfoil) surfaces were modified using UNSM apparatus at The University of Akron, Ohio, USA. The modified surfaces are indicated by the arrows in Figure 4-1. The airfoil sample was treated on both sides in order to avoid sample distortion. This is the usual practice when applying mechanical surface treatments such as laser shock peening (LSP) on airfoil geometry [135]. UNSM process parameters are summarized in Table 4-1 and are also compared with other UNSM parameters found in the literature [36,42,43]. To observe the effectiveness of UNSM processing, several techniques were used to characterize the untreated and treated samples and are discussed in the following sections.

Table 4-1: UNSM processing parameters for Ti-6Al-4V and study purpose

Reference	Ball material	Diameter of ball tip (mm)	Frequency (kHz)	Interval (mm)	Amplitude (µm)	Study purpose
Amanov et al. [42]	Silicon nitride	2.38	20	0.07	30	Fretting wear and friction reduction
Cho et al. [43]	Tungsten carbide	2.30	20	0.07	30	Fatigue behaviour
Ye et al. [36]	Tungsten carbide	2.60	20	**	**	Mechanical properties and microstructure
Present work	Tungsten carbide	2.40	20	0.01	24	Water droplet erosion performance

**Indicates no information from the reference.

4.2.2.2. Surface roughness

Mitutoyo SJ-210 portable surface roughness tester was used to measure the surface roughness (Ra) before and after UNSM treatment. An average of 5-7 readings was taken across the sample surface. The surface roughness is an important parameter in WDE study because roughness can act as stress raiser or crack initiation sites [34]. Hence, it is recommended to have similar initial surface roughness when comparing the WDE performance of different materials and/or surface conditions.

4.2.2.3. X-ray diffraction pattern and residual stress measurement

X-ray diffraction (XRD) patterns for the untreated and UNSM treated surfaces were acquired in order to observe any phase changes/transformations due to UNSM processing. Phase change/transformation has been reported in material such as 304 stainless steel after UNSM processing [37–39,49]. In this work, the constituent α- and β-phases were monitored before and after processing. The compressive residual stresses before and after UNSM were also measured using the XRD $\sin^2\phi$ technique at Proto Manufacturing Inc., USA. Crystallographic plane of {213} and Bragg's angle (2θ = 142º) obtained by Cu Kα radiation were used for this purpose. For the UNSM condition, the top surface and in-depth residual

stresses were measured relative to the ultrasound scanning directions i.e. parallel (0˚) and transverse (90˚). For the sake of comparison, the top surface residual stresses for the As-M condition were also measured using these two directions. To quantify the residual stress values with respect to depth, surface layers were gradually removed by electropolishing. Strain gradient correction and layer removal corrections were carried out in accordance with SAE J784a standard [136]. Total depth of 0.26 mm was measured with initial fine steps of 0.03 mm down to 0.15 mm followed by two coarser steps of 0.06 mm down to 0.21 mm and of 0.05 mm down to 0.26 mm. More information on the residual stress measurements using the $\sin^2\phi$ technique can be found in the standard [136].

4.2.2.4. Microhardness

Microhardness measurements were carried out on the top surface and cross-section of all treated and untreated samples. A direct load of 50 gram-force (gf) and a dwell time of 15 seconds were used. Prior to the hardness measurements, the samples (treated and untreated) were cut perpendicular to the surface using a diamond cutter. Under cooling and lubricating fluid conditions, low speed and moderate load were applied in order to minimize unwanted surface modifications during cutting. After mounting, silicon carbide grit papers from 400 to 800 were used for grinding and vibratory polishing with 1 μm diamond paste was employed to remove scratches and other undesired debris.

4.2.2.5. Microstructure investigations

To observe any surface features such as microdimples, the as-treated top surface was observed under SEM (S-3400N, Hitachi). Also, the cross-section of the as-treated condition was observed using optical microscope. For surface and in-depth microstructure investigations, Kroll's reagent containing 2 ml HF + 5 ml HNO_3 + 100 ml H_2O was used to etch the vibratory polished samples. Etching time of 15 seconds was chosen in order to have a balance between details and contrast as recommended by Gammon *et al.* [137]. SEM images

of the polished-etched top surface and cross-sections for both treated and untreated samples were taken at different magnifications.

4.2.3. WDE testing and characterization

4.2.3.1. WDE tests

A rotating disc rig available at Concordia University, shown in Figure 4-3a, was used for studying the WDE performance of the treated and untreated Ti-6Al-4V. In this study, the untreated Ti-6Al-4V is used as a reference. Details about this unique erosion rig has been reported in [28,133]. The test was conducted in accordance with the ASTM G73 standard [29]. In this rig, the untreated and UNSM treated samples were fixed at diametrically opposite ends of the rotating disc as shown in Figure 4-3a. To avoid vibration during testing, difference in sample weight not exceeding 0.05 g was maintained. It is worth noting that the surface roughness of both treated and untreated samples was similar prior to testing. Two types of nozzles as shown in Figure 4-3b were used depending on the geometry to be tested. A shower head nozzle was used for testing the airfoil samples, whereas a single streak nozzle was used for testing the T-shaped flat samples. Typical WDE testing parameters are summarized in Table 4-2. Once the desired rotational speed was obtained, the water droplets (de-ionized water) were introduced while controlling the flow rate. The setup enabled the droplets to impact the samples at 90° in a repetitive fashion. The impact angle of 90º causes the most severe water erosion damage [109]. The erosion exposure time depended on the impact speed, nozzle type and sample geometry. For instance, for the T-shaped flat, 1 minute constant time intervals were used in order to capture the early stages of the erosion process (initiation stage). Whereas, longer time intervals of 2, 3, 4, 6, 10, 12, 30, 60 and 75 minutes were employed as the test progressed to the advanced stages of erosion. For the airfoil, intervals of 2, 3, 4, 6, 8, 10, 12, 15, 18, 20, 24 and 30 minutes were used.
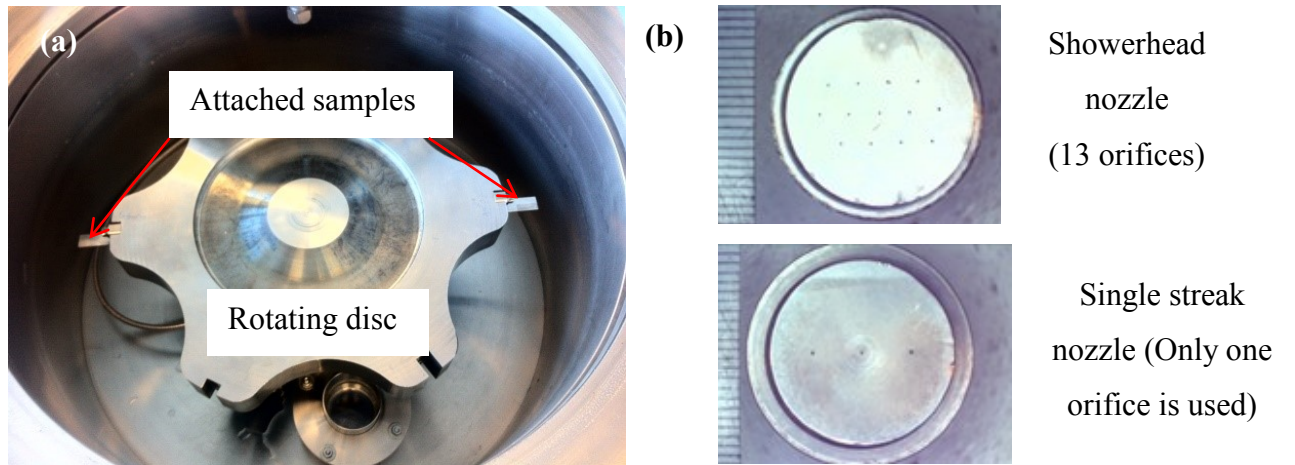
Figure 4-3: Water erosion rig (a) and nozzles used (b).

Table 4-2: WDE test parameters used in the present work

WDE parameters	Flat sample	Airfoil sample
Impact speed (m/s)	250, 275, 300, 350	300, 350
Rotational speed x 10^3 (rpm)	10, 11, 12, 14	12, 14
Flow rate (liter/min)	0.05	0.15
Nozzle head type	Single streak	Shower head
Stand-off distance (mm)	5	5
Average droplet size (µm)	463	460
Impact angle (°)	90	90

4.2.3.2. Water droplet erosion behaviour

During the WDE tests, experiments were halted at certain intervals and eroded samples were weighed using a balance having ±0.2 mg accuracy. Typical erosion curves such as cumulative mass loss *versus* exposure time/number of impingements, maximum erosion rate (ER_{max}) *versus* impact speed and number of impingement to erosion initiation *versus* impact speed were plotted. For satisfactory determination of the incubation period and ER_{max}, a three line representation method [12] demonstrated in Figure 4-4a was used. In Figure 4-4a, the ER_{max} denoted as "B" is the slope of the best line fit of the data points in the maximum erosion stage, whereas the incubation period denoted as "A" is the intersection of the straight line with the x-axis (exposure time axis) [29]. To observe the erosion rate as the erosion test

progressed, the instantaneous erosion rate (ER_{inst}) which is the slope between two consecutive points on the erosion-time graphs were plotted (Figure 4-4b). It is important to note that the incubation period, ER_{max} and ER_{inst} are analyzed in this study. To understand how the erosion process evolved, images were taken using a standard stereo optical microscope at the intervals during which mass loss was measured.
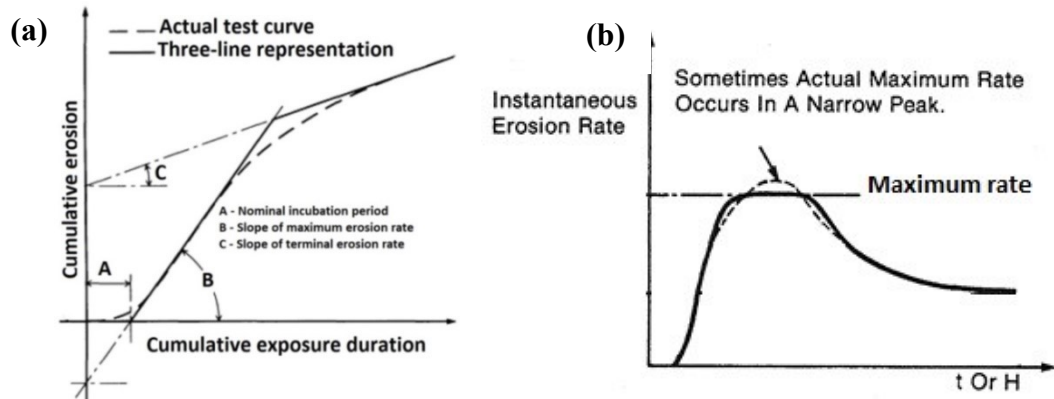
Figure 4-4: WDE curve characterization using (a) three line representation [12] and (b) ER_{inst} [29].

4.3. Results and discussion

4.3.1. Effect of UNSM on surface and in-depth characteristics

UNSM treatment has been considered as an effective and economically viable method for producing nano-corrugated [138] and nanostructured [47] surface layers. This is due to the accompanied grain refinement. Properties and microstructure of the modified layers can be controlled by careful selection of process parameters such as static load, amplitude, diameter of the ball tip and interval. In this study, interval of 0.01 mm, static load of 30 N, amplitude of 24 μm and tip diameter of 2.4 mm were used for the UNSM treatment. The effect of UNSM process on the surface roughness, XRD pattern, compressive residual stress, microstructure and microhardness were investigated and reported in this paper.

4.3.1.1. Surface roughness

The average surface roughness (Ra) values before and after UNSM treatments were recorded. Five different locations across the treated and untreated surfaces were measured

and average Ra value was taken. Ra values of 0.71±0.06 µm and 0.26±0.02 µm were observed before and after UNSM, respectively. It can be seen that the surface roughness after UNSM treatment was reduced significantly (about 63 % reduction). Also, the UNSM showed a relatively uniform roughness across the surface. This observation is also in accord with the findings of [37,44,45,47,48,139]. The surface roughness can further be controlled by varying parameters such as static load [42] and number of strikes [45]. It can be said that UNSM treatment improves surface quality. However, this is not the case in other processes such as shot peening (SP) and LSP where the control of surface roughness and surface defects is still a challenge [34]. For comparative studies such as wear and fatigue behaviour of materials, the surface roughness of treated and untreated samples should be made comparable [37,38,44]. To study WDE, the untreated samples were also polished to a comparable surface roughness similar to the UNSM samples. An average Ra value of 0.25±0.03 µm is used for the untreated samples in this work and more on this is discussed in section 4.3.2.

4.3.1.2. XRD pattern and compressive residual stresses

The XRD patterns of the untreated and UNSM conditions are as shown in Figure 4-5, where reduced peak intensity and peak broadening are observed for the UNSM condition compared with the untreated material. Full width half maximum (FWHM) approach was employed to quantify the peak broadening. For instance, analysing the first three peaks in Figure 4-5, FWHM values were quantified. For the untreated condition, 0.26, 0.22 and 0.36 were obtained for first, second and third peaks, respectively. Similarly, for the treated condition, 0.48, 0.48 and 0.55 were obtained. It has been reported that reduced peak intensity and peak broadening are due to the high induced strains, causing severe plastic deformation and grain refinement [140–142]. Figure 4-5 clearly indicates that UNSM treatment is one of such processes that induce severe surface layer of plastic deformation.
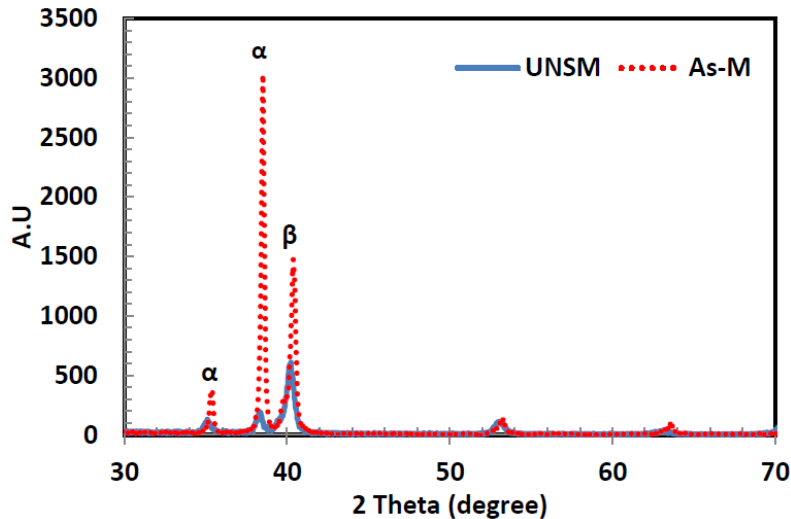
Figure 4-5: XRD patterns for the As-M and UNSM treated surface.

The compressive residual stresses in the 0 and 90° directions before and after UNSM were measured. Surface of the As-M condition showed -490±19 MPa and -607±9 in the 0 and 90° directions, respectively. The UNSM surface showed -863±18 MPa and -1582±28 MPa in the 0 and 90° directions, respectively. UNSM condition showed higher top surface compressive residual stress in both directions than the As-M condition. This is due to the local plastic deformation and induced strain hardening during UNSM processing [49]. Similar top surface residual stress has been observed elsewhere on UNSM-treated Ti-6Al-4V [42]. Also, due to machining, grinding and polishing, the observed surface compressive residual stresses for the untreated condition is expected. Chou *et al.* [143] demonstrated that surface finishing techniques such as grinding and polishing can induce different levels of compressive residual stresses. Variation of the compressive residual stress with depth was measured for the UNSM condition. Figure 4-6 shows the observed stress profile and it can be seen that compressive residual stresses were induced into the material down to 0.25 mm. Similar variation in residual stress has been reported on UNSM treated Ti-6Al-4V [42,43]. Depth of compressive residual stress down to 0.15 mm [42] and 0.16 mm [43] was observed. It is also shown that the stresses in 0 and 90° directions were different. For instance, comparing the magnitude of the compressive residual stresses from the top surface to 0.12

mm depth, stresses in 90° direction were higher than in the 0° direction. However, beyond 0.12 mm depth, residual stresses in both directions were relatively similar. The observed compressive residual stresses induced via UNSM are due to the surface and sub-surface deformation. Compressive residual stresses extend into the subsurface of the target material through dislocations multiplications and their interactions [34]. It has been pointed out that increasing the frequency of ball striking and load increases the macroscopic compressive residual stresses [36,45]. Contrarily, a decrease in compressive residual stresses was observed after applying very high static load [38]. Hence, careful selection of process parameters is required for optimized UNSM process.
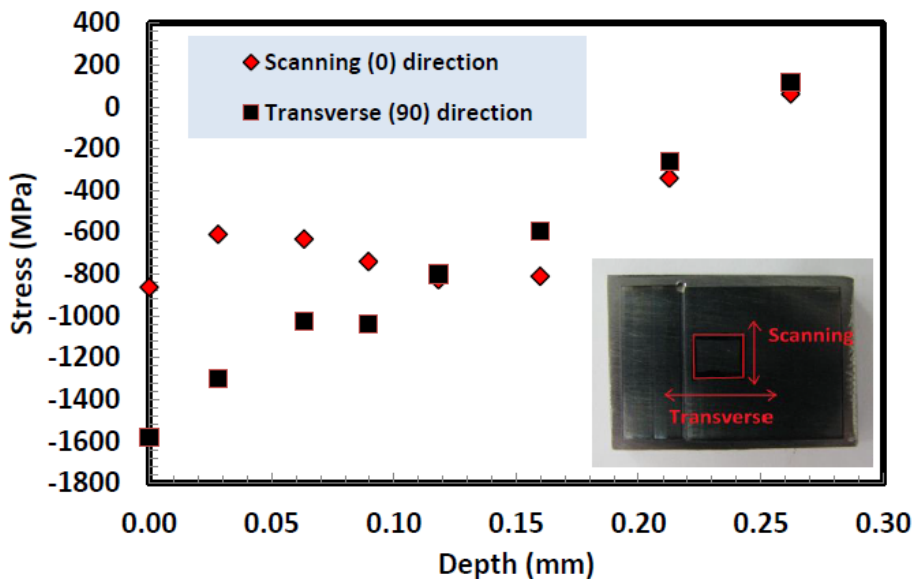
Figure 4-6: Variation of top surface and in-depth compressive residual stress profile.

4.3.1.3. Microstructure characteristics

The SEM micrographs in Figure 4-7 show that UNSM treatment produces microdimples and microtracks on the surface. Microdimples are indentations produced due to the ball impact which causes severe plastic deformation during processing [47,139]. They are usually 1-2 µm in diameter [144] and formed in a micro-tracked fashion (Figure 4-7) which can be attributed to the controlled processing parameters such as scanning interval. However, varying the interval induces different microtracks and microdimples patterns and

consequently, different material properties/behaviours [145]. Microdimples have shown significant effect on tribological characteristics such as reducing the friction coefficient and the wear volume loss [144].
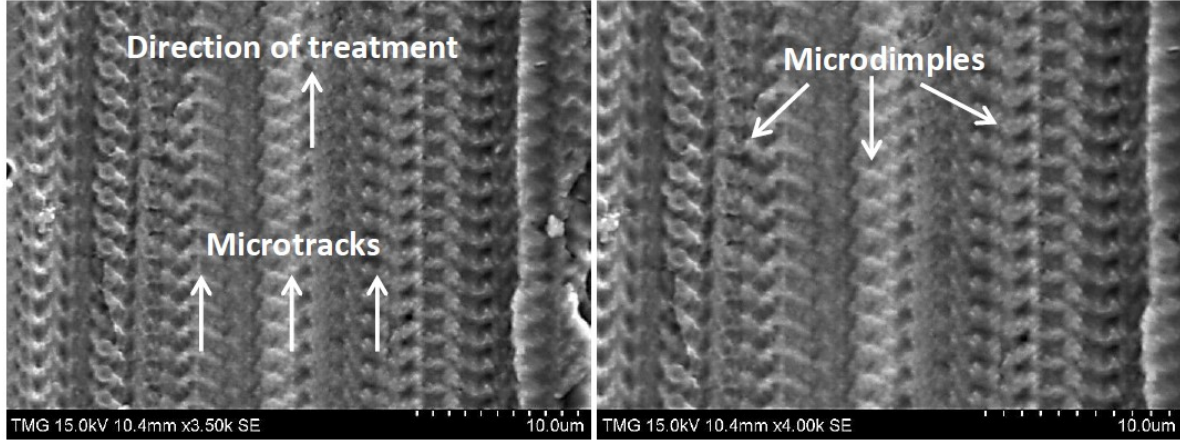
Figure 4-7: SEM micrographs showing microtracks and microdimples on ultrasonic modified surface.

Also, due to the severe plastic deformation during UNSM processing, surface and sub-surface layers in the material are significantly changed. Figure 4-8a shows optical macrograph of the cross section after UNSM treatment, whereas Figure 4-8b shows a schematic illustration of the layers of a typically UNSM modified material.
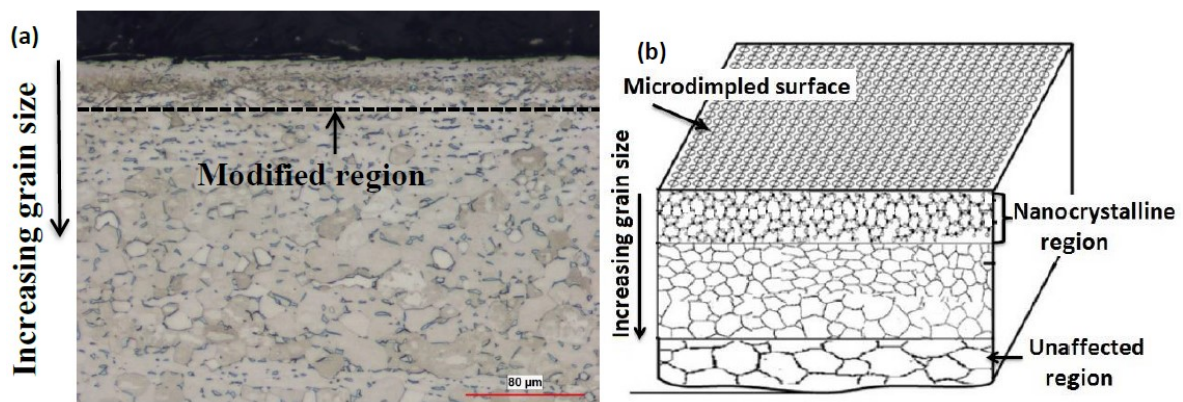
Figure 4-8: (a) optical macrograph of typical UNSM sample and (b) schematic illustration of structure characteristics and grain size profile on UNSM treated condition.

The modified region in Figure 4-8a indicates that the coarse-grain structure has been deformed significantly [144]. It can be seen from Figure 4-8a that the effectiveness of the UNSM treatment is reduced with respect to the depth. In other words, an increase in the grain

size away from the deformed region until the unaffected region is observed as shown in Figure 4-8b. The grain refinement, in conjunction with the accumulation of dislocation, causes the enhancement in mechanical properties such as microhardness. Similar to other mechanical surface treatment techniques such as LSP, SP, DR and LPB, plastic deformation and induced strain after UNSM occur in a gradient manner, with the top surface showing the highest plastic strain followed by a gradual decrease into the material [49]. It is important to note that the plastically deformed layer shown in Figure 4-8a could be increased by increasing the striking number and/or amplitude [36]. However, over processing may deteriorate the desired properties too.

Figures 4-9a-b shows the polished and etched top surface of the untreated and treated samples. Figure 4-9a shows un-deformed grains and the β-phase is surrounding the α-phase in a uniformly distributed fashion. However, Figure 4-9b shows fragmented and elongated β-phase and the grain boundaries were less apparent. This could be due to the deformation of grains that resulted in the modified microstructure. Amanov *et al.* [42] also reported similar modified microstructure in Ti-6Al-4V after UNSM with the grain boundaries less apparent. Their [42] micrographs showed that the initially continuous β-phase was fragmented. Mechanical deformation marks in the grains were formed (Figures 4-9b, c and d) after UNSM treatment due to the induced high strain and strain rate [36]. Location A in Figures 4-9c and d clearly show the formation of the deformation marks within the grains. Figures 4-9e and f show the cross-sectional micrographs of the untreated and treated conditions, respectively. Figure 4-9e shows relatively un-deformed grains across the depth, whereas Figure 4-9f shows the deformed or modified layer of about 30-40 μm at the top surface. This is attributed to the effectiveness of the UNSM technique in producing relatively deep modified layers.
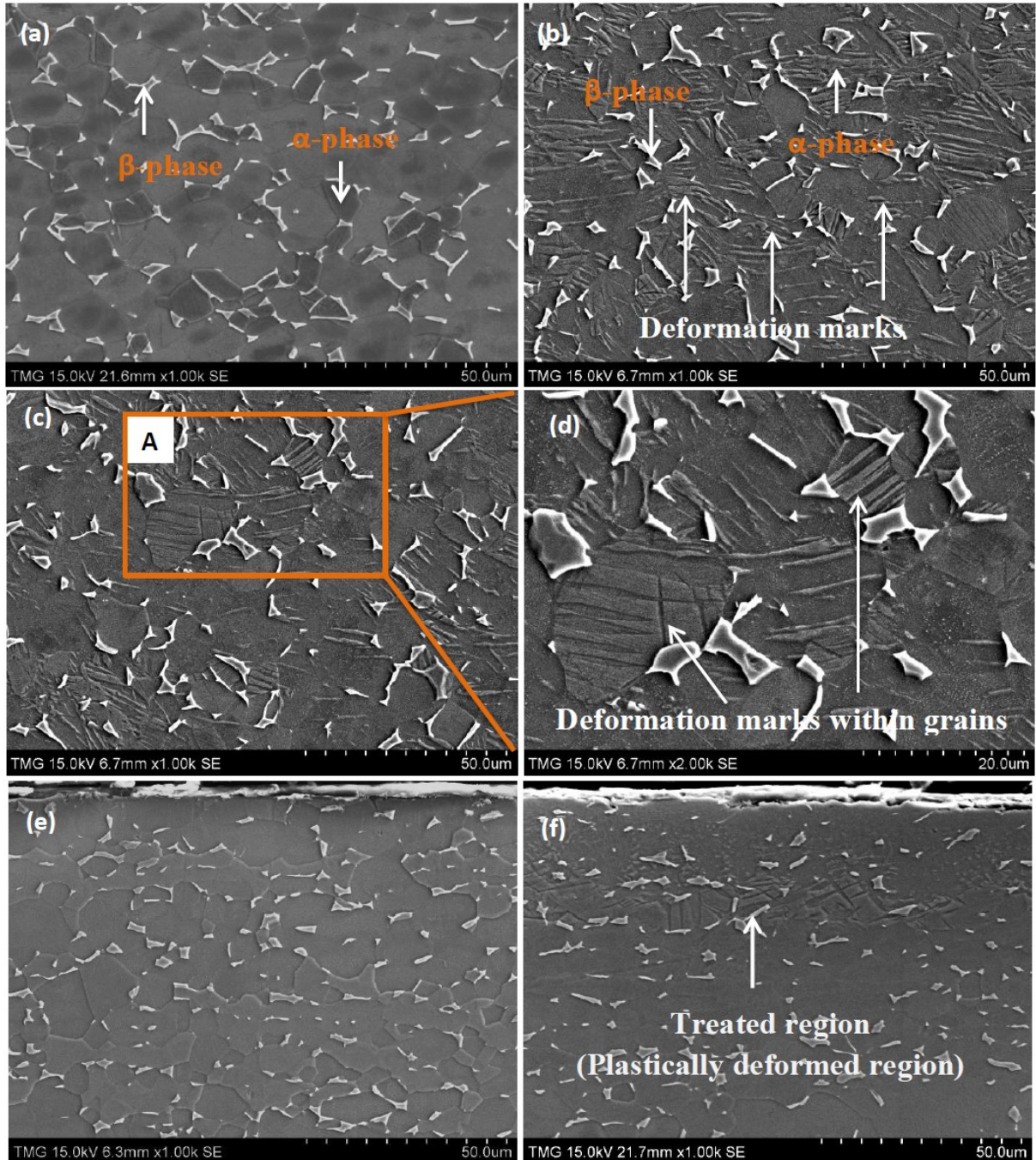
Figure 4-9: SEM micrographs showing polished and etched (a) untreated top surface (b, c, d) UNSM treated top surface (e) untreated cross-section and (f) UNSM treated cross-section.

4.3.1.4. Microhardness

As mentioned in section 4.2.2, a 50 gf load was used to measure the top surface and in-depth microhardness. Microhardness at 7-8 locations were obtained across the depth of UNSM and As-M samples. At each location, the average and standard deviation of 4-5 readings were calculated. Figure 4-10 shows the microhardness values for untreated and

UNSM conditions. It is clear that the UNSM condition showed enhanced microhardness as compared with the untreated condition. The top surface microhardness values were 331±5.3 HV and 379±7.6 HV for untreated and UNSM conditions, respectively. Furthermore, the microhardness can further be enhanced by varying UNSM parameters such as scanning interval [42] and number of strikes [45]. This increases the depth of the deformed layer, thus increasing the microhardness [36,45]. It is important to note that the highest microhardness value of 427±16.83 HV was observed 30 μm below the top surface. This is also shown in the optical macrograph embedded in Figure 4-10. To confirm the aforementioned trend, another treated sample was measured and similar microhardness trend was observed. Amanov *et al.* [42] also reported similar variation in microhardness below the surface of UNSM treated Ti-6Al-4V. This could be due to the additional work hardening during cutting, polishing and grinding. Zaden *et al.* [146] showed microhardness increase below the surface of Al6061 after cutting in dry, wet and mist conditions. They [146] attributed this trend to the increase in surface deformation which further increased the work hardening effect. For the treated conditions, the microhardness values decreased steadily after the plastically deformed layer.
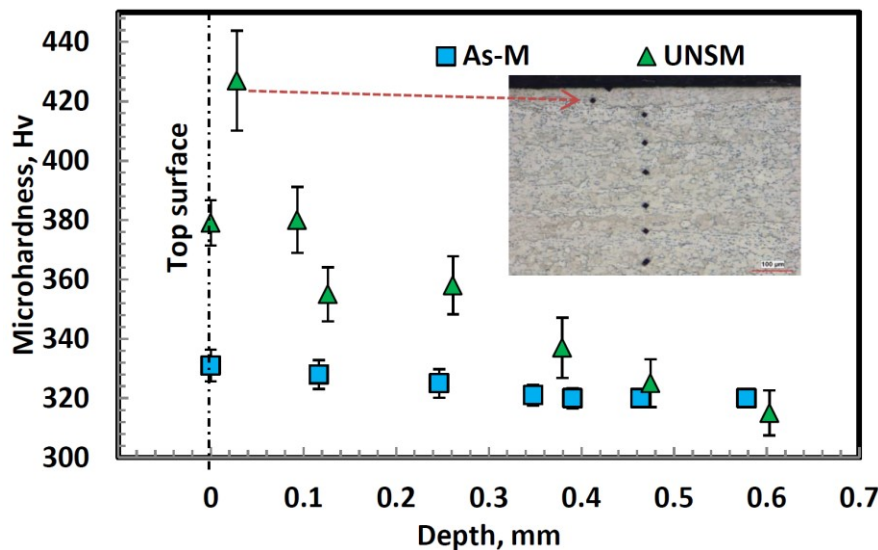
Figure 4-10: Variation of microhardness with depth for treated and untreated samples.

In general, the increase in microhardness after UNSM can be attributed to the grain refinement and work hardening effect. This observation is in accord with UNSM treatment on

70

Ti-6Al-4V [36,43], medium carbon steel (S45C) [45], austenitic stainless steel (SUS 304) [38] and magnesium alloy (AZ91D) [48]. Hence, the surface and in-depth features observed in Figures 4-5 to 4-10 are used to help understand the WDE performance of the As-M and UNSM conditions. The WDE results are detailed in the following section.

4.3.2. Water droplet erosion

Prior to the WDE tests, the As-M flat samples were polished to a similar surface finish as the UNSM samples. The average Ra for the polished and UNSM samples were approximately 0.25±0.03 μm and 0.26±0.02 μm, respectively. This was done because the presence of surface defects or imperfections such as scratches has an influence on the WDE behaviour of materials. Heymann [30] emphasized the influence of surface roughness on the erosion behaviour of materials. He [30] stated that the presence of surface asperities or irregularities facilitates the erosion initiation. This is because irregularities on the surface act as stress raisers and potential sites for pit formation and growth. Also, due to the high speed lateral jetting which interacts with surface irregularities or asperities, further crack initiation and material damage are observed. Hence, better surface quality delays the crack initiation and material damage. For instance, Kirols *et al.* [17] studied the influence of initial surface roughness on the WDE behaviour of 12 % Cr-Steel and Ti-6Al-4V. For the Ti-6Al-4V, samples with average initial surface roughness values (Ra) of 0.30, 0.12 and 0.04 μm were tested. They [17] reported that merely polishing the surfaces prior to WDE tests delayed the erosion initiation and in some cases, decreased the maximum erosion rate. In this work, polishing was done in order to reduce the effect of surface roughness.

For the T-shaped flat samples, UNSM *versus* the polished As-M samples were tested. For simplicity, the polished-As-M samples are referred to As-M (untreated) samples for all the WDE tests. At each WDE testing condition (mentioned in Table 4-2 and section 4.2.3.1); two coupons (As-M and UNSM) were tested at the same time in order to investigate their WDE

performances. The main parameter that was varied was the impact speed while keeping other parameters constant. Here, impact speeds of 250, 275, 300 and 350 m/s were selected. This is because the predominant factor in the material damage is the impact speed [111,133]. This is attributed to the increased kinetic energy ($\frac{1}{2}mv^2$) with increasing the speed. The cumulative mass losses *versus* the number of impingements graphs were plotted. The number of impingement was determined using Equation 4-1.

$$N_{imp} = R \times E_t \times N_{droplets} \qquad\qquad (4-1)$$

Where N_{imp} is the cumulative number of impingements during an exposure period, R is the rotational speed (rpm), E_t is the erosion exposure time (minutes) and $N_{droplets}$ is the number of droplets impacting the sample per revolution. For the flat sample geometry in this work, $N_{droplets}$ is 6. Detailed procedure on the droplet generation, droplet size distribution and number of droplets hitting the sample can be found in reference [133]. For the airfoil samples, only impact speeds of 300 and 350 m/s were used. Here, 350 m/s was chosen as the most severe condition, whereas 300 m/s was chosen in order to have a less severe testing condition and also, to avoid prolonged testing. Tests using impact speed of 250 and 275 m/s for airfoil geometry would mean testing for prolonged erosion time without significant mass loss. Therefore, tests at these speeds were not performed. Contrary to the flat sample geometry, there is a challenge of quantifying the number of droplets hitting the airfoil sample. This is due to the shower head nozzle used during testing. Hence, graphs of cumulative mass loss *versus* number of cycles were plotted. The number of cycles is simply the rotational speed (rpm) multiplied by the erosion exposure time (minutes). It is worth noting that the amount of water used after certain time interval can be computed by multiplying the number of cycles by the flow rate.

It is worth mentioning that there are two threshold speeds in relation to erosion damage i.e. first and second threshold speeds [133]. The first threshold speed is the speed below

which no apparent damage is seen. However, the definition of this speed is somehow subjective and depends on the testing conditions such as impact speed, droplet size and number of impingements. More information regarding first threshold speeds with regards to different applications such as liquid impingement erosion for pipe wall thinning, liquid jet impact, WDE for compressor blade applications has been addressed by the authors in [133]. The second threshold speed is the speed at which mass loss is measurable. In this work, all the selected impact speeds are speeds at which measurable mass losses are observed.

In order to verify the repeatability of the WDE experiments, tests at 250 and 350 m/s with 463 µm droplet size were conducted. For each test speed, the samples had similar surface quality and each test was conducted twice. Also, for each test speed, the two tests are designated as test 1 and test 2. Figure 4-11 shows the WDE curves for test 1 and test 2 for both speeds. It can be seen that for each test speed, the curves coincided for most of the data points, indicating an acceptable level of repeatability.
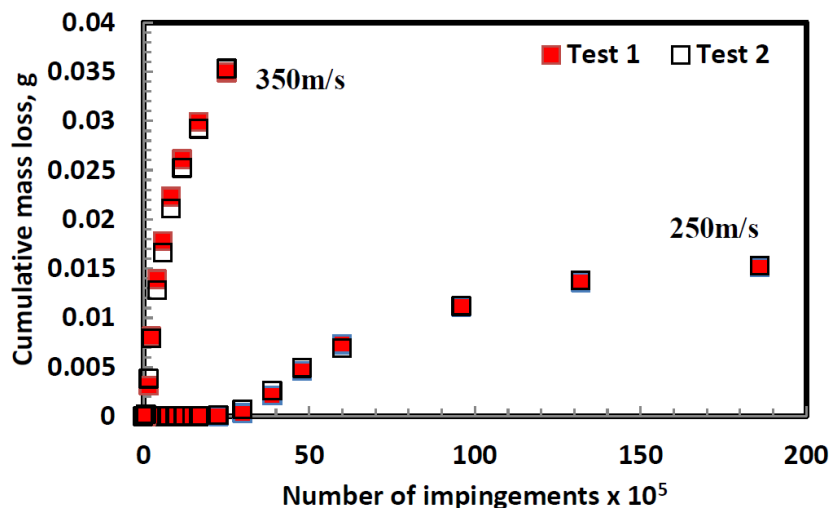
Figure 4-11: WDE curves showing the repeatability of the results at 250 m/s and 350 m/s.

4.3.2.1. WDE performance of UNSM and As-M T-shaped sample conditions

Figure 4-12 shows the cumulative mass loss *versus* number of impingements graphs for the flat samples. The graphs compare the WDE performances of UNSM and As-M samples tested at different speeds.
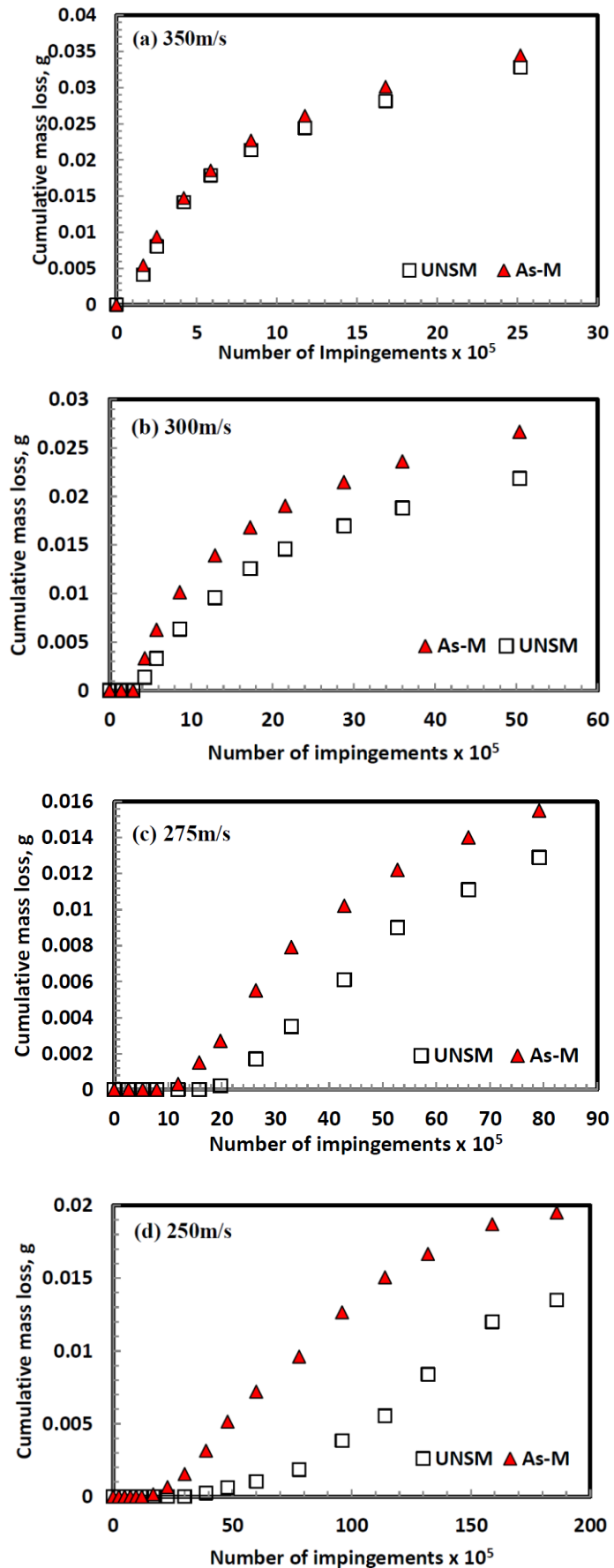
Figure 4-12: WDE curves of As-M *versus* UNSM flat samples at different impact speeds.

Figure 4-12a shows that similar WDE performance was observed at 350 m/s for UNSM and As-M samples. In other words, both conditions are exhibiting similar erosion trend in terms of initial mass loss and subsequent stages. This can be attributed to the severity of the WDE test conditions. Therefore, the UNSM treatment showed little or no beneficial effect in enhancing WDE performance at such high impact speed. At 300 m/s (Figure 4-12b), UNSM showed a much better WDE performance as compared with the As-M condition. At 275 and 250 m/s (Figure 4-12c-d), UNSM condition showed significant improvement in WDE performances at all stages of the erosion process as compared with the As-M condition. Based on the graphs shown in Figure 4-12, the effect of UNSM treatment on the WDE performance of Ti-6Al-4V was observed at impact speeds of 250, 275 and 300 m/s. However, this was not the case at impact speed of 350 m/s.

Based on the three line representation (Figure 4-4a), the influence of impact speed on the erosion initiation and ER_{max} is shown in Figures 4-13a and 4-13b, respectively. It can be seen from Figure 4-13 that reducing the impact speed from 350 to 250 m/s delayed the erosion initiation time and showed less ER_{max}. In other words, as the speed is decreased from 350 to 250 m/s, more droplet impingements are required in order to initiate erosion damage in both conditions. Comparing the As-M and UNSM conditions at 250 m/s, 6 million droplet impingements were required for erosion initiation for the UNSM condition as compared with 2.1 million droplet impingements required for the As-M condition, indicating better WDE performance of the UNSM condition at this speed. As the impact speed is increased, the number of impingements for erosion initiation is significantly reduced for both conditions. At 350 m/s, the number of impingements to initiate erosion for the UNSM and As-M samples was the same, indicating the effect of the speed on the erosion initiation. When comparing the ER_{max} for the UNSM and As-M samples (Figure 4-13b), UNSM condition showed less ER_{max} at impact speeds ≤300 m/s as compared with the As-M condition. However, at 350m/s, both

conditions showed similar ER_{max} due to the severity of the erosion test. The relationship between erosion rate and impact speed has been discussed and emphasized in the literature [110]. This dependency between the maximum erosion rate and impact velocity can be expressed using Equation 4-2. Based on the power law relationship in Equation 4-2, the speed exponent n can be determined.

$$ER_{max} \propto V^n \qquad (4-2)$$

Where ER_{max} is the erosion rate, V is the impact speed and n is the speed exponent. For metals, typical exponent values range from 5-7 in the literature [110,111]. However, based on Figure 4-13b, exponent values of 11.2 and 12.1 were observed for the As-M and UNSM samples, respectively. The values observed in this study are different from the values observed by Kamkar [9] and Mahdipoor *et al.* [28] for Ti-6Al-4V. This discrepancy can be attributed to the test conditions, initial surface quality of the samples and the starting microstructure. The higher value shown by the UNSM condition indicates higher dependence on impact speed and more sensitive to the change in speed than the As-M condition. The impact damping capacity and fracture toughness of the UNSM surface are reduced. This hypothesis is in accord with the explanation given by Ma *et al.* [11] in their study on the WDE performance of deep rolled Ti-6Al-4V.
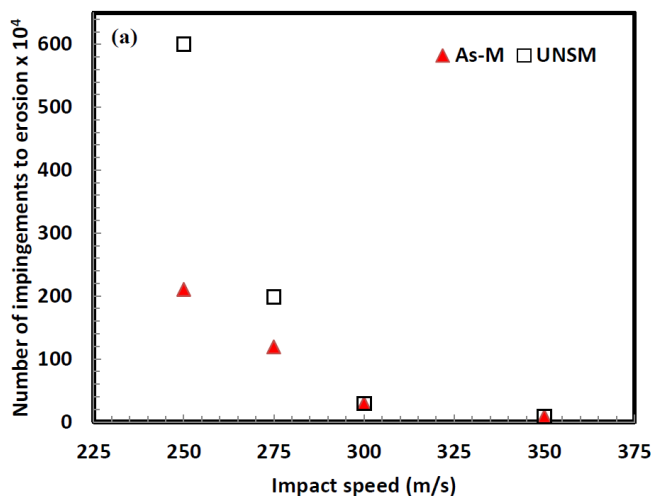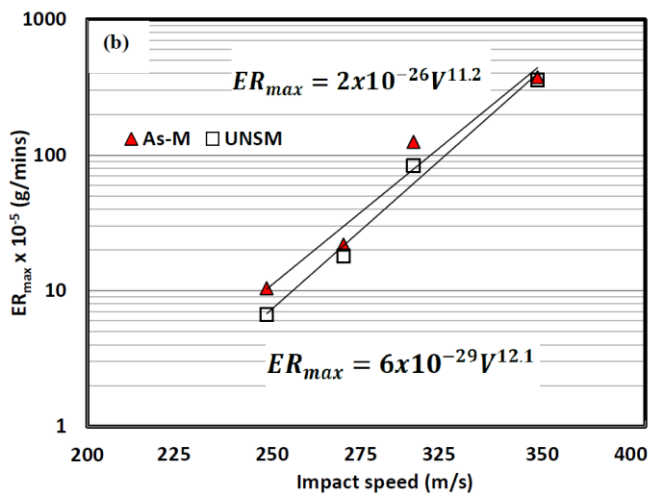
Figure 4-13: Effect of impact speed on (a) number of impingements to initiation and (b) ER_{max}.

Interestingly, using the instantaneous erosion rate approach (Figure 4-4b), the variation of erosion rates with increase in exposure could be traced clearly. Figure 4-14a-d shows the ER_{inst} *versus* number of impingements at different speeds. It can be seen that the As-M condition had higher ER_{inst} and maximum ER_{inst} than the UNSM condition at all speeds. The maximum ER_{inst} is the highest points on the graphs (Figure 4-14). At 350 m/s, the ER_{inst} were very close for both conditions. Also, Figure 4-14 shows that the maximum ER_{inst} was not reached after the same number of impingements/exposure for the UNSM and As-M conditions. In other words, the As-M condition reached its maximum ER_{inst} much earlier than the UNSM condition. Table 4-3 shows the aforementioned maximum ER_{inst} trends and the number of impingements at which the maximum ER_{inst} occurred for the treated and untreated conditions. Table 4-3 indicates that UNSM condition required more droplet impingements to reach its maximum ER_{inst} at all speeds. It is important to note that this insight is missed by the three line representation (Figure 4-4a) because it only uses a straight line to determine the ER_{max}. Therefore, for comparative erosion studies, it is recommended to observe and report the ER_{inst}.
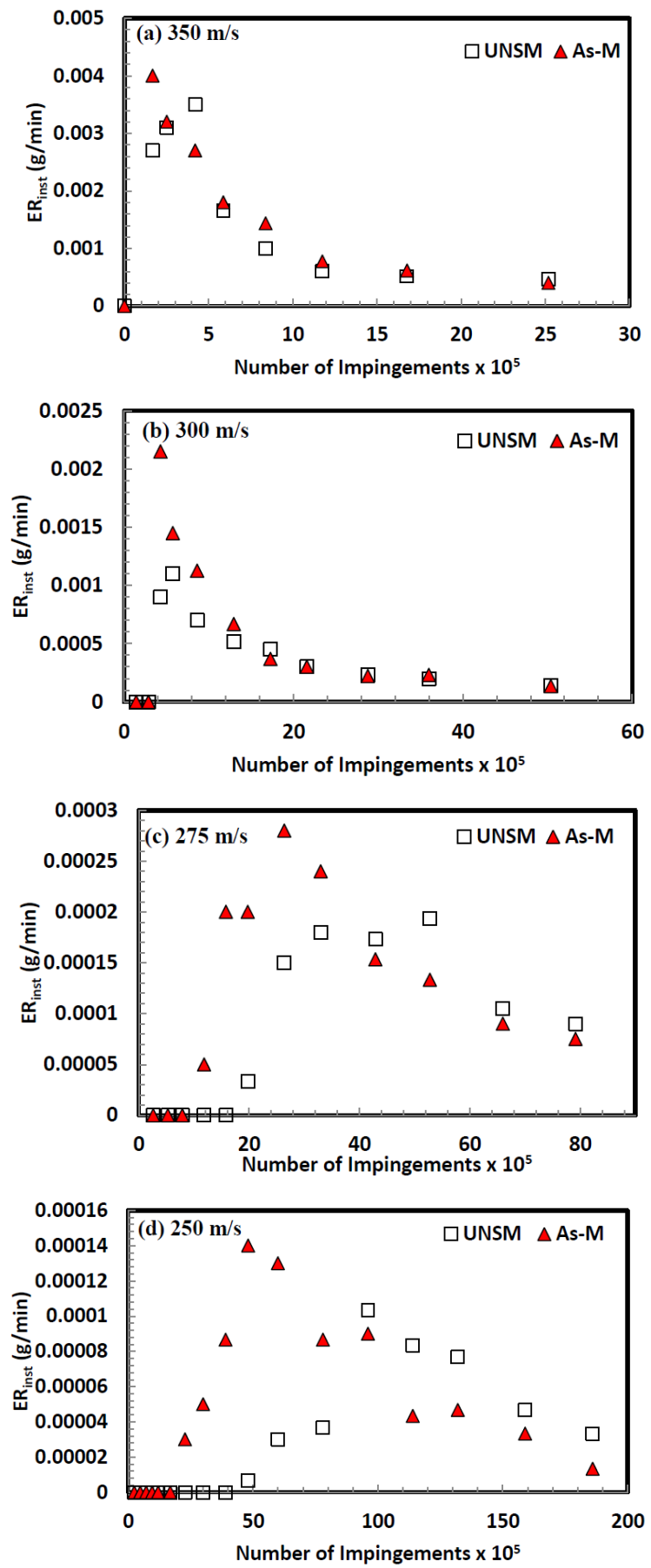
Figure 4-14: ER_{inst} *versus* number of impingements at different impact speeds.

78

Table 4-3: Characterization of the ER_{inst} curves at various speeds

Impact speed (m/s)	Condition	ER_{inst} x 10^{-5}	N_{imp} x 10^5
250	As-M	14	48
	UNSM	10	96
275	As-M	28	26
	UNSM	19	53
300	As-M	215	4
	UNSM	110	6
350	As-M	400	2
	UNSM	350	4

Based on Figures 4-12 and 4-14 and Table 4-3, the general trend is that UNSM (T-shaped) samples showed enhanced WDE performance than the As-M samples at impact speeds 250, 275 and 300 m/s. However, at 350 m/s, both treated and untreated conditions showed similar WDE performance. This trend is in accord with the observations of Mahdipoor *et al.* [24] where they studied the WDE performance of HVOF sprayed coated and uncoated Ti-6Al-4V. Impact speeds of 250, 300 and 350 m/s were employed and their [24] results showed that at speed of 250 m/s, the coated condition had enhanced erosion performance compared to the uncoated condition. At 350 m/s, similar erosion performance was observed for the coated and uncoated conditions [24]. In another study, Mahdipoor *et al.* [28] studied the influence of impact speed on water droplet erosion of TiAl (Titanium Aluminide) compared with Ti-6Al-4V. They [28] showed that TiAl had superior WDE performance compared to Ti-6Al-4V at 275 and 300 m/s impact speeds. Again, at 350 m/s, they [28] showed that the superiority of TiAl over Ti-6Al-4V was reduced significantly.

In this study, as the impact speed is increased from 300 to 350 m/s, the effectiveness of the UNSM treatment diminished. This can be attributed to the increased impact pressure which induced high internal stresses. This pressure is usually termed as 'water hammer pressure' which is the induced pressure exerted by the "arrested" liquid droplet on the solid

surface. This observation is in accord with the explanation given by Thiruvengadam and Rudy [110], Mahdipoor *et al.* [24,28], Ma *et al.* [11] and Kamkar [9]. The exerted pressure strongly depends on the impact speed employed. Sanada *et al.* [113] reported that pressure distributions depend on Mach number (*Mi*) ranges. They [113] stated that the difference in pressure at the center and edge of the droplet is minimum for low *Mi* (between 0.1 and 0.4). For high *Mi* (>0.4), the edge pressure is 3 times that of the center when liquid jetting occurs [16,114]. In this study, the calculated Mach number is within the low *Mi* range. Moreover, high *Mi* range will only be achieved at impact speeds greater than 550 m/s based on the assumptions in [113]. Nevertheless, the initiation period will be influenced greatly by the exerted impact pressure. According to Heymann [12,13], this pressure can be considerably higher than the yield strength of many alloys especially at high impact speeds. For instance, Equation 4-3 provides a reasonable critical impact pressure by incorporating the shock wave velocity for rigid and elastic surface [13].

$$P = \rho C V \left(2 + \frac{(2K-1)V}{C} \right) \qquad\qquad (4 - 3)$$

Where P is the pressure (MPa), ρ is the density of the liquid (kg/m^3), C is the acoustic velocity of the liquid (m/s), V is the impact velocity (m/s), and $K = 2$ for water up to impact Mach number of 1.2. Incorporating values of 250 m/s, 275 m/s, 300 m/s and 350 m/s for V; water hammer pressures of 919, 1032, 1148 and 1392 MPa were obtained, respectively. Based on the calculated pressure values, it can be seen that the impact pressure increases linearly with the impact speed. Due to the high pressure at high speeds, the effectiveness of the UNSM treatment will be reduced significantly. For this reason also, similar erosion initiations for both the UNSM and As-M samples were observed for impact speeds 350 m/s (Figure 4-12).

Highlighting the phenomenon of stress wave propagation could possibly explain the observed trends in Figure 4-12. During the initial droplet impacts, part of the impact energy

transmits through the solid until it reaches a discontinuity. This discontinuity can either be grain boundaries, inclusions and/or cracks. In this work, the deformed region due to UNSM treatment represents a discontinuity. At the discontinuity interface, part of the stress wave travels as transmitted waves, whereas the remaining part travels back in the opposite direction as reflected waves. As the erosion process evolves, the surface is continuously impacted by the liquid droplets and the transmission and reflection of the stress waves occur repeatedly. Hence, the transmitted and reflected waves interaction results in high tensile stress waves that cause crack initiation and propagation of existing cracks [11]. Due to the high frequency of the liquid impacts at high speeds, the stress wave interactions will be very fast and the magnitude of the resulting tensile stress waves will be high. However, the stress wave interactions will be reduced greatly as the impact speed is reduced, thereby reducing the magnitude of tensile stress wave. This is the scenario when the impact speed was reduced from 350 m/s to 250 m/s, where the effectiveness of the treatment was realized.

The enhanced WDE performance observed in this study at speed 250, 275 and 300 m/s are mainly attributed to the increased microhardness and modified microstructure. Heymann [18,30] stated that microhardness is a good and reliable material property used in assessing the resistance of materials to erosion damage. Reports [18,109] have shown that the erosion resistance varies with 2nd to 3rd power of Vickers hardness number. More so, refined microstructure or reduction in grain size has also been associated with erosion resistance of materials [106,109]. Materials having small finely distributed and hard particles are resistant to erosion especially in elastic and ductile matrix [18]. For treated Ti-6Al-4V, microhardness and refined microstructure have been considered among the most influential parameters improving the WDE performance. For instance, Yasugahira et al. [147] studied the water erosion resistance of pure Al and a range of titanium alloys. They [147] attributed the higher resistance of Ti alloys to the high Vickers number. Similar investigation was carried out by

Robinson *et al.* [26] who reported that the resistance was due to the 10 % increase in hardness and the refined microstructure. In this work, it has been shown that UNSM treatment enhanced the surface and in-depth microhardness (Figure 4-10) and the modified surface and in-depth microstructure (Figures 4-8a, 4-9b, 4-9c and 4-9d). For these reasons, UNSM condition showed enhanced WDE performances as compared with the As-M condition at speeds <350 m/s. The effect of micro-dimpled surface (Figure 4-7) might also have contributed to the enhanced WDE performance. This is due to the fact that micro-dimpled surface has shown enhanced tribological characteristics. For instance, Amanov *et al.* [144] studied the influence of micro-dimples on the tribological behaviour of thrust ball bearing in a ball-on-disc test rig. The upper ring of the thrust bearing was used as the disc specimen and a rotational speed of 100 rpm was employed. Comparing the UNSM treated surface with ground surface, their [144] results showed that UNSM treated (micro-dimpled) surface had reduced wear volume loss as compared to the ground surface. Also, the friction coefficient of the UNSM-treated surface was reduced by about 25 %. The effect of micro-dimples might be extended to WDE applications especially at very low speed such as 150m/s. However, more experimental work is needed.

Since UNSM treatment involves work hardening similar to SP, LSP, LPB and DR, it enhances mechanical properties such as hardness. Heymann [18] stated that processes involving work hardening such as pressing, rolling or hammering might be beneficial in resisting erosion damage. However, excessive work hardening might show detrimental effects. In another report, Frederick and Heymann [10] stated that processes involving peening might not be very effective in enhancing the WDE behaviour of materials especially during the incubation stage. They [10] argued that the peening process involves plastic deformation which work hardens the surface and during droplet impingements, repeated plastic deformation further work hardens the surface. The duplication of the work hardening

process at the incubation period might be detrimental to the WDE behaviour [10]. Heymann [30] further stated that the first plastic deformation retards erosion initiation while the second promotes the erosion initiation. The first and second plastic deformations balance each other, thus a non-enhanced WDE performance will be observed. Ma *et al.* [11] reported the WDE performance of untreated and deep rolled Ti-6Al-4V. Despite having improved hardness after the deep rolling process, both the untreated and treated conditions had the same WDE performance. They [11] suggested that there are two competing mechanisms at the initiation stage which balance out one another. These competing mechanisms are the work hardening process from the deep rolling process and the compressive residual stresses. While work hardening decreases the erosion resistance due to the increased brittleness, the presence of compressive residual stresses is expected to improve WDE resistance by delaying crack propagation. For this reason, no enhanced WDE performance was observed for the deep rolled treated condition. This is in accord with explanation given in [30] who pointed out that a non-enhanced WDE performance maybe observed due to duplication of the working hardening process. However, the results presented in this work showed contradictory trends to the arguments in [10,30]. For instance, changing the severity of erosion test conditions such as varying impact speed, different erosion behaviour may prevail. This is the situation observed in this work where enhanced WDE performances were seen at speeds <350 m/s. Contrary to Frederick and Heymann [10], the incubation (erosion initiation) stage (Figure 4-13a) in this work was significantly delayed for the UNSM treated sample at such varied conditions. Moreover, the ER_{max} (Figure 4-13b and 4-14) was reduced significantly at these conditions. It can be inferred that the severity of the erosion conditions must be taken into consideration when evaluating the suitability of certain service treatment to combat WDE.

Another reason for the observed trends in this study and [11] is the level of induced plastic deformation during UNSM and DR processing. It might be that the amount of plastic

83

deformation from the DR technique is higher than the UNSM technique. Due to the increased strain hardening, the DR treated material will be more brittle than the UNSM treated material. In this case, the UNSM condition will accommodate more plastic deformation from water hammering than the DR condition during the initiation stage.

It has been shown that UNSM induced deep levels of compressive residual stresses (Figure 4-6). However, it is not guaranteed that the induced stresses are beneficial in enhancing WDE resistance. In this case, extensive work is still needed in order to fully understand the influence of compressive residual stresses on WDE performance.

4.3.2.2. WDE performance of UNSM and As-M airfoil sample conditions

Similar to the WDE investigations on the flat T-shaped samples, As-M and UNSM-treated airfoil samples were studied. However, the WDE tests were conducted perpendicular to the UNSM-treated surface and a shower head nozzle of 460 μm droplet size was used. Figures 4-15a and b show a schematic illustration of the WDE testing direction with respect to the airfoil treated surface and a typically eroded UNSM airfoil, respectively. The nozzle contained 13 orifices where water droplets are introduced. Due to the difficulty in accurately accounting for the number of impingements when using a shower head, the number of cycles was used.
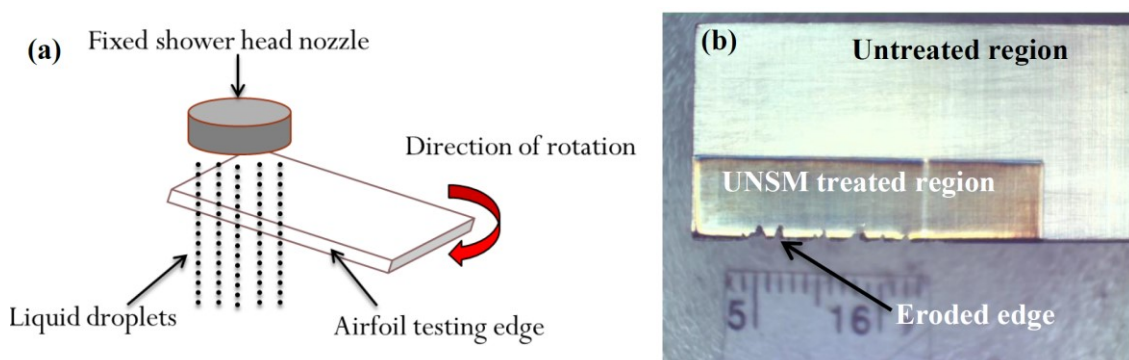
Figure 4-15: (a) schematic illustration of the WDE testing direction with respect to the airfoil treated surface and (b) typical eroded UNSM airfoil.

Figure 4-16 shows the WDE curves for the As-M and UNSM airfoil samples and Figure 4-17 shows the corresponding ER_{inst} curves tested at different impact speeds. Figure 4-16a

84

shows that at 350 m/s, both conditions had the same initial mass losses but after additional

number of cycles, the UNSM showed more mass loss as compared with the As-M condition.

This can be attributed to the severity of the test which induced high stresses. Due to the work

hardened surface, the material is most likely to fail in a brittle manner, allowing cracks to

propagate easily. Ma *et al.* [11] stated that strain-hardened surfaces decrease the erosion

resistance due to increase in brittleness. This could be the reason for the observed mass loss

in the UNSM. This observed trend is also shown in Figure 4-17a where the UNSM condition

showed higher maximum ER_{inst} than the As-M condition. Figure 4-16b shows that at 300 m/s,

both conditions showed initial mass losses but the UNSM condition further lost material with

additional cycles.
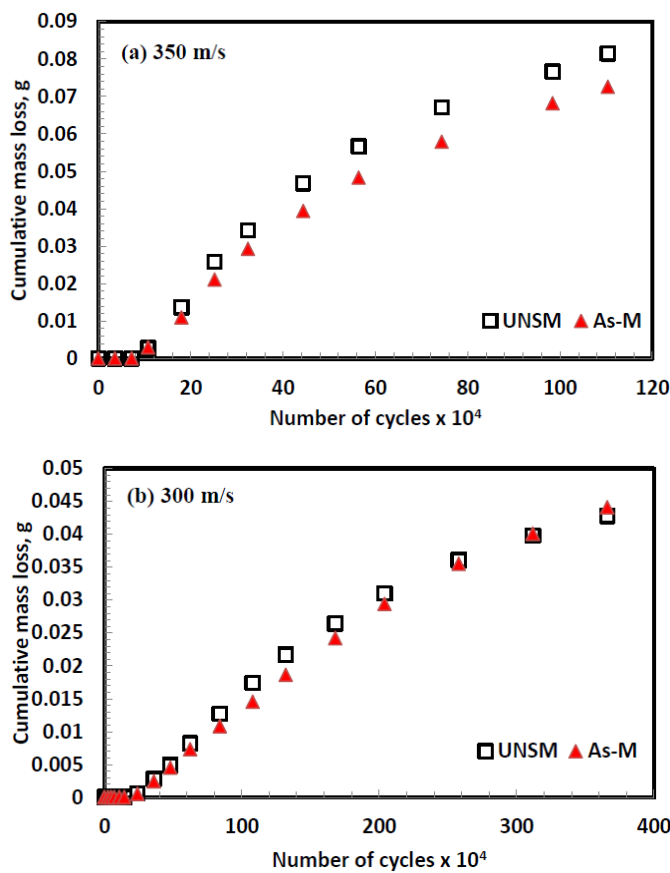
Figure 4-16: WDE curves of As-M and UNSM airfoil samples at different impact speeds.

Interestingly, the UNSM started showing better WDE performance than the As-M

condition. This is demonstrated clearly in the region A of Figure 4-17b where the UNSM

treatment mitigated further erosion damage. Similar tests were carried out using 300 m/s and similar trends were observed. Here, the induced compressive residual stresses might have arrested crack propagations similar to the crack arrest in stress corrosion cracking (SCC) tests [34]. Another reason for this behaviour could be attributed to the effectiveness of the UNSM treatment further away from the leading edge.
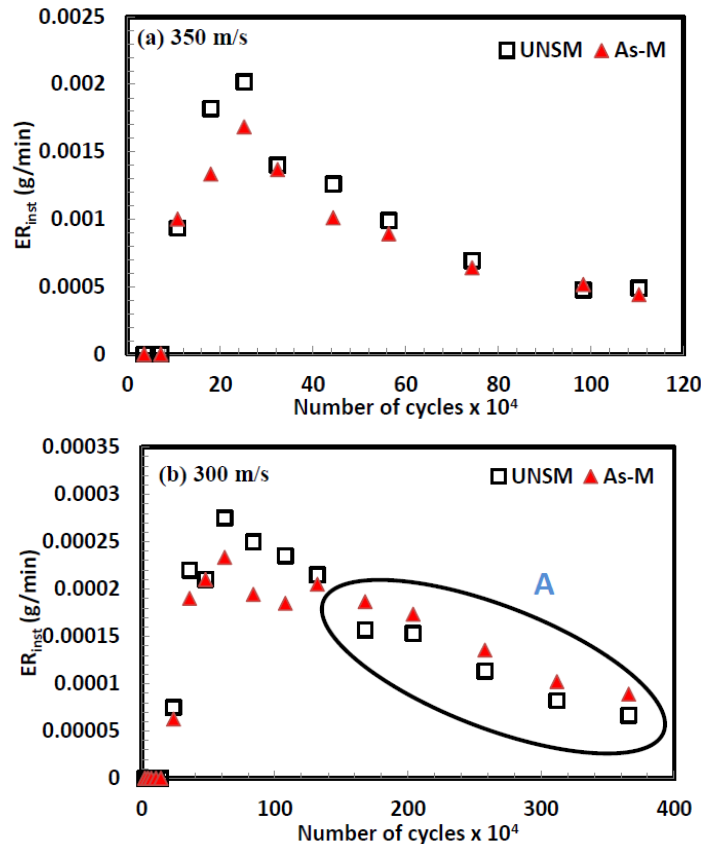
Figure 4-17: ER_{inst} for As-M and UNSM airfoil samples at different impact speeds.

4.3.2.3. Effect of sample geometry and UNSM on WDE performance

The effect of UNSM process on WDE performance of treated and untreated T-shaped and airfoil samples is reported in this work. UNSM process induced compressive residual stresses, modified the microstructure as well as improved the microhardness. For the T-shaped flat sample, the WDE test was conducted parallel to the ultrasonically modified surface. UNSM condition showed enhanced WDE performance especially at speeds of 250, 275 and 300 m/s compared with the As-M condition for this sample geometry. This is clearly demonstrated in Figures 4-12, 4-13 and 4-14. This behaviour is attributed to the modified

microstructure and enhanced microhardness. However, at 350 m/s both treated and untreated conditions had similar WDE performances. Even though UNSM induced compressive residual stresses which are beneficial in retarding crack initiation and propagation, this benefit could not be guaranteed for the T-shaped flat samples. This is because the modified microstructure and enhanced microhardness have more profound influence on erosion resistance than induced compressive residual stresses. Hence, it can be inferred that for the flat samples, the improved WDE performance is attributed to the hardening effect only. For the airfoils where the WDE test perpendicular to the treated surface (Figures 4-15a and b), the induced compressive residual stresses showed limited beneficial effect in mitigating erosion at the advanced erosion stage. This is the case at relatively low speed of 300 m/s. However, at 350 m/s where the test condition is severe, the induced compressive residual stresses showed no beneficial effect on the airfoil geometry. Contrary to the flat samples, the WDE performance of the treated airfoil condition at relatively low speed (300 m/s) could have been influenced by the induced compressive residual stresses. This is due to the fact that compressive residual stresses are through the thickness of the airfoil. It is worth noting that at 350 m/s, UNSM and its attributes were not realized on both sample geometries. This is due to the diminished effect of the UNSM treatment at high impact speed.

4.3.3. Optical macrographs

Optical macrographs were acquired after each interval during testing. Figure 4-18 shows the erosion process of As-M and UNSM conditions at 250, 275, 300 and 350 m/s corresponding to the WDE results presented in Figure 4-12. Normally, the erosion initiation process emerges with an erosion trace line due to impingement of droplets [11,17]. For instance, Figure 4-18a shows a trace line on the UNSM-treated condition after 20 minutes of exposure at 250 m/s. This indicates that the erosion is still in the incubation period where the mass loss is negligible [29]. Compared with the As-M condition after the same 20 minute

exposure in Figure 4-18a, the As-M condition showed formation of small isolated pits along the trace line, thus indicating early stage of the erosion damage even though the mass loss was negligible. With additional impacts, large isolated pits were formed and gradual pit growth was observed on the As-M condition. This is the situation seen in Figure 4-18a after 38 minutes of exposure where mass loss of 0.0003 g was recorded. At this point, the UNSM-treated condition only showed the erosion trace line without any noticeable pits. After 80 minutes of exposure, the As-M condition showed a mass loss of 0.0043 g with a complete crater formed. At the same time, the UNSM condition showed only a gradual growth of isolated pits with a mass loss of 0.0001 g. The delay in erosion process on the UNSM further delayed reaching the maximum ER_{inst} and final steady state. For instance, from Figure 4-14d, the As-M condition showed maximum ER_{inst} of 0.00014 g/min after 80 minutes and the UNSM showed maximum ER_{inst} of 0.00013 g/min after 160 minutes. Figure 4-18a also confirms the enhanced WDE performance (delayed erosion initiation) of UNSM as compared with the As-M condition. Reaching the maximum erosion rate, material damage was at its peak and complete crater has been formed. The material damage was due to the high exerted pressure and the liquid lateral jetting. This jetting also interacts with surface imperfections [16], forming surface cracks and surface asperities. This leads to significant material removal during the advanced erosion stages. It is important to note that with increased exposure time, both the depth and the width of the craters are increased [11]. For instance, crater width of less than 1 mm and greater than 1 mm were observed on the UNSM condition after 80 and 340 minutes, respectively, as can be seen in Figure 4-18a. This observation is also true when comparing the crater width/depth for different speeds at the same exposure. Similar erosion evolution and progression was observed at 275 m/s (Figure 4-18b) where UNSM showed delayed erosion initiation and smaller maximum ER_{inst} than that of the As-M condition. Similar analyses were made on Figures 4-18c (300 m/s) and d (350 m/s).
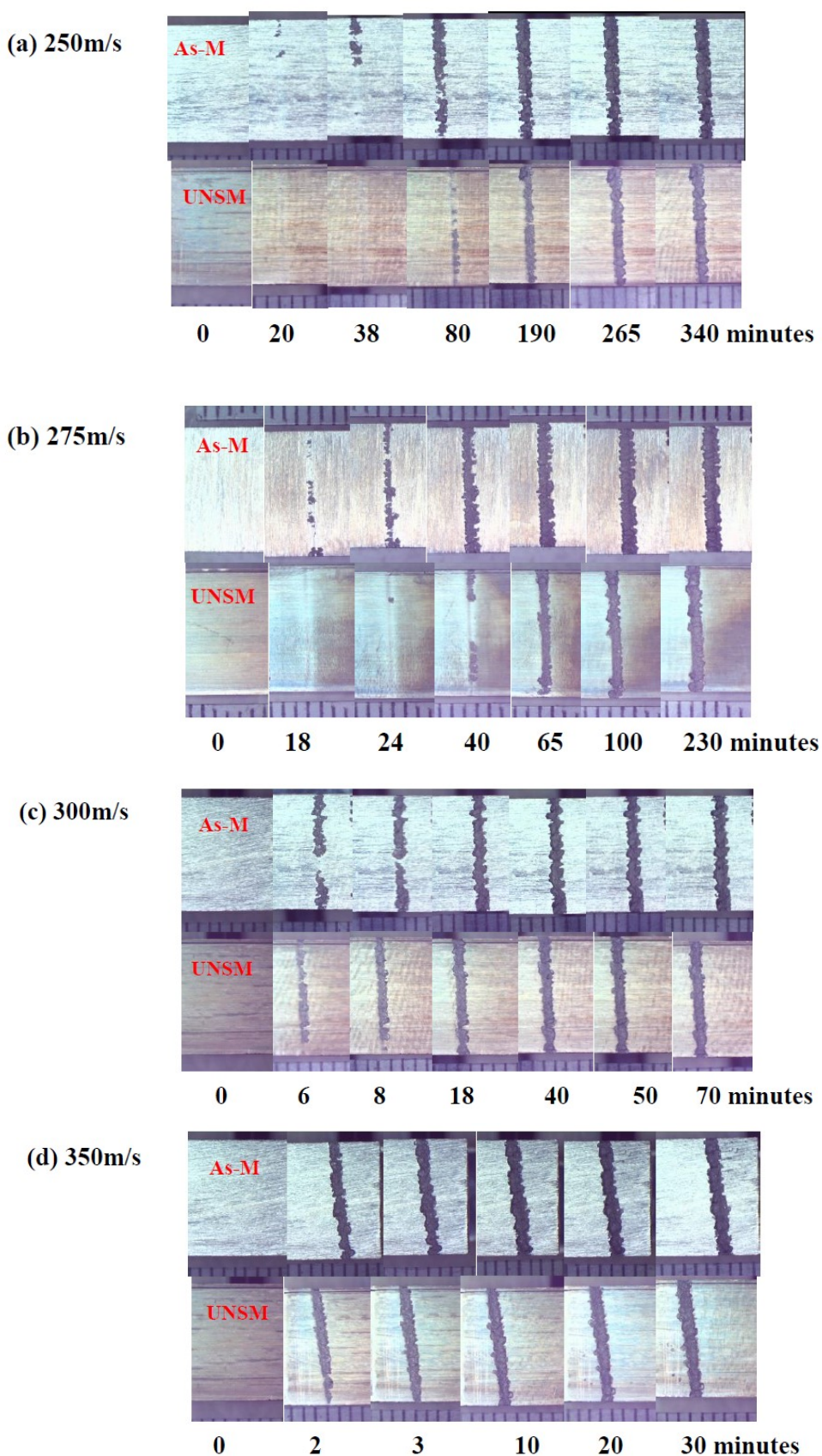
Figure 4-18: Optical macrographs showing the erosion evolution and progression of As-M and UNSM flat samples tested at various speeds and exposure times. The scale shown in each image is in mm.

Based on Figure 4-18a-d, it can be said that at impact speeds of 250 and 275 m/s, the UNSM condition showed delayed erosion initiation and the subsequent stages as compared with the As-M condition. At impact speeds of 300 and 350 m/s, the erosion initiation and progression of the As-M and the UNSM conditions are much faster as compared with these at speeds of 250 and 275 m/s.

In a similar fashion, the As-M and UNSM airfoil samples were observed under the optical microscope during test interruptions. However, for this sample geometry, the images were taken at two different orientations considering the fact that the WDE tests were conducted perpendicular to the UNSM treated surfaces. Figure 4-19 shows the erosion evolution and progression of the airfoil samples at 300 m/s. Both conditions showed similar erosion initiation as discussed previously and demonstrated in Figures 4-16b and 4-17b. It can be seen that after 90 minutes of exposure, individual craters are merging into one another due to the continuous impacts and liquid jetting. Also, the formed craters are becoming deeper as seen after 90 minutes. With further exposure, the craters further deepen and widen due to the accumulated liquid impacts and the radial outflows. The increase in depth with increase in exposure can be seen more clearly in this geometry than in the T-shaped flat samples. Similar to the flat samples, increasing the impact speed showed faster erosion initiation and greater maximum ER_{inst} (Figures 4-16a and 4-17a).
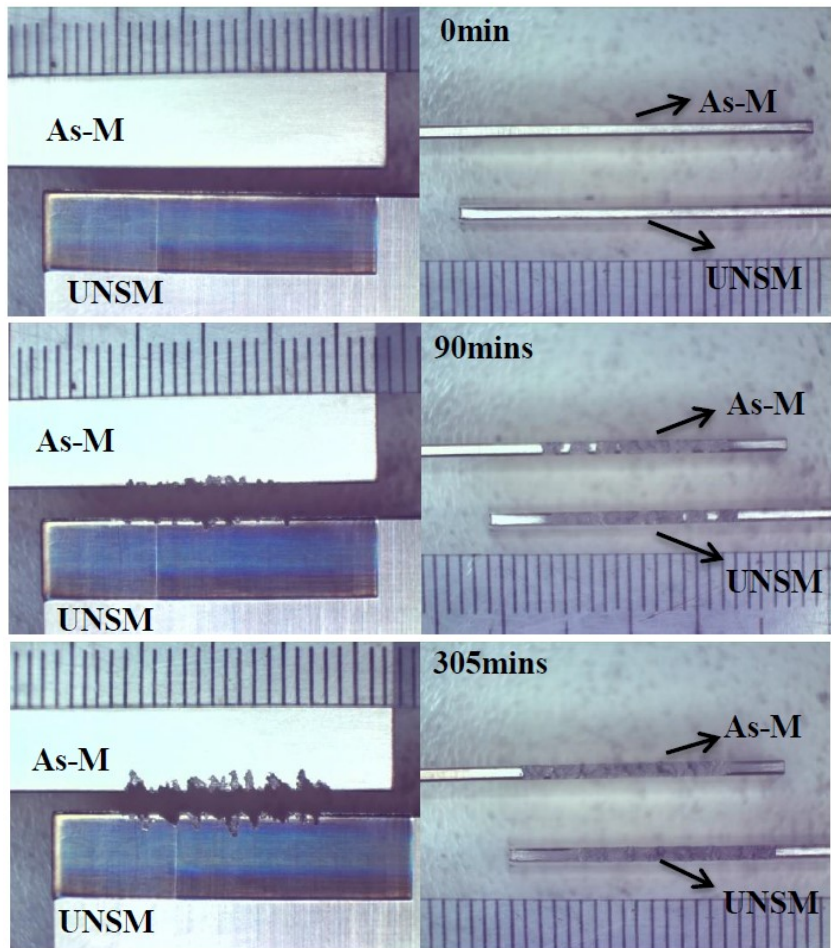
Figure 4-19: Optical macrographs showing the erosion evolution and progression of As-M and UNSM airfoil samples at 300 m/s. The scale on each image is in mm.

4.4. Conclusions

This work investigates the effect of UNSM treatment on the WDE performance of Ti-6Al-4V for the first time. The following conclusions can be drawn:

- UNSM treatment reveals surface features such as microdimples and microtracks due to the ball impact during processing. Also, the treatment induces compressive residual stress. In this work, compressive residual stresses were induced into the material down to 0.25 mm after UNSM processing.

- UNSM is associated with excessive plastic deformation, thus the process reveals mechanical deformation marks. This resulted in significant changes on the surface and sub-surface layers which leads to variation in grain size across the depth of the modified layer. Hence, material properties such as microhardness are enhanced.

91

- WDE results show that increasing the impact speed leads to faster erosion initiation and greater ER_{max}. This trend is attributed to the increasing impact pressure and the lateral jetting of the liquid droplet.

- UNSM T-shaped flat condition shows enhanced WDE performances especially at speeds of 250, 275 and 300 m/s compared with the As-M condition. This is attributed to the refined microstructure and increased microhardness. At speed of 350 m/s, the UNSM and As-M conditions show similar WDE performance.

- UNSM and As-M airfoils show similar WDE performance at 350 m/s, suggesting that the effectiveness of the UNSM treatment diminishes due to test severity. However, at 300 m/s, UNSM airfoil mildly enhances WDE performance at the advanced stage of erosion damage compared with the As-M condition.

- This work concludes that for the mechanical treatment to be effective in enhancing WDE performance, surface hardening and grain refinement must be realized. Compressive residual stresses alone are not sufficient to enhance WDE performance especially for the T-shaped flat geometry.

Acknowledgement

Chapter 5 : Water Droplet Erosion Performance of Laser Shock Peened Ti-6Al-4V

A. K. Gujba[a], L. Hackel[b], M. Medraj[a,c,*]

[a]Department of Mechanical and Industrial Engineering, Concordia University, 1455 De Maisonneuve Blvd. W. Montreal, Quebec, Canada, H3G 1M8.
[b]Metal Improvement Company-Curtiss Wright Corporation, 7655 Longard Rd, Livermore, California, United States CA 94551.
[c]Department of Mechanical and Materials Engineering, Masdar Institute, Masdar City, P.O. Box 54224, Abu Dhabi, United Arab Emirates.
*Author to whom correspondence should be addressed; E-Mail: mmedraj@encs.concordia.ca; Tel.: +1-514-848-2424 (ext. 3146); Fax: +1-514-848-3175.

ABSTRACT

The water droplet erosion (WDE) performance of laser shock peened (LSP) Ti-6Al-4V was investigated. LSP condition using 2 or 3 peening impacts per unit area induced compressive residual stresses. However, LSP treatment showed mild increase in microhardness and no observable changes in the microstructure. The effect of LSP and its associated attributes on the WDE performance was studied according to ASTM G73 standard. Influence of impact speed between 150 and 350 m/s on the WDE performance was explored. Two sample geometries, T-shaped flat and airfoil, are used for the WDE tests. For the flat samples, LSP showed little or no beneficial effect in enhancing the WDE performances at all tested speeds. The peened and unpeened flat samples showed similar erosion initiation and maximum erosion rate (ER_{max}). LSP airfoil samples showed mild improvement in the WDE performance at 300 m/s during the advanced erosion stage compared to the as-machined (As-M) condition. However, at 350 m/s, no improved WDE performance was observed for the LSP airfoil condition at all stages of the erosion. It was concluded that compressive residual stresses alone are not enough to mitigate WDE. Hence, the notion that fatigue mechanism is dominating in WDE damage is unlikely.

Keywords: LSP; microstructure; microhardness; residual stresses; WDE; impact speed; Ti-6Al-4V

5.1. Introduction

Gas turbine efficiency in power generation industry is affected by changes in temperature [1]. This is mostly experienced during summer times when ambient temperature increases. In order to increase the gas turbine efficiency, cost effective techniques are employed to keep the temperature at the inlet of the gas turbine compressor as low as possible. Among these techniques, fog cooling technique has been used successfully. In this technique, water droplets are sprayed into the gas turbine compressor to cool down the intake air, thus increasing the intake mass. This approach reduces the temperature and increases power output [5]. A major setback of this method is the erosion damage caused to the leading edge of the rotating blades during service. This is due to the combined effect of the rotating blades and the injected liquid droplets during fog cooling [6]. This damage further causes fatigue damage for the entire gas turbine. The erosion damage is known as "water droplet erosion (WDE)" which is the progressive loss of material from a solid surface due to continuous impacts by liquid droplets [7]. The high pressure exerted by the liquid droplets and the radial outflow (lateral jetting) of the droplets along the surface are the main driving forces of the erosion damage [10,131]. Despite the known causes of the erosion damage, the erosion process of materials is considered to be a complex phenomenon. This is due to the many parameters involved such as impact speed, impact angle, droplet size, and mechanical properties and conditions of the target material. To fully understand the erosion process, the effect of these parameters on the WDE behaviour must be understood. However, the task becomes more cumbersome especially when considering the interactions between these parameters such as impact speed and droplet size. Also, due to the variation of erosion rate with exposure time, predicting the erosion behaviour becomes difficult. Therefore, WDE experimental investigations are essential to understand the WDE behaviour of materials.

A typical material prone to this type of erosion damage is Ti-6Al-4V alloy, used for compressor blades in gas turbines. Surface coatings [24,33] and laser surface treatments [25,31] have been employed to mitigate WDE damage on Ti-6Al-4V. However, WDE is accelerated due to the presence of surface defects, interface defects and microcracks after such treatments. Recently, there is considerable interest in understanding the effectiveness of mechanical treatments in combating erosion damage. This is due to the deep levels of induced compressive residual stresses after mechanical processing. WDE behaviour of mechanical surface treatments such as deep rolling (DR) [11] and ultrasonic nanocrystalline surface modification (UNSM) [148] have recently being studied. This work explores another mechanical surface treatment, laser shock peening (LSP). LSP is a cold working process where pulses hit the surface through high power intensity, generating shock waves. As the shock wave stress exceeds the dynamic yield strength of the material, plastic deformation occurs [34]. These waves deform the top surface and compressive residual stresses are extended into the material [34]. More information on LSP in relation to shock wave generation, process parameters, residual stress profile, surface quality and material properties can be found in [34]. For the most part of the literature, LSP was usually employed to enhance the fatigue life [58,71,149,150] and fretting fatigue life [85] of materials such as Ti-6Al-4V. These enhancements have been attributed mainly to the significant depth of induced compressive residual stresses after LSP processing [151]. So far, the effect of LSP and its associated attributes on the WDE performance of Ti-6Al-4V or other alloys could not be found in the literature. Reports [9,117,133] have shown that WDE damage mechanisms is influenced significantly by crack initiation and propagation. Also, due to the continuous liquid impingements in a cyclic fashion, researchers [9,11,117] have associated WDE to fatigue. Moreover, it is well known that LSP retards crack initiation and propagation as well as enhances fatigue life [34]. At this point, one would expect LSP to mitigate the

WDE damage to a certain degree. For these reasons, studying WDE performance of laser peened Ti-6Al-4V is worthwhile. This work attempts to explore this research gap for the first time. The WDE performance is discussed based on the observed residual stresses, microhardness and microstructure. Much attention was given to the influence of impact speed on the WDE performance. Another factor that can influence WDE behavior is the sample geometry, however only flat sample geometry has been studied extensively in the literature [11,24,25,31,33]. Only recently, a study [148] by the current authors investigated the effect of sample geometry on the WDE behavior of Ti-6Al-4V. In the study [148], ultrasonic nanocrystalline surface modification was employed on two sample geometries, T-shaped flat and airfoil. The current study also explores similar sample geometries (T-shaped flat and airfoil), however different surface treatment (LSP) is employed. In this paper, the influence of sample geometry and the effectiveness of LSP and its attributes on the WDE performance of Ti-6Al-4V are addressed. To achieve this objective, a systematic approach is followed in carrying out this investigation.

5.2. Experimental procedure

5.2.1. Material and sample geometries

For this study, Ti-6Al-4V (ASTM B265, Grade 5) alloy [134], used for compressor blades in gas turbines, was investigated. Figure 5-1 shows the starting microstructure of the Ti-6Al-4V alloy which contains α- and β-phases. T-shaped and airfoil samples, as shown in Figure 5-2, were machined using a CNC Haas machine under flood coolant in accordance to the sample's geometrical requirement of the WDE testing rig. The T-shaped sample represents the typical flat surfaces commonly explored in the literature [11,24,25,31,33]. Moreover, in industrial gas turbine compressor blade where damage is caused by droplet impacts, the airfoil geometry represents the leading edge of the compressor blade. For this reason, the airfoil geometry is employed in this study.
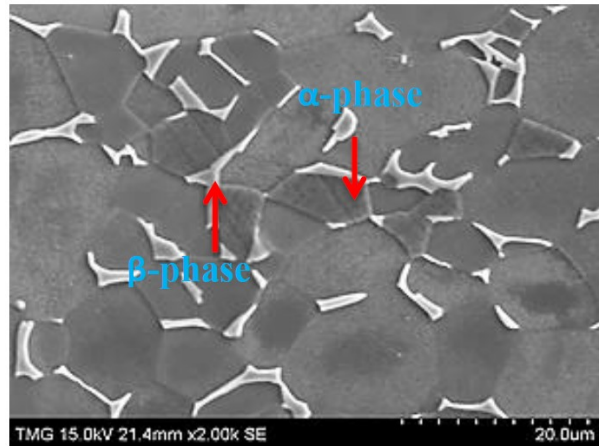
Figure 5-1: SEM micrographs showing the initial Ti-6Al-4V microstructure.
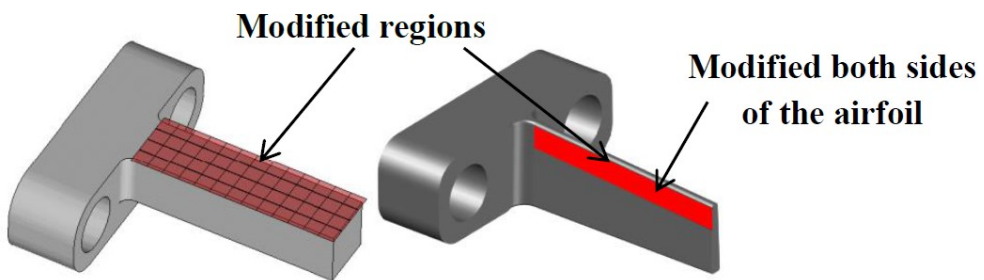
Figure 5-2: Typical T-shaped flat (left) and airfoil (right) samples machined.

5.2.2. LSP processing and characterizations

Untreated samples were used as the baseline reference material in this work. Otherwise stated, untreated condition in this work is also referred to as as-machined (As-M) condition. For LSP processing, next section describes the process. Also, to observe the effectiveness of the LSP processing, several techniques were used to characterize the untreated and treated samples.

5.2.2.1. LSP processing

For the LSP processing, an Nd:Glass laser at Metal Improvement Company (MIC), Livermore Laser Peening Division, California, USA, was used. Table 5-1 shows the LSP processing parameters used in this work. Figure 5-2 also shows the LSP modified regions on both sample geometries. For the airfoil geometry, it is a common practice to peen both sides

of the sample in order to avoid distortion as reported in [69,71,135,152–154]. This approach has been adopted in this work.

Table 5-1: LSP processing parameters and conditions

Sample geometry	T-shaped Flat	Airfoil
Surface treated	As-M	As-M
Laser type	Nd:Glass	Nd:Glass
Ablative layer	Aluminum	No layer
Intensity (GW/cm^2)	10	10
Pulse time (ns)	18	18
Number of layers	2	3
Spot geometry	Square	Square

5.2.2.2. X-ray diffraction pattern and residual stress measurement

X-ray diffraction (XRD) patterns for the untreated and LSP treated surfaces were acquired in order to observe any induced strains during LSP. It has been reported that X-ray diffraction peak broadening is associated with induced strains [155]. In this work, variations in the peak intensity and peak broadening are monitored for the first three peaks. Top surface compressive residual stresses before and after LSP processing were also measured using the XRD $\sin^2\phi$ technique at Proto Manufacturing Inc., USA. Crystallographic plane of {213} and Bragg's angle ($2\theta = 142°$) obtained by Cu Kα radiation were employed for this purpose. For the LSP condition, residual stresses were measured relative to the peening (scanning) directions i.e. parallel (0˚) and transverse (90˚). Figure 5-3 shows a peened sample and the 0˚ and 90˚ directions used for measurements are indicated. For comparison, the top surface residual stresses for the As-M condition were also measured using these two directions.
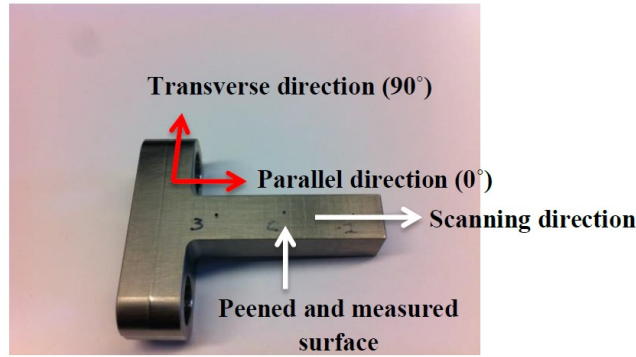
Figure 5-3: Illustration of 0° and 90° directions relative to laser scanning direction on a peened sample.

5.2.2.3. Microhardness

Prior to the hardness measurements, the samples (LSP and As-M) were cut perpendicular to the surface using a diamond cutter. Under cooling and lubricating fluid conditions, low speed and moderate load were applied in order to minimize undesired surface modifications during cutting. After mounting, SiC papers from 400-800 grits were used for grinding and vibratory polishing with 1 µm diamond paste was employed to remove scratches and other undesired debris. Microhardness measurements were carried out on the top surface and cross-section of LSP and As-M samples. A 50 gf load and 15 seconds dwell time were used during measurements. Microhardness at 7-8 locations were obtained across the depth of LSP and As-M samples. At each location, the average and standard deviation of 4-5 readings were calculated.

5.2.2.4. Microscopy

To observe any surface features, the as-treated top surface was observed under SEM (S-3400N, Hitachi). For surface and in-depth microstructure investigations, Kroll's reagent containing 2ml HF + 5ml HNO_3 + 100ml H_2O was used to etch the vibratory polished samples. As recommended by Gammon *et al.* [137], etching time of 15 seconds was chosen to have a balance between details and contrast. SEM images of the polished-etched top surface and cross-sections for both LSP and As-M samples were taken at different magnifications.

5.2.3. WDE testing and damage analysis

5.2.3.1. WDE tests

A rotating disc rig at Concordia University, shown in Figure 5-4a, was used for studying the WDE performances of LSP and As-M Ti-6Al-4V. The test was conducted in accordance with the ASTM G73 standard [29]. In this rig, the As-M and LSP samples are fixed at diametrically opposite ends of the rotating disc as shown in Figure 5-4a. To avoid vibrations during testing, difference in sample weight not exceeding 0.05 g was maintained. It is worth noting that prior to testing, the surface roughness of both LSP and As-M samples were similar. The nozzles are fixed and protected by a shield, as shown in Figure 5-4b, to prevent droplets from drifting away during testing. Two types of nozzles were employed for the WDE tests depending on the sample geometry. A shower head nozzle was used for testing the airfoil samples; whereas, a single streak nozzle was used for testing the T-shaped flat samples. Figures 5-5a and b show a schematic illustration of the WDE testing direction with respect to the T-shaped flat and airfoil treated surface, respectively. Typical WDE testing parameters are summarized in Table 5-2. Reaching the desired impact (rotational) speed, de-ionized water droplets were introduced at a controlled flow rate. The impact angle of 90º which causes the most severe water erosion damage [109] was used. The erosion exposure time depends on the impact speed, nozzle type, sample geometry and erosion stage. For instance, shorter exposure times were used in order to capture the early stages of the erosion process (initiation stage). Whereas, longer times were employed as the test progressed to the advanced stages of erosion.
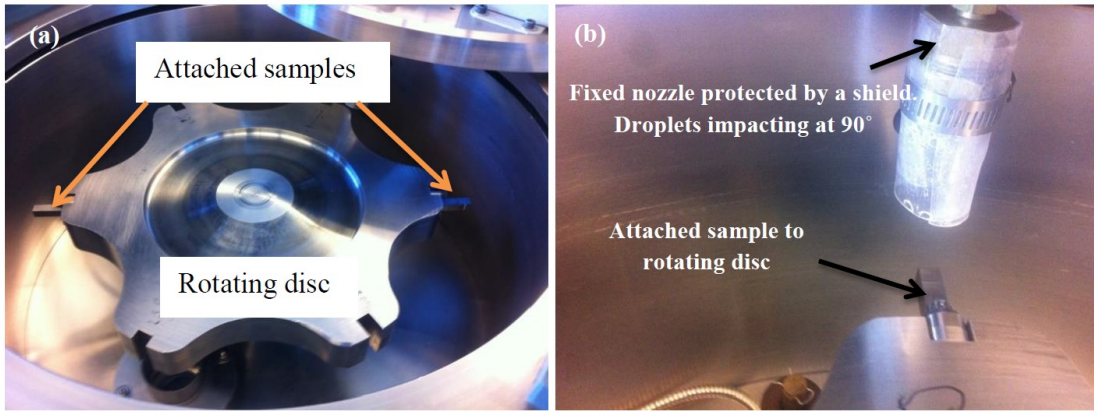
Figure 5-4: Water erosion rig with attached samples (a) and fixed nozzles and sample (b).
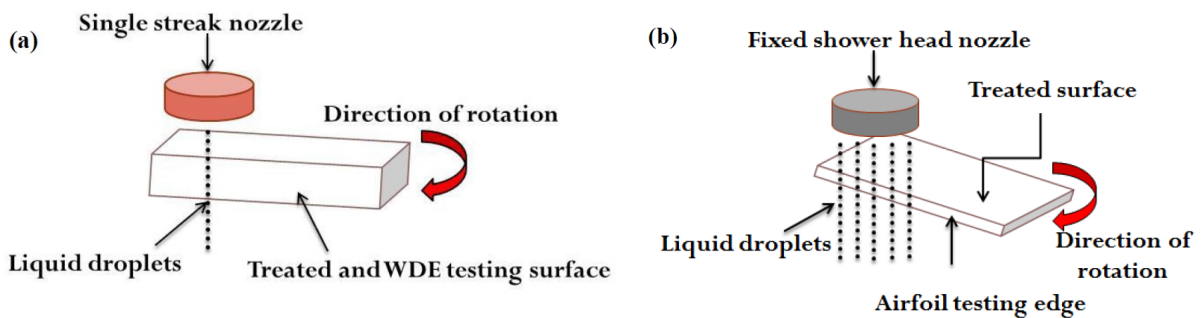
Figure 5-5: Schematic illustration of the WDE testing direction with respect to (a) T-shaped flat and (b) airfoil treated surfaces.

Table 5-2: WDE test parameters used in this work

WDE parameters	Flat sample	Airfoil sample
Impact speed (m/s)	150, 200, 250, 300, 325, 350	300, 350
Rotational speed x 10^3 (rpm)	6, 8, 10, 12, 13, 14	12, 14
Flow rate (liter/min)	0.05	0.15, 0.20*
Nozzle head type	Single streak	Shower head
Nozzle distance from sample (mm)	5	5
Average droplet size (µm)	463	460, 200
Impact angle (°)	90	90

*Flow rate of 0.20 L/min was used only for shower head nozzle producing average droplet size of 200 µm.

5.2.3.2. Damage analysis and WDE curves characterizations

During the WDE tests, experiments were halted at certain intervals and eroded samples were weighed using a balance having ±0.2 mg accuracy. Also, to understand how the erosion process evolved and progressed, images were taken using a standard stereo optical

microscope at the intervals during which mass loss was measured. Typical erosion curves such as cumulative mass loss *versus* number of impingements, maximum erosion rate (ER$_{max}$) *versus* impact speed and number of impingement to erosion initiation *versus* impact speed were plotted. The cumulative mass loss is the sum of material loss due to exposure to an erosive medium at a particular time. The number of impingement was determined using Equation 5-1.

$$N_{imp} = R \times E_t \times N_{droplets} \qquad (5-1)$$

Where N_{imp} is the cumulative number of impingements during an exposure period, R is the rotational speed (rpm), E_t is the erosion exposure time (minutes) and $N_{droplets}$ is the number of droplets impacting the sample per revolution. For the flat sample geometry, $N_{droplets}$ has been determined as 6. Detailed procedure on the droplet generation, droplet size distribution and number of droplets impacting the sample has been reported by the current authors in reference [133]. Contrary to the flat sample geometry, there is a challenge of quantifying the number of droplets impacting the airfoil sample. This is due to the shower head nozzle used during testing. Hence, graphs of cumulative mass loss *versus* number of cycles are plotted. The number of cycles is simply $R \times E_t$. For satisfactory determination of the incubation period and ER$_{max}$, a three line representation method [12] demonstrated in Figure 5-6a is used. In Figure 5-6a, the ER$_{max}$ denoted as "B" is the slope of the data points in maximum erosion stage, whereas the incubation period denoted as "A" is the intersection of the straight line with the x-axis (time axis) [29]. To determine the relationship between impact speed and ER$_{max}$, the power law relationship given in Equation 5-2 is used.

$$ER_{max} \propto V^n \qquad (5-2)$$

Where E_R is the erosion rate, V is the impact speed and n is the speed exponent. To observe the erosion rate as the erosion test progressed, the instantaneous erosion rate (ER$_{inst}$) which is the slope between two consecutive points on the erosion-time graphs is plotted,

similar to that shown in Figure 5-6b. Hence, in this study the incubation period, ER_{max} and ER_{inst} are analyzed.
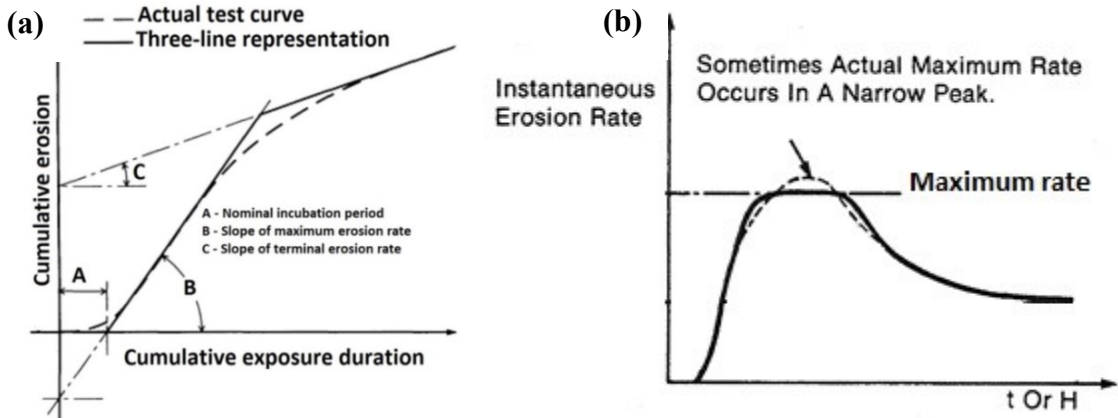
Figure 5-6: WDE curve analyses using (a) three line representation [12] and (b) ER_{inst} [29].

5.3. Results and discussion

5.3.1. Effect of LSP on surface and in-depth characteristics

The effects of LSP and its associated attributes on the surface and in-depth characteristics of Ti-6Al-4V alloy have been investigated. This section reports the effect of LSP process on the observed XRD pattern, compressive residual stress, microstructure and microhardness.

5.3.1.1. XRD pattern and compressive residual stresses

Figure 5-7 shows the XRD patterns of the As-M and LSP conditions acquired. Observing the first three peaks, the intensity of the first two peaks is reduced for the LSP condition compared to the As-M condition. For all three peaks, LSP condition showed peak broadening compared to the As-M condition. The full width half maximum (FWHM) approach was used to quantify this peak broadening in Figure 5-7. For the As-M condition, 0.26, 0.22 and 0.36 were obtained for first, second and third peak, respectively. Similarly, for the LSP condition, 0.38, 0.39 and 0.38 were obtained. It can be inferred here that the reduced peak intensity and peak broadening are due to the induced lattice strains during LSP processing [156,157]. Prevéy [158] and Zolotoyabko *et al.* [155] mentioned that X-ray diffraction peak broadening

is associated with increase in induced lattice strains. This was attributed to the induced cold work during processing. This is in accord with the observation in this work.

Furthermore, the top surface compressive stresses were measured for the As-M and LSP conditions in the 0, scanning, and 90˚, transverse, directions. The As-M condition showed -490±19 and -607±9 MPa, respectively in the 0º and 90º directions due to the machining process. LSP condition showed residual stresses of -770±13.5 and -768±14.82 MPa in the 0º and 90º directions, respectively, which are higher than those observed for the As-M condition. This is due to the effectiveness of LSP in inducing compressive residual stress. The LSP induced stresses are in the range of 90-110 ksi (600-750 MPa) and about 60-80% of the materials' yield strength. This is in accord with the current findings. Since, several studies reported the variation of the compressive residual stress with depth after the LSP process [58,71,85,150,159], the in-depth residual stresses were not measured in this work.
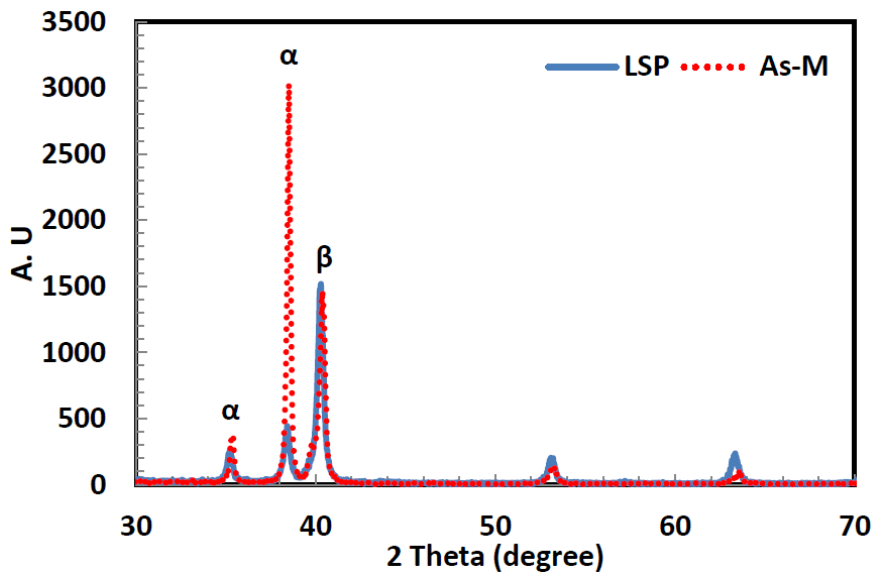
Figure 5-7: XRD patterns of the As-M and LSP treated surface.

5.3.1.2. Microstructure

The top surface and cross-sectional views of the As-M and LSP conditions were observed using SEM. Figure 5-8a shows the observed top surface after LSP processing, however microstructural changes due to deformation are not observed due to the small amount of cold

working induced during LSP process [34,86,87]. Graham *et al.* [160] further mentioned that laser shock processing does not cause macroscopic deformation in the treated region. Thus, this micrograph is similar to the starting microstructure (As-M) shown in Figure 5-1. Figures 5-8b and c show the in-depth microstructures of the As-M and LSP conditions, respectively. Similarly, no noticeable changes were observed in the microstructure after LSP treatment across the depth. Shepard *et al.* [154] reported the effect of LSP on the microstructure of Ti-6Al-4V. They [154] employed several peening parameters such as different pulse repetitions of 1, 3 ad 5 shocks/spot and power densities of 4 and 9 GW/cm^2 while keeping pulse duration of 20 ns constant. Their [154] results showed that LSP induced deep levels of compressive residual stresses especially with increase in both pulse repetition and power density. However, their [154] SEM micrographs showed no changes in the microstructure after peening. Zhao [161] also reported that the microstructure of peened and unpeened Ti-6Al-4V samples after LSP processing at different energy levels was similar. This is also the case in the present work. It is well known that the pulse duration produced by the peening process where laser shock interaction times are very short (in nanoseconds) compared to other conventional peening techniques such as shot peening [162]. Even though XRD analysis (peak broadening) suggests induced strains after LSP, the short interaction times might not be enough to significantly change the microstructure. This is mainly attributed to the low level of cold work during processing (about 5 %) [87]. Moreover, information on the interaction of the microstructure with laser induced shock waves and the resulting changes at the macro- and microstructural levels is still lacking in the literature. Based on the present work and works in [154,161], it can be inferred that microstructural changes after peening might not be significant even though deep compressive residual stresses are induced..
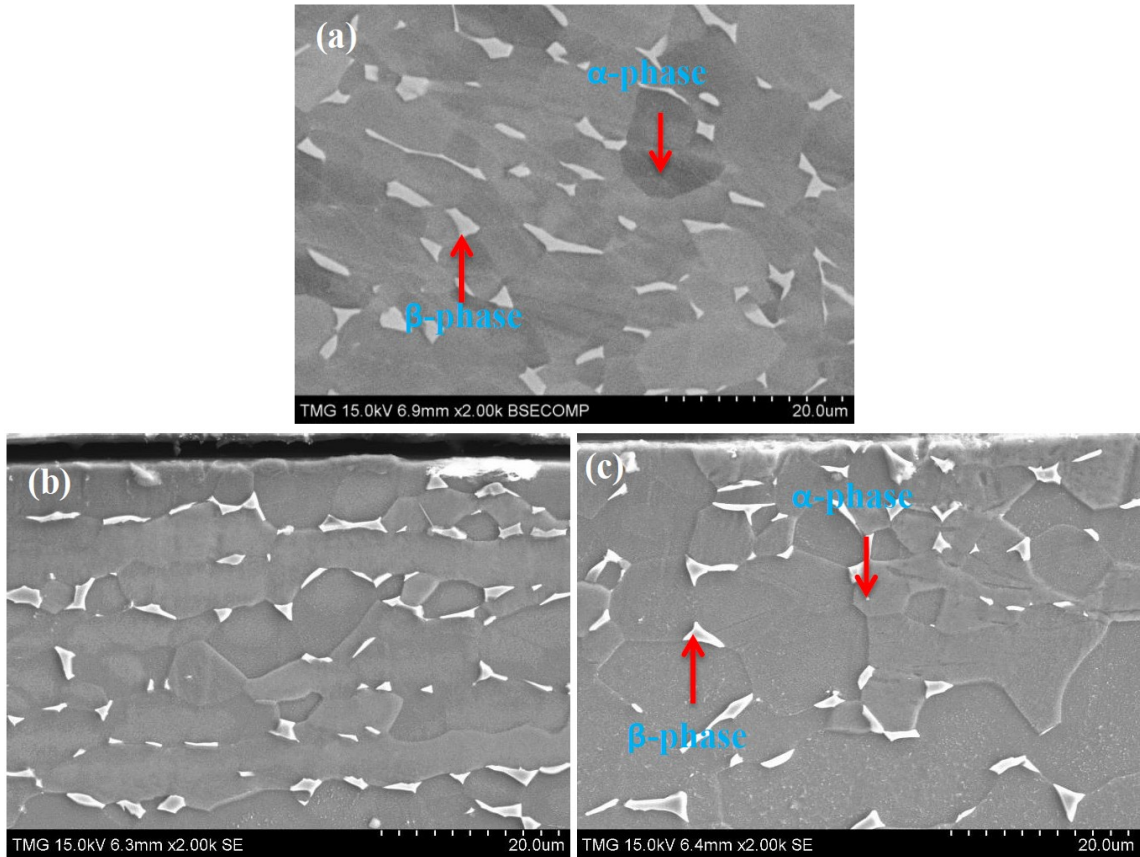
Figure 5-8: SEM micrographs showing (a) treated top surface (b) untreated cross-section and (c) LSP treated cross-section.

5.3.1.3. Microhardness

Figure 5-9 shows the microhardness measurements of As-M and LSP conditions. The top surface microhardness values were 331±5.3 HV and 333±6.2 HV for As-M and LSP conditions, respectively. Microhardness across the depth shows that only a mild increase or no appreciable increase after the LSP treatment. Chavez *et al.* [163] also reported that LSP had no apparent effect on the microhardness of Ti-6Al-4V. These observations are in accord with the works of Rubio-González *et al.* [41] and Fairand and Clauer [40] on other materials. For instance, Rubio-González *et al.* [41] showed that LSP had no effect on the hardness of 2205 duplex stainless steel. They [41] attributed this to the insufficient energy from LSP. Again, Fairand and Clauer [40] reported the effect of LSP on heat treated aluminum alloys (2024-T351, 2024-T851, 7075-T651, 7075-T73). Their [40] results showed that LSP increased the hardness in 2024-T351. However, no appreciable effect on the hardness of peak

aged 2024-T851 and 7075-T651 and over-aged 7075-T73. No obvious reasons were mentioned for the observed behaviours. This can be attributed to the low level of cold working associated with the LSP processing [164]. Reports [87,88] have shown that LSP induces about 5 % cold working. It is known that cold working improves the mechanical properties such as hardness and tensile strength [165]. For instance, Nagarjuna *et al.* [166] studied the effect of cold working on mechanical properties and structure of Ti alloy (Ti with Cu-1.5 wt%). They [166] reported that increase in percentage cold work from 0, 20, 40, 60 up to 80 % showed significant increase in hardness. This also had a corresponding increase in the tensile strength of the alloy. This is due to the fact that tensile strength is directly proportional to the hardness [167]. It was deduced from their work [166] that at 5 % cold work, the tensile strength was increased by only less than 2 % compared to 46.15 % increase at 80 % cold work. Petunina and Poplavskaya [165] also studied the effect of cold working on the strength of titanium-based alloys (pure Ti and Ti-3Al-2V). They [165] stated that the tensile strength of the titanium alloys was enhanced significantly after 20 % cold working with only a slight loss in ductility. Gupta *et al.* [168] also studied the effect of prior cold working before tensile tests on equiaxed α- and β-phase Ti-6Al-4V. Three different levels of cold working were employed, 0, 10 and 15 %. They [168] reported that with 10 % and 15 % cold work, the tensile strength (TS) and ultimate tensile strength (UTS) were increased as compared to 0 % cold worked condition. Hence, the strain hardening exponent (n) and strength coefficient (K) were consequently increased with increase in cold working. They [168] attributed this behaviour to the large amount of dislocations and the dislocation pile up hindered the movement of other dislocation, thus strain hardening the material. In the current work where LSP is assumed to induce only 5 % cold work, the hardness increased by only 2-3 %. From the aforementioned works [165,166], it can be confirmed that low level of cold working from LSP might not have significant effect on hardness. This accompanied with the

unchanged microstructure (Figure 5-8c) could have led to the observed unchanged microhardness. It is known that refinement of microstructure or reduction in grain size is associated with enhanced microhardness [148]. This is not the case in this work. The observed surface and in-depth characteristics are used to understand the WDE performance.
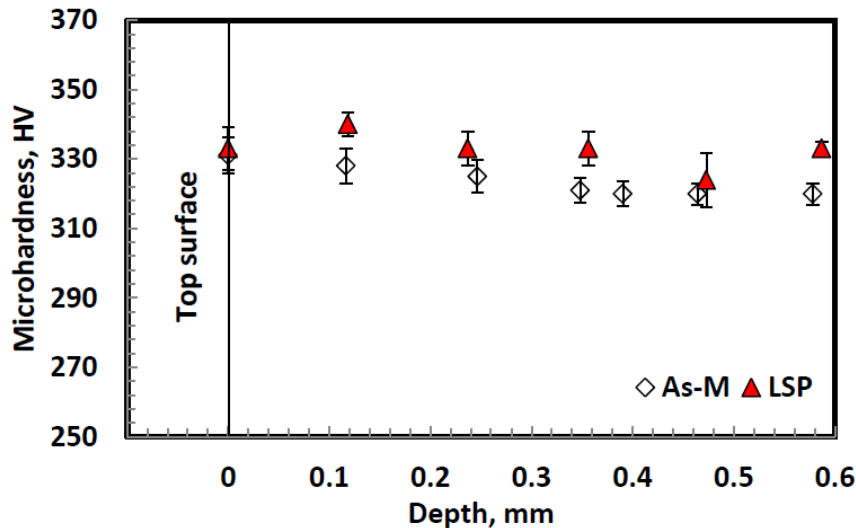
Figure 5-9: Measured microhardness with respect to depth for LSP and As-M conditions.

5.3.2. Water droplet erosion performance

During WDE tests, two coupons (As-M *versus* LSP) were tested at the same time in order to investigate their WDE performances. To understand the effects of LSP and its attributes on WDE performance, a wide range of impact speed was used. For the T-shaped flat samples, impact speed was the main parameter varied while keeping other parameters constant. Here, impact speeds of 150, 200, 250, 300, 325 and 350 m/s were selected. For the airfoil samples, only impact speeds of 300 and 350 m/s were used. Also, two droplet sizes of 200 and 460 μm were used. For the 460 μm droplet size used, impact speeds of 300 and 350 m/s were employed, whereas only 350 m/s was employed for the 200 μm droplet size test. Impact speed of 350 m/s was chosen as the most severe condition, whereas 300 m/s was chosen to have a less severe testing condition. Testing at lower impact speed than 300 m/s and 200 μm droplets would require impractical long testing time. Therefore, tests using impact speed of <300 m/s for airfoil geometry were not performed in this work.

5.3.2.1. WDE performance of LSP and As-M T-shaped sample conditions

Figures 5-10a and b show the graphs of cumulative mass loss *versus* number of impingements for flat T-shaped LSP and As-M conditions at impact speeds ranging from 150 to 350 m/s. Figure 5-10b shows typical well-behaved erosion curves with an S-shape. With this curve shape, distinct erosion stages such as incubation (initiation) period with negligible mass loss; acceleration stage up to a ER_{max} stage; deceleration (attenuation) stage with declining ER and terminal erosion state with constant ER can be observed [12,29,30]. In this work, the incubation period and ER_{max} are analyzed. From Figure 5-10, it can be seen generally that increasing the impact speed from 150 to 350 m/s showed faster erosion evolutions and progressions in both As-M and LSP conditions. This is due to the increase in test severity with increase in impact speed. Interestingly, at impact speed of 150 m/s (Figure 5-10a), no erosion was observed on both As-M and LSP conditions after 840 minutes of exposure which corresponds to approximately 30 million impingements. Here, only a shiny erosion line trace was observed under the optical macrograph and no visible damage was detected. This is as shown in the insert macrograph in Figure 5-10a. This could be the threshold speed for both As-M and LSP conditions which is greater than or equal to 150 m/s. The threshold speed is the speed below which no apparent damage is seen [30]. Moreover, the definition of this speed is somehow subjective and depends on the testing conditions such as impact speed, droplet size and number of impingements. In this work, it was found that using average droplet size of 464 μm and flow rate of 0.05 liter/min, the threshold velocity was in the range of 150 m/s $\leq V_{threshold}$ <200 m/s where there was no measurable mass loss after as long as 840 minutes of exposure which corresponds to more than 30 million impingements. This is an important observation has not been captured in previous studies on WDE of Ti-6Al-4V [9,17,31]. Based on Figures 5-10a and b, it can be seen that similar WDE performance was observed for both As-M and LSP conditions. In other words, both

conditions showed similar WDE behaviour at all stages of the erosion irrespective of the impact speed employed. The little difference observed in the graphs is considered within the experimental errors.
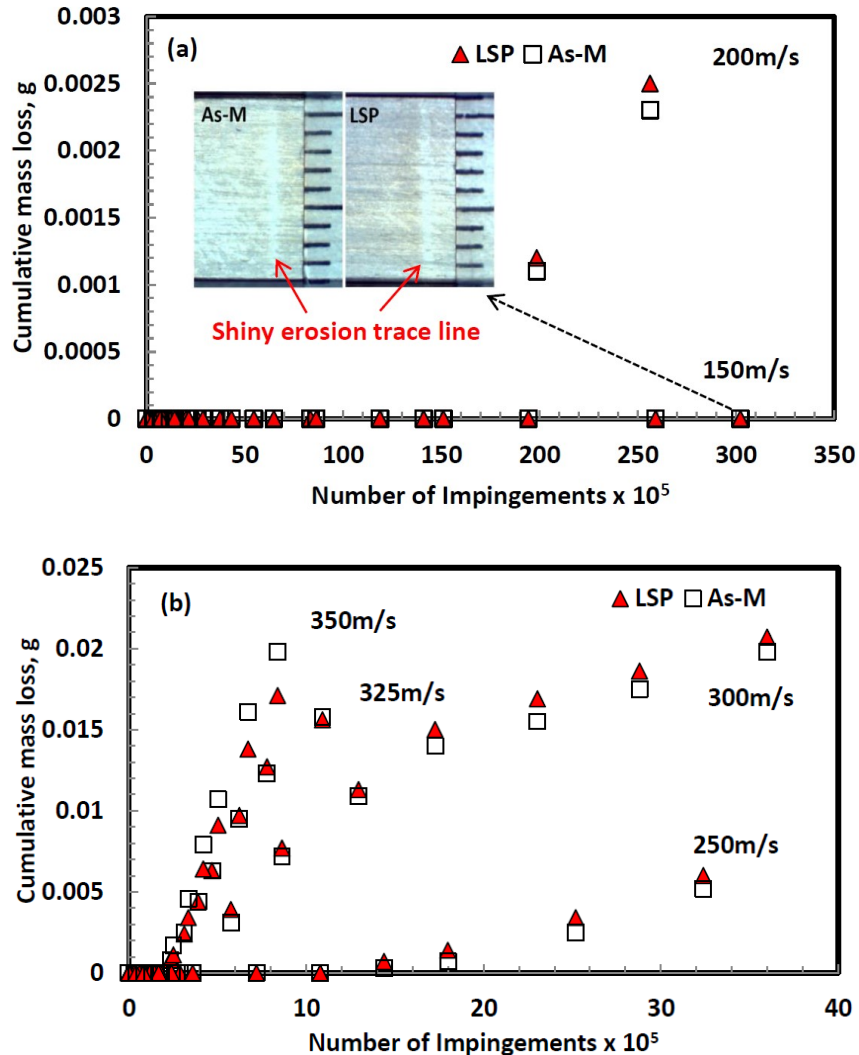
Figure 5-10: WDE curves for As-M *versus* LSP at (a) 150-200 m/s and (b) 250-350 m/s.

Using the three line representation (Figure 5-6a), the effect of impact speed on the erosion initiation and ER_{max} was deduced for the LSP and As-M conditions based on the results presented in Figures 5-10a and b. Figures 5-11a and b show the aforementioned effect of speed on the erosion initiation and ER_{max}, respectively. It is evident from Figure 5-11a that at higher impact speeds lower number of impingements were required to initiate erosion damage. Also, at higher impact speed corresponds to greater ER_{max} due to increased test

severity. However, at all tested speeds, number of impingements to initiate erosion for the LSP and As-M samples was the same. The relationship between impact speed and ER_{max}, was established using the power law equation (Equation 5-2) and the speed exponent was determined. For metals, typical exponent values range from 5-7 in the literature [110,111]. However, based on Figure 5-11b, exponent value of 8.9 was observed for the As-M and LSP samples, respectively. This observation is in accord with the studies by Kamkar [9] and Mahdipoor *et al.* [28] where they reported values of 9 and 7-9, respectively, for WDE tested Ti-6Al-4V. The exponent value obtained in this work and in [9,28] is higher than the range (5-7) found in the literature. This could be due to the test set-up/conditions, initial target surface conditions and erosive medium characteristics such as droplet size and droplet velocity. For instance, exponent values of 5 [110] and 6-7 [117] have been reported for liquid jet impact and liquid impingement erosion for pipe wall thinning applications, respectively. In this work and in [9,28], the application is for water droplet erosion for compressor blades of gas turbine. Hence, it can be seen that the test set-up/conditions are different which resulted in different exponent values. Also, the technique used for determining ER_{max} could have influenced the observed difference. In this work and in [9,28], three line representation technique was employed, whereas others [110,117,118] used the ER_{inst} approach. Based on Figure 5-11b, the exponent value (8.9) further confirms that the LSP and As-M conditions have similar WDE performance.

Two main reasons for the observed WDE performance are the lack of noticeable microstructural changes (Figure 5-8) and mild increase in microhardness (Figure 5-9) after the LSP treatment. Microhardness is one of the most important material properties used to assess the resistance of materials to WDE damage [18,30]. It has been reported [18,109] that erosion resistance varies with 2nd to 3rd power of hardness. Refined microstructure and reduction in grain size have also been associated with erosion resistance [18,30]. For treated

Ti-6Al-4V, enhanced microhardness and refined grains have shown improved erosion resistance [26,147]. However, this is not the case for the LSP condition, thus similar erosion behaviour compared to As-M condition is expected.
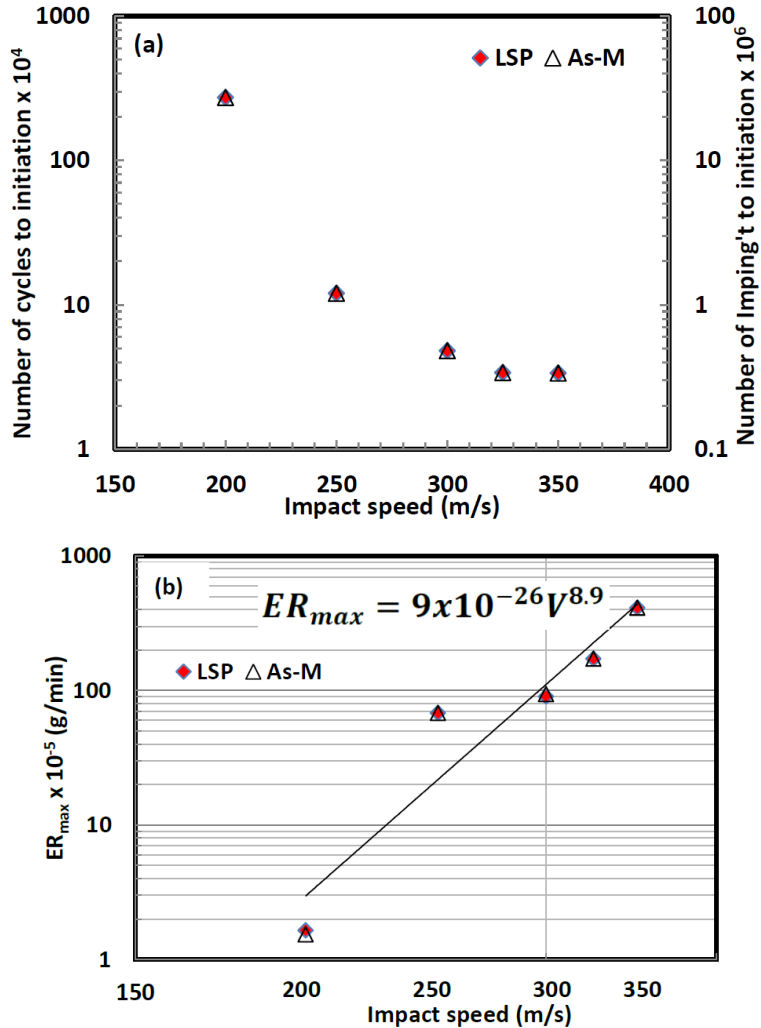
Figure 5-11: Effect of impact speed on (a) erosion initiation and (b) ER_{max}.

The influence of induced compressive residual stresses in understanding erosion performance is paramount. It has been reported that induced compressive residual stresses supress cavitation erosion. For instance, Hackel *et al.* [159] reported the effect of laser peening on the cavitation erosion behaviour of Ti-6Al-4V. Their [159] preliminary erosion results showed that LSP technique supresses cavitation erosion due to the beneficial induced compressive residual stresses. In their [159] work, no information about microhardness, microstructure and surface roughness after LSP was provided. Also, the starting surface

112

conditions for both peened and unpeened samples prior to the cavitation test were not mentioned. These details are needed in order to understand this behaviour. It should be noted here that cavitation erosion is different from water droplet erosion. The main difference is the high exerted pressure by the liquid droplets and the radial outflows in WDE damage and this is not the case during cavitation tests which deal with the collapse of bubbles. In WDE, the surface is continuously impacted by water droplets, transmission and reflection of the stress waves will occur repeatedly. These waves interact and result in high tensile stress waves that cause crack initiation and propagation of existing cracks. Because of the high frequency of the liquid impacts at high speeds, the stress wave interactions will be very fast and the magnitude of the resulting tensile stress waves will be high. This is not the case in cavitation tests.

The influence of mechanical surface treatments on the WDE behaviour of materials has not been explored extensively in the literature. Heymann [18] stated that processes involving cold working (strain hardening) such as pressing, rolling or hammering might be beneficial in mitigating erosion damage. However, too much cold working might show detrimental effects. In another report, Frederick and Heymann [10] stated that processes involving peening might not be beneficial in enhancing the WDE behaviour of materials especially during the incubation stage. This is due to the fact that the exposed surface is plastically deformed twice and consequently, work hardened twice. First work hardening comes from the peening process itself, whereas the second comes from the continuous droplet impacts during the erosion process. The duplication of the work hardening process at the incubation period might be detrimental to the WDE behaviour [10]. Heymann [30] further stated that the first plastic deformation retards erosion initiation while the second promotes the erosion initiation. The first and second plastic deformations balance each other, thus this may result in non-enhanced WDE performance. The statements mentioned in [10,18,30] are contradictory and

113

need to be supported with further investigations. In addition to this work, two mechanical surface treatments, deep rolling and (DR) and ultrasonic nanocrystalline surface modification (UNSM), have recently been explored in relation to WDE performance of Ti-6Al-4V. For instance, Ma *et al.* [11] studied the water impingement erosion performance of deep rolled *versus* As-M Ti-6Al-4V. During their [11] work, several DR parameters were explored in order to have deep compressive residual stress while improving the surface and sub-surface properties. Using similar sample geometry (T-shaped flat), WDE parameters such as droplet sizes (464 μm and 603 μm) and impact speeds (250 m/s and 350 m/s) were employed. Their [11] WDE results showed that no improved WDE performance for the DR condition compared to the As-M condition at all tested conditions. This is in accord to with the present work, where no enhanced WDE performance was observed for the LSP condition. More so, the present work and [11] revealed that no deterioration in the WDE performance was observed after LSP and DR processing, respectively. Gujba *et al.* [148] studied the effect of UNSM on the WDE performance of Ti-6Al-4V. T-shaped flat geometry was also tested while using impact speeds of 250, 275, 300 and 350 m/s and 464 μm droplet size. Their [148] WDE results showed that UNSM condition had enhanced WDE performance at impact speeds of 250, 275 and 300 m/s compared with the As-M condition. At 350 m/s, the effectiveness of the UNSM process diminished. The enhanced performance was attributed to the increased microhardness and modified microstructure after UNSM processing. In this work, even at lower speeds of 150 and 200 m/s employed, no enhanced WDE performance could be observed. This is due to the fact that LSP had no significant effect on the microhardness and microstructure (grain refinement). Even though, the amount of cold working is small in LSP, the observations in this work and [11] are in agreement with the explanations given in [10,30], who pointed out that a non-enhanced WDE performance maybe observed due to duplication of the working hardening process. However, the current work and [11] are in

disagreement with statements given in [18], who claimed that processes involving cold working might mitigate erosion damage. Interestingly, the work in [148] showed that specific process involving cold working mitigates erosion damage at certain conditions which is in accord with the explanations given in [18]. Also, the same work in [148] proved that duplication of the working hardening process did not show any non-enhanced WDE performance which is in disagreements with the explanation given in [10,30].

5.3.2.2. WDE performance of LSP and As-M airfoil sample conditions

Similar to the WDE studies on the flat T-shaped samples, airfoils in As-M and LSP conditions were investigated. However, the WDE tests were conducted perpendicular to the LSP treated surface as shown in Figure 5-5b. Figures 5-12a and b show the WDE curves for the As-M and LSP airfoil samples tested using 460 and 200 μm droplet sizes, respectively. Figure 5-12a shows the test carried out using 460 μm at 350 and 300 m/s and it can be seen that at 350 m/s, significant mass loss at all stages of the erosion was observed as compared with test at 300 m/s. This observation is also shown in the ER_{inst} curves in Figures 5-13a and b, respectively. Again, at 350 m/s (Figures 5-12a and 5-13a), the WDE performance of As-M and LSP conditions were very close. However, at 300 m/s (Figure 5-12a and 5-13b), LSP condition lost more material during early stages of the damage as compared to the As-M condition. At the advanced stages (>100 x 10^4 cycles), LSP condition showed slightly reduced erosion rate compared to the As-M condition. This could be due to the influence of induced compressive residual stresses which is through the thickness of the airfoil. This is an interesting observation that has been reported in another work by Gujba *et al.* [148]. They [148] studied the influence of UNSM treatment on the WDE performance of treated and untreated airfoil Ti-6Al-4V. Similar to the LSP treatment on the airfoil geometry, the UNSM treatment was carried out on both sides, thus residual stresses are across the thickness as well. Using similar erosion conditions i.e. 460 μm at 350 and 300 m/s, they [148] reported that at

350 m/s, no enhanced performance was observed. However, at 300 m/s the UNSM airfoil showed mildly enhanced WDE performance at the advanced WDE stages. This is the case in the present work (shown in Figure 5-13b) under the same eroding condition. Hence, the induced stresses might have resisted further crack propagations similar to the crack arrest in stress corrosion cracking (SCC) tests [34]. Based on the present work and [148], it can be said that both LSP and UNSM might be effective treatments especially when sample are treated away from the leading edge. It should be noted that this behaviour was observed only at 300 m/s which is relatively low speed testing condition.
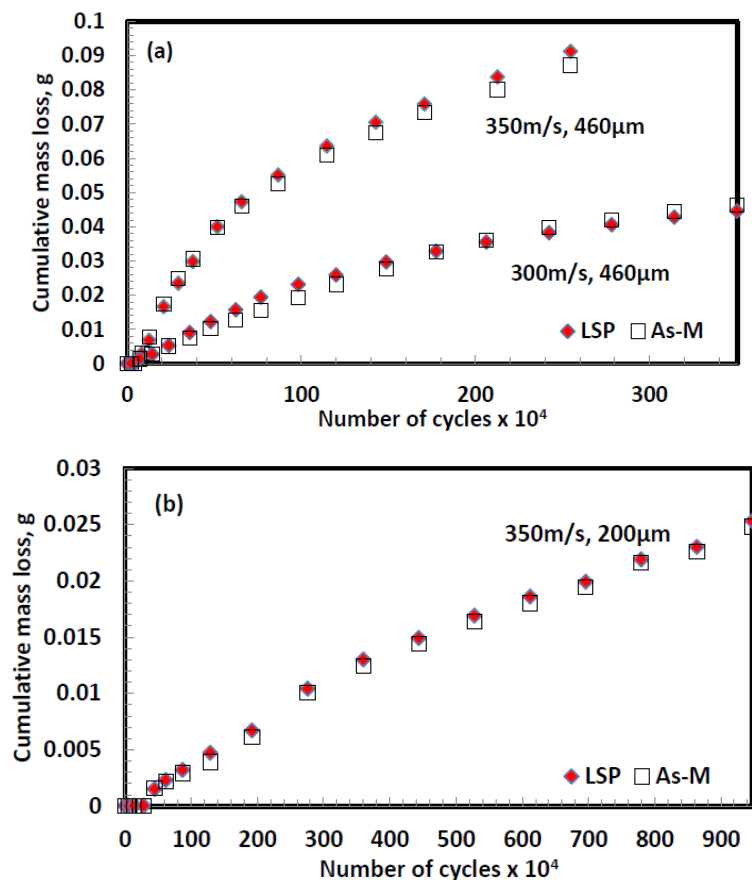
Figure 5-12: WDE curve of As-M *versus* LSP for (a) 460 and (b) 200 μm droplet sizes.

In order to further reduce the test severity, the droplet size was reduced to 200 μm while using 350 m/s. Figure 5-12b shows the WDE curve for test at 350 m/s and 200 μm. It can be seen that reducing the droplet size reduced the mass loss compared to test at 350 m/s using 460 μm (Figure 5-12a). This is attributed to the decreased test severity when using smaller

droplet sizes. Figure 5-12c shows the corresponding ER_{inst} for Figure 5-12b where the erosion rate was reduced significantly. However, the LSP condition did not show enhanced WDE performance at all stages of the erosion. By reducing the droplet size (reducing test severity), one would expect behaviour similar to Figure 5-13b. This is not the case in Figure 5-13c where the WDE performance for both As-M and LSP condition was the same.
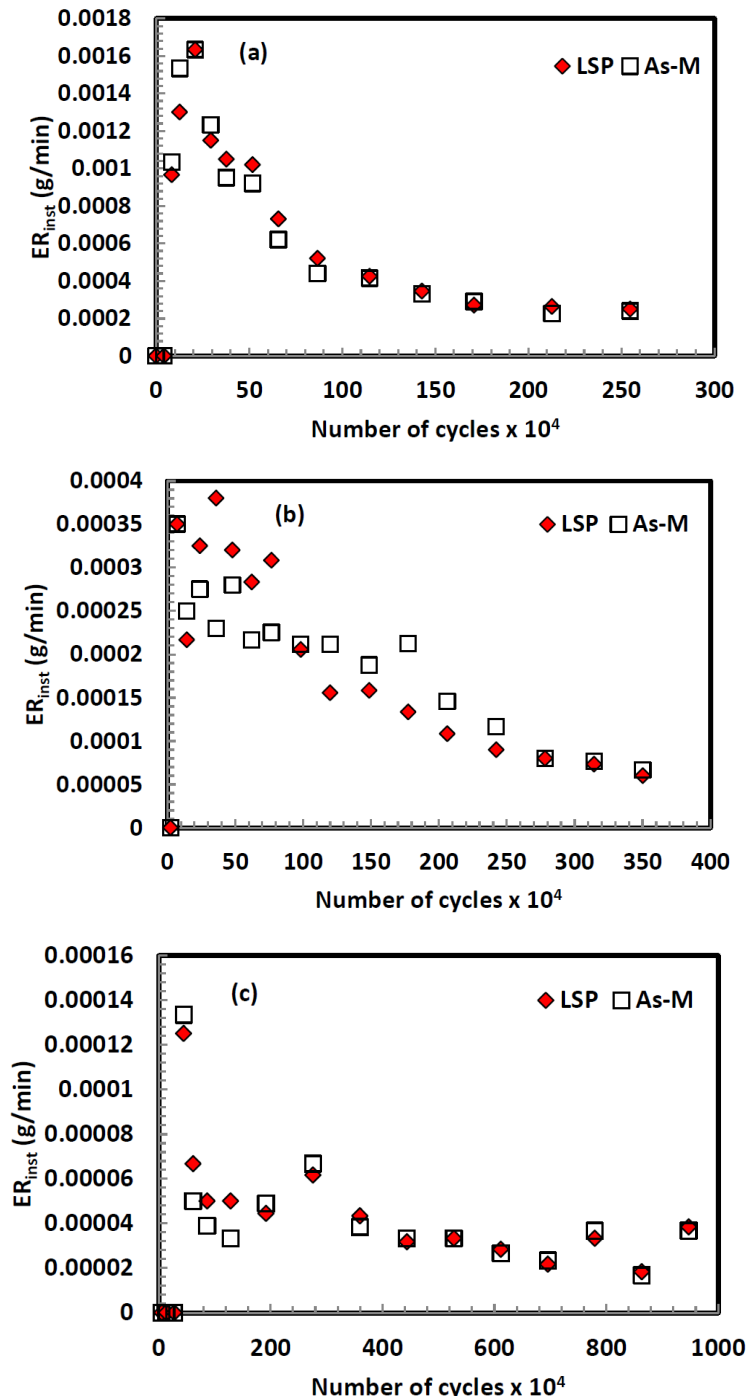
Figure 5-13: ER_{inst} for WDE tests using (a) 350 m/s, 460 μm, (b) 300 m/s, 460 μm and (c) 350 m/s, 200 μm.

5.3.2.3. Effect of sample geometry and LSP on WDE performance

The effect of LSP process on WDE performance of treated and untreated T-shaped and airfoil samples is reported in this study. LSP induced compressive residual stresses but had no significant effect on the microstructure and microhardness.

For the T-shaped flat sample, the WDE test was conducted parallel to the peened surface (Figure 5-5a). Laser peening had no beneficial effect in enhancing WDE performance for this sample geometry. This is clearly demonstrated in Figure 5-10 where both As-M and LSP conditions showed similar WDE performance. In other words, both conditions showed similar erosion initiation and ER_{max} at all tested speeds as shown in Figures 5-11a and b. This was attributed to the unchanged microstructure and lack of appreciable increase in microhardness. Even though LSP induced compressive residual stresses which are beneficial in retarding crack initiation and propagation, this benefit could not be realized for the T-shaped flat samples. This explanation is in accord with the findings in [148]. In their [148] WDE study, they mentioned that the benefit of compressive residual stresses could not be guaranteed for the T- shaped sample. This is because modified microstructure and enhanced microhardness seem to be the dominating factors in erosion resistance than the induced compressive residual stresses. Comparing [148] with this work, the argument can further be strengthened that compressive residual stresses are not beneficial for this T-shaped flat sample geometry. This is due to the fact that LSP only induced compressive residual stresses with minimum influence on the microstructure and microhardness. Based on this study and [148], it can be inferred that for enhanced WDE performance on the flat samples, hardening effect must be realized.

For the airfoils where the WDE test perpendicular to the treated surface (Figure 5-5b), the LSP treatment had limited beneficial effect in mitigating the erosion damage during the advanced erosion stage at a relatively low speed (300 m/s). At 350 m/s, where the test

condition is severe, the induced compressive residual stresses showed no beneficial effect on the airfoil geometry. Comparing with the T-shaped sample geometry, the WDE performance of the treated airfoil condition at relatively low speed (300 m/s) could have been influenced by the induced compressive residual stresses via LSP. This is because the induced compressive residual stresses are through the airfoil thickness. Hence, erosion damage is improved to some degree by resisting further crack propagations especially at advanced stages. This observation is in accord with the study in [148].

5.3.3. WDE damage evolution

During the erosion tests, optical macrographs were taken after every interval. This is to observe the erosion initiation and progression on the As-M and LSP conditions. Figures 5-14a and b show the macrographs taken during tests at 250 and 300 m/s which correspond to WDE curves in Figure 5-10. The erosion initiation started with the emergence of erosion trace line. Figure 5-14a shows this initiation process on the As-M condition after 6 minutes of exposure at 250 m/s. This is the incubation stage where mass loss is negligible. Compared with LSP condition, similar erosion trace line was seen after the same 6 minute exposure. After 10 minutes of exposure (Figure 5-14a), both conditions showed formation of small isolated pits along the trace line, thus indicating early stage of the erosion damage. Here, the As-M and LSP conditions showed mass losses of 0.0003 and 0.0002 g, respectively. With additional impacts (after 16 minutes), large isolated pits were formed and gradual pit growth was observed in the As-M and LSP conditions. At this point, mass losses of 0.012 and 0.013 g were recorded for the As-M and LSP condition, respectively. After 56 minutes, complete craters were formed and mass loss of 0.084 g was observed for both As-M and LSP conditions. Similarly, increasing the impact speed from 250 to 300 m/s (Figure 5-14b), quicker erosion initiation and progression were observed. For instance, after 6 minutes of exposure, formation of pits and gradual pit growth were observed in both As-M and LSP

conditions compared to the pit growth after 10 minutes at 250 m/s (Figure 5-14a). ER_{max} was reached after 16 minutes of exposure (11.52 x 10^5 impingements) after which a decrease in the rate was observed for both conditions (Figure 5-10b).
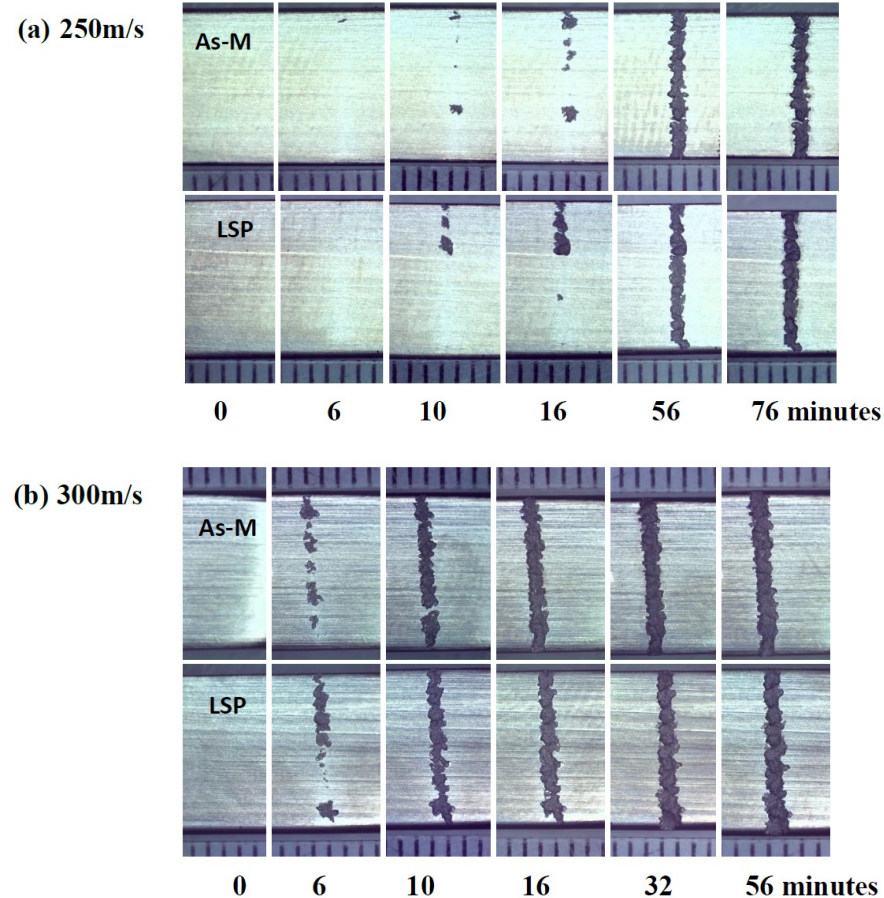
Figure 5-14: Optical macrographs showing the erosion evolution and progression on As-M and LSP samples tested at (a) 250 m/s and (b) 300 m/s. The scale shown in each image is in mm.

From the optical macrographs shown in Figure 5-14, it can be said that decreasing the impact speed delays the erosion initiation and progression. The early erosion initiation and progression at high impact speeds are due to the significant impact stresses. This is attributed to the high impacts pressure and the radial outflows (lateral jetting) of the liquid droplets. It is worth noting that with increased exposure time/droplet impacts, both the depth and the width of the craters are increased [11]. At 250 m/s, crater width of less than 1 mm and greater than 1 mm were observed on the both As-M and LSP conditions after 10 and 76 minutes, respectively. This observation is also true when comparing the crater width/depth for

different speeds at the same exposure. For instance, comparing the crater widths after 16 minutes of exposure at 250 m/s and 300 m/s, it can be observed that crater width of less than 1 mm and greater than 1 mm were observed at 250 m/s and 300 m/s, respectively. This is also the case when comparing the As-M and LSP conditions. This is due to the continuous droplet impacts and the radial liquid outflows. At all exposure times shown in Figures 5-14a and b, similar erosion evolution and progression were observed for the As-M and LSP conditions. This further indicates that LSP had no benefit in enhancing the WDE performance for this sample geometry. This can be attributed to the unchanged microstructure and lack of appreciable increase in microhardness after peening.

Similar to Figure 5-14, Figure 5-15 shows the erosion evolution and progression for the LSP and As-M airfoil samples at 350 m/s using 460 μm droplet size which correspond to the WDE curve in Figure 5-12a . Due to the sample geometry, images were taken at two different orientations. From Figure 5-15, both As-M and LSP conditions showed similar erosion initiation and progression. Isolated pits/craters were observed after 9 minutes of exposure due to the shower head nozzle employed. Here, mass losses of 0.0068 and 0.0077 g were observed on the LSP and As-M conditions, respectively. After 21 minutes of exposure, the craters merged into one another due to the continuous liquid impacts and lateral jetting, causing significant loss of material. At this stage, the formed craters became deeper and cumulative mass losses of 0.0235 and 0.0249 g were observed for the LSP and As-M conditions, respectively. With additional exposure (after 182 minutes), the craters further deepened and widened due to the accumulated liquid impacts and the radial outflows. Mass loss of 0.0913 and 0.0873 g were recorded for the LSP and As-M conditions, respectively. Both As-M and LSP conditions showed crater depth of <1mm and ~2mm after 21 and 182 minutes, respectively. Based on Figure 5-15, the WDE performance of As-M and LSP airfoils is the same. This is also the case for the test at 350 m/s using 200 μm droplet size. The effect

of LSP and the associated compressive residual stresses had no benefit in mitigating erosion at this speed (350 m/s).
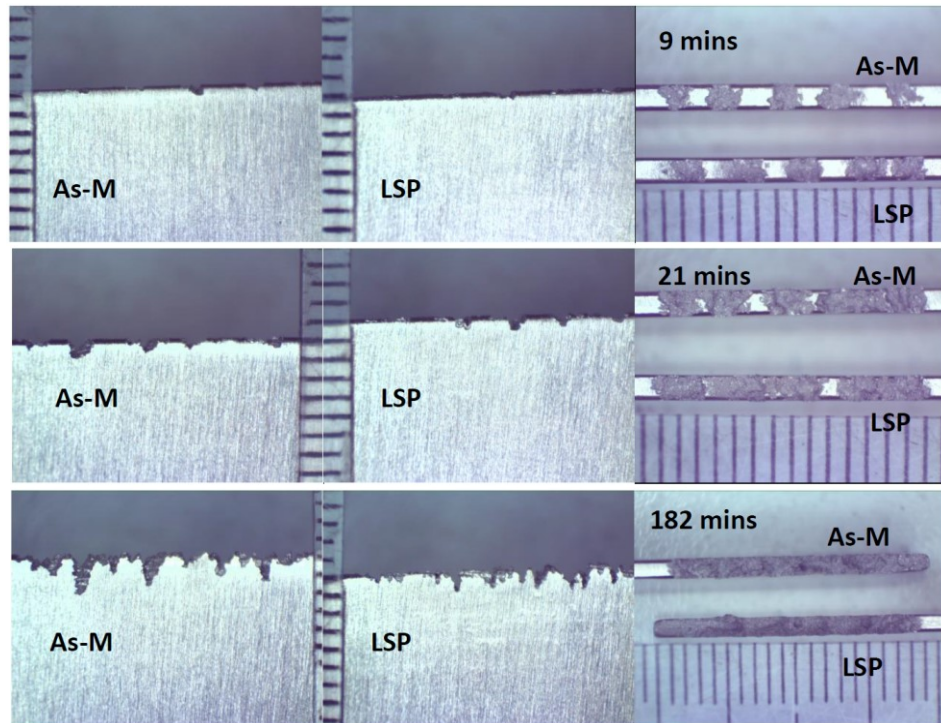
Figure 5-15: Optical macrographs showing the erosion evolution and progression on As-M and LSP airfoil samples at 350 m/s using 460 μm. The scale shown in each image is in mm.

5.3.4. WDE and Fatigue damage

Despite researchers [9,11,117] associating WDE to fatigue-like damage due to the continuous liquid impingements in a cyclic fashion, the question still remains, is fatigue mechanism dominating in WDE?. Also, the perception that compressive residual stresses enhance fatigue life is becoming a fact. If fatigue is dominating in WDE, then processes that induce deep and large compressive residual stresses such as LSP should mitigate erosion damage. However, this does not seem to be the case for enhancing water droplet erosion resistance. Even though fatigue-like features such as striations during WDE damage have been observed [133], the likelihood that fatigue-like mechanism is dominating in WDE is unlikely. If this is the case, the level of residual stresses reached via LSP should have been sufficient to mitigate erosion damage. It has been mentioned that compressive residual stresses through the thickness of the airfoil samples could have arrested further crack

122

propagations. These are normal cracks which could be observed in other damages such as stress corrosion cracking (SCC) not only limited to WDE. It is worth noting that only the effect of continuous liquid impacts is usually considered when ascribing WDE to fatigue while ignoring the effect of the continuous liquid lateral jetting after the impacts. The continuous lateral jetting which is not the case in real fatigue damage could be more damaging than liquid impacts especially at high impact speeds. It has been reported that increase in impact speed has significant effect on the lateral jetting and the resulting damage [133]. Hence, WDE damage should be viewed and understood as a synergy of both continuous liquid impacts and the lateral jetting.

5.4. Conclusions

This work studies the effect of LSP on the WDE performance of Ti-6Al-4V for the first time. The work explores the influence of impact speed on two sample geometries (T-shaped flat and airfoil). The following conclusions can be drawn:

1. LSP treatment using 2 and 3 pulses per unit area induces significant levels of compressive residual stress. However, for the treatment approach and conditions used in this work, LSP shows little or no effect on the Ti-6Al-4V microstructure and microhardness.

2. WDE results show similar WDE performance for the T-shaped flat LSP and As-M conditions at all tested speeds (150 m/s to 350 m/s). At 150 m/s, both LSP and As-M conditions show no erosion damage after 840 minutes (30 million impingements).

3. Both LSP and As-M conditions show similar ER_{max} and speed exponent value of 8.9. Hence, for the T-shaped fat geometry, LSP treatment shows no beneficial effect in enhancing the WDE performance.

4. Despite LSP inducing compressive residual stresses, the residual stresses reached in this work do not improve WDE performance. Since LSP is proven to improve fatigue

behaviour of Ti-6Al-4V alloy, this indicates that the fatigue-like mechanism is not dominating in WDE.

5. For the airfoil geometry, WDE curves show similar WDE performances LSP and As-M conditions at 350 m/s. At 300 m/s, LSP shows little improvement in WDE resistance at the advanced erosion stage. The compressive residual stress through the sample thickness influences this behaviour.

6. Synergy between surface hardening, microstructural refinement and compressive residual stresses is necessary for significant improvement in water droplet impingement erosion resistance.

Chapter 6 : Conclusions, Contributions and Recommendations

The main outcomes of this thesis are summarized in this chapter. Also, the main contributions of this work in relation to previously published works are highlighted. Suggestions for future research directions are provided.

6.1. Conclusions

The thesis investigates the WDE behaviour/performance of untreated (As-M) and treated Ti-6Al-4V. The influence of impact speed on the WDE performance is detailed. For the first time, the study explores two mechanical surface treatments, LSP and UNSM. Also, the work reports the effect of sample geometries and the effectiveness of these mechanical surface treatments on the WDE performance of Ti-6Al-4V. Two sample geometries, T-shaped flat and airfoil, are employed.

Investigation on the WDE behaviour of bare (As-M) Ti-6Al-4V shows that increasing the impact speed decreases the erosion initiation time and increases the maximum erosion rate (ER_{max}). It is found that ER_{max} increases with the 9 to 10th power of impact speed. A threshold speed range between 150 and 200 m/s was observed for this material after prolonged exposure. The dimensions of erosion crater are influenced significantly with increase in impact speed. From SEM analyses, formation of microcracks, isolated pits and surface asperities are the main erosion features during the early stage of the erosion damage. At advanced WDE stage, the dominating mode of material removal is the hydraulic penetration. More so, fatigue striations, side wall cracks, sub-surface cracks, material folding and upheaving were also observed at the advanced stage. Impact speed influences the liquid lateral jetting at the advanced water droplet erosion stage. In this study, it was shown that lateral jetting is more apparent with increase in impact speed even with relatively low number of impingements/less exposure time.

In the second part of the work, the effect of UNSM treatment on the WDE performance of Ti-6Al-4V is reported. UNSM treatment reveals surface features such as microdimples and microtracks due to the ball impacts. Also, the treatment induces deep levels of compressive residual stress. In this work, compressive residual stresses were induced in the parallel and transverse directions down to 0.25 mm. UNSM treatment is associated with severe plastic deformations, thus the process reveals mechanical deformation marks. This translates to significant changes in the surface and sub-surface layers after processing. Hence, material properties such as microhardness are enhanced due to variation in grain sizes across the depth of the ultrasonically modified layer. In this work, the highest microhardness was observed at around 30 μm below the top surface. WDE results reveal that UNSM T-shaped flat condition shows enhanced WDE performances at speeds of 250, 275 and 300 m/s compared with the As-M condition. This is attributed to the modified microstructure and improved microhardness. At speed of 350 m/s, both conditions show similar WDE performance. The effects of UNSM and its attributes diminished with increasing impact speed. UNSM airfoil shows more mass loss at the advanced stages as compared with the As-M condition at 350 m/s. At 300 m/s, UNSM airfoil mildly improves WDE performance at the advanced stages compared with the As-M condition.

Finally, this study investigates the influence of LSP and its associated attributes on the WDE performance of Ti-6Al-4V. LSP condition shows significant level of induced compressive residual stress compared to As-M condition. However, LSP shows a mild increase in the microhardness which is attributed to the unchanged microstructure after LSP. WDE results show that the T-shaped flat LSP and As-M conditions had similar WDE performance at all tested speeds. Similar erosion initiation times and ER_{max} are observed for both conditions. The ER_{max} increases with the 9th power of impact speed for both LSP and As-M flat samples. Optical macrographs reveal that both peened and unpeened conditions

had the same erosion evolution and progression. The erosion curves for different WDE testing conditions support these observations. In this work, the LSP technique shows no enhanced WDE performance in peened flat samples for all tested speeds. The LSP and As-M airfoil conditions show similar WDE performances at 350 m/s. However, at advanced stage, LSP condition shows little resistance compared to As-M condition at 300 m/s.

The notion that compressive residual stresses enhance fatigue life is becoming a fact. However, this does not seem to be the case for enhancing water droplet erosion resistance. Even though this work observes fatigue-like features such as striations during WDE damage, the likelihood that fatigue-like mechanism is dominating in WDE is unlikely. This work also shows that treating both sides of the airfoil proves to be slightly beneficial in arresting further crack propagations at relatively low speed (300 m/s). This is due to the compressive residual stresses across the thickness of the airfoil. This work indicates that compressive residual stresses induced by mechanical surface treatments might be more effective in the airfoil geometry than the T-shaped geometry.

6.2. Contributions

Due to the urgent need to address the issue of WDE especially in the power generation industry, this study contributes to the on-going understanding of the WDE phenomenon. In previous studies, erosion testing at high impact speeds was a challenge due to limitations of the test facilities and/or testing conditions. For instance, most test facilities employed rotating arm apparatus and the water spraying was on a stationary target. In this work, a state-of-the-art rotating disc water erosion testing rig that reaches up to 500 m/s linear speed (equivalent to 20,000 rpm rotational speed) is used. In this rig, erosion parameters such as impact speed and droplet size can be controlled accurately and repeatable results can be achieved. The repeatability of the results has been demonstrated in this work. More so, the results can be used in physical simulation of the WDE process as experienced in real life situations. Also, in

previous studies, only a narrow range of impact speeds is employed hence, there is a need to study WDE behaviour at a wide range of impact speeds. For these reasons, a range of impact speed from 150 to 350 m/s was studied and the threshold velocity of 150 m/s $\leq$ V$_{threshold}$ <200 m/s was found for this material. Previously, much attention was not given to the effect of sample geometry on WDE performance. This study employed special sample geometry (airfoil) which is close to the real life compressor blade leading edge.

In mitigating erosion damage, surface treatments such as coatings and laser surface treatments have been employed to combat WDE. However, there are still challenges related to surface imperfections and microcracks after such surface modifications. These surface defects are detrimental during WDE tests. Recently, mechanical surface treatments have received considerable attention. For the most part of the literature, mechanical surface treatments are employed to enhance fatigue life and successful results have been achieved. This was attributed to the induced compressive residual stresses. Also, due to the continuous liquid impacts in a cyclic fashion, WDE has been likened to fatigue. Moreover, crack initiation and propagation have been found to significantly influence WDE damage behaviour. It is well known that compressive residual stresses retard crack initiation and arrest further propagation as well as enhance fatigue life. At this point, one would expect mechanical surface treatments to mitigate the WDE damage to a certain degree. Not long ago, deep rolling which is a mechanical surface treatment was explored in order to enhance WDE performance of Ti-6Al-4V. However, no enhanced WDE performance was observed for the deep rolled condition. For the first time, two mechanical surface treatments, LSP and UNSM, were employed. Influence of these treatments on the WDE performance of Ti-6Al-4V was experimentally studied. It was established in this work that specific mechanical surface treatment mitigates erosion damage at certain conditions. For instance, UNSM surface treatment employed enhanced the WDE performance especially at 250, 275 and 300

128

m/s impact speeds for the flat samples. Whereas, LSP and its associated attributes did not show improved WDE performance of Ti-6Al-4V for the flat samples. Moreover, no deterioration in the performance was observed.

The combined effect of surface treatment and sample geometry on the WDE performance was established. For instance, treating the airfoil on both sides and having compressive residual stresses through the thickness showed a slight reduction in the erosion rate especially at the advanced stage of erosion. It is worth mentioning that companies are now interested in testing erosion damage up to the advanced stages. This might be a viable contribution that can be applied. Hence, sample geometry plays a significant role in understanding WDE performance.

Three journal articles were used in the body of the thesis (chapters 3, 4 and 5). In addition, a review article (number 1 below) related to LSP has been published and conference paper presented. Another article is under preparation and will be submitted afterwards. They are listed as follows:

Journal Papers

(1) **A. K. Gujba,** M. Medraj: Laser peening process and its impact on materials properties in comparison with shot peening and ultrasonic impact peening. *Materials*, Vol. 7, 2014, pp. 7925-7974. Doi:10.3390/ma7127925.

(2) **A. K. Gujba**, A. Amanov, M. Medraj: Influence of sample geometry and mechanical surface treatment on the WDE performance of Ti-6Al-4V. (Under preparation)

Conference Presentation

(1) **A. K. Gujba**, D. Kevorkov, L. Hackel, M. Medraj: Mechanism of material removal in Ti-6Al-4V during the incubation and advanced water droplet erosion stages. The 4th International Conference and Exhibition on Materials Science & Engineering, 14-16th September, 2015, Orlando, Florida, USA.

6.3. Recommendations

WDE is a complex phenomenon due to several interacting parameters involved in the water droplet erosion process. Efforts have been made to mitigate the erosion damage however, identifying a single parameter for WDE resistance still remains a challenge. For this reason, there is still need for more studies. In order to compliment the on-going search for best and reliable techniques to mitigate WDE damage, some suggestions for future works are as follows.

- Based on this work, it does not seem that the induced compressive residual stresses are beneficial in enhancing WDE resistance. For this reason, more research work is still needed in order to establish the influence of compressive residual stresses on the WDE performance of materials. This can be achieved by exploring other processes that induces compressive residual stress such as warm laser shock peening (WLSP) or thermal engineered LSP. WLSP is a new emerging technique that integrates the merits from the conventional LSP process, dynamic strain aging (DSA) and dynamic precipitation (DP) to enhance material performance [82,169,170]. This technique stabilizes the induced compressive residual stresses and modifies the microstructure. Hence, careful selection of LSP temperature, pre-treatment and tempering temperatures as well as other processing parameters should be studied.

- In this work, impact speeds and droplet sizes in the range of 150 to 350 m/s and 200-463 μm were used during WDE tests. More studies with varying impingement conditions are still needed. For instance, further reducing the droplet size ranging from 100 - 150 μm, varying the stand-off distance, flow rate, impact angle and surface conditions could reveal different erosion behaviour.

- The thesis work presented is solely experimental studies. However, there is still need to have extensive studies using simulation. Combining simulations and experimental test results would provide better understanding of the erosion process.

- Experimental conditions used in this thesis are similar to the observed conditions in gas turbine compressor blades in service. In steam turbines, condensated water droplets impact blades at significantly larger speeds causing serious erosion damage problems. Hence, the current work could be extended to steam turbine applications.

References

[1]   C. B. Meher-Homji, T. R Mee: Gas turbine power augmentation by fogging of inlet air. Proceedings of 28th Turbomachinery Symposium, ASME International, Houston, Texas, USA, 4th Sept. 1999, pp. 93-114.

[2]   Energy Information Agency: 2005 Database of U.S Department of energy. Available online: http://energy.gov/data/open-energy-data, (28/10/2013).

[3]   D. Punwani: Turbine inlet cooling: An energy solution that's better for the environment, ratepayers and plant owners. Presented at POWER-GEN International, Orlando, Florida, USA, 2nd Dec. 2008, pp. 1-9.

[4]   S. Duncan: Thermal energy storage and its effect on CO_2 at the Source, Presentation at 2007 ASHRAE technical committee summer meeting, Long Beach, California, USA, 23-27th Jun. 2007.

[5]   T. Giampaolo: The gas turbine handbook: Principles and practice, 3rd edition, Fairmont Press, New York, USA, 2006.

[6]   J. R. Khan: Fog cooling, wet compression and droplet dynamics in gas turbine compressors. PhD dissertation, University of New Orleans, USA, 2009.

[7]   ASTM G40-15: Standard terminology relating to wear and erosion, ASTM International, West Conshohocken, PA, 2015. Available online: www.astm.org.

[8]   H. S. Kirols: Water droplet erosion: Influencing parameters, representation and comparisons. Master's thesis, Concordia University, Montreal, Canada, 2015.

[9]   N. Kamkar: Water droplet erosion mechanisms of Ti-6Al-4V. PhD Dissertation, École de Technologie Supérieure (ÉTS), Montreal, QC, Canada, 2014.

[10]   F. G. Hammitt, F. J. Heymann: Liquid-erosion failures, failure analysis and prevention, ASM Handbook, ASM International, Vol. 11, 1986, pp. 163–171.

[11] D. Ma, A. Mostafa, D. Kevorkov, P. Jedrzejowski, M. Pugh, M. Medraj: Water impingement erosion of deep-rolled Ti64. Metals, Vol. 5, No. 3, 2015, pp. 1462–1486.

[12] F. Heymann: Liquid impingement erosion. ASM Handbook. Materials Park. OH: ASM International, Vol. 18, 1992, pp. 221-232.

[13] F. Heymann: High speed liquid impact between a liquid drop and a solid surface. Journal of Applied Physics, Vol. 40, No. 13, 1969, pp. 5113–5122.

[14] M. C. Kong, D. Axinte, W. Voice: Aspects of material removal mechanism in plain waterjet milling on gamma titanium aluminide. Journal of Material Procesing Technology, Vol. 210, No. 3, 2010, pp. 573–584.

[15] K. F. Graff: Wave motion in elastic solids. Dover Publications, Inc., New York, 2012.

[16] S. Honghui, J. E. Field: Stress waves propagation in solids under high-speed liquid impact. Science in China Series G Physics, Mechanics and Astronomy, Vol. 47, No. 6, 2004, pp. 752–766.

[17] H. S. Kirols, D. Kevorkov, A. Uihlein, M. Medraj: The effect of initial surface roughness on water droplet erosion behaviour. Wear, Vol. 342-343, 2015, pp. 198-209.

[18] F. J. Heymann: Erosion by liquids. Machine Design, 1970, pp. 118–124.

[19] G. F. Schmitt: Liquid and solid particle impact erosion. Technical Report AFML-TR-79-4122, Air Force Materials Laboratory, Wright Patterson, Air Force Base, Ohio, USA,1979.

[20] A. Arbor, S. Hattori, M. Takinami, T. Otani: Comparison of cavitation erosion rate with liquid impingement erosion rate. Proceedings of the 7th International Symposium on Cavitation, Ann Arbor, Michigan, USA, 17-22nd Aug. 2009, Paper No. 32, pp. 1–6.

[21] J. E. Field, J. J. Camus, M. Tinguely, D. Obreschkow, M. Farhat: Cavitation in impacted drops and jets and the effect on erosion damage thresholds. Wear, Vol. 290–291, 2012, pp. 154–160.

[22] L. Huang, J. Folkes, P. Kinnell, P. H. Shipway: Mechanisms of damage initiation in a titanium alloy subjected to water droplet impact during ultra-high pressure plain waterjet erosion. Journal of Material Processing Technoogy, Vol. 212, No. 9, 2012, pp. 1906–1915.

[23] J. Foldyna, J. Klich, P. Hlaváček, M. Zeleňák, J. Ščučka: Erosion of metals by pulsating water jet. Tehnicki Vjesnik, Vol. 2, 2012, pp. 381–386.

[24] M. S. Mahdipoor, F. Tarasi, C. Moreau, A. Dolatabadi, M. Medraj: HVOF sprayed coatings of nano-agglomerated tungsten-carbide/cobalt powders for water droplet erosion application. Wear, Vol. 330–331, 2015, pp. 338–347.

[25] B. S. Mann: Water droplet and cavitation erosion behavior of laser treated stainless steel and titanium alloy: Their similarities. Journal of Materials Engineering and Performance, Vol. 22, No. 12, 2013, pp. 3647-3656.

[26] J. I. Robinson, R. C. Reed: Water droplet erosion of laser surface treated Ti-6A1-4V. Wear, Vol. 187, 1995, pp. 360–367.

[27] W. F. Adler, R. F.Vyhnal: Rain erosion of Ti-6Al-4V. In 4th International Conference on Rain Erosion and Associated Phenomena, Meersburg, Germany, 8-10th May, 1974, pp. 536–569.

[28] M. S. Mahdipoor, H. S. Kirols, D. Kevorkov, P. Jedrzejowski, M. Medraj: Influence of impact speed on water droplet erosion of TiAl compared with Ti6Al4V. Scientific Reports, Vol. 5, 2015, Article Number: 14182 (17 pages).

[29] ASTM G73-10: Standard test method for liquid impingement erosion using rotating apparatus. ASTM International, West Conshohocken, PA, 2010. Available online: www.astm.org.

[30] F. Heymann: On the time dependence of the rate of erosion due to impingement or cavitation. ASTM STP 408, American Society for Testing and Materials, 1967, pp. 70–110.

[31] C. Gerdes, A. Karimi, H. Bieler: Water droplet erosion and microstructure of laser nitrided Ti-6A1-4V. Wear, Vol. 186–187, Part 2, 1995, pp. 368–374.

[32] V. A. Ryzhenkov, A. I. Lebedeva, A. F. Mednikov: Erosion wear of the blades of wet-steam turbine stages: Present state of the problem and methods for solving it. Thermal Engineering, Vol. 58, No. 9, 2011, pp. 713–718.

[33] B. S. Mann, V. Arya: An experimental study to corelate water jet impingement erosion resistance and properties of metallic materials and coatings. Wear, Vol. 253, No. 5–6, 2002, pp. 650–661.

[34] A. K. Gujba, M. Medraj: Laser peening process and its impact on materials properties in comparison with shot peening and ultrasonic impact peening. Materials, Vol. 7, No. 12, 2014, pp. 7925–7974.

[35] S. Hattori: Effects of impact velocity and droplet size on liquid impingement erosion. International Symposium on the Ageing Management & Maintenance of Nuclear Power Plants (ISaG 2010), Tokyo, Japan, 27-28th May. 2010, pp. 58–71.

[36] X. Ye, Y. Ye, G. Tang: Effect of electropulsing treatment and ultrasonic striking treatment on the mechanical properties and microstructure of biomedical Ti-6Al-4V alloy. Journal of Mechanical Behaviour of Biomedical Materials, Vol. 40, 2014, pp. 287–296.

[37] A. Cherif, Y. Pyoun, B. Scholtes: Effects of ultrasonic nanocrystal surface modification (UNSM) on residual stress state and fatigue strength of AISI 304. Journal of Material Engineering and Performance, Vol. 19, No. 2, 2010, pp. 282–286.

[38]   K. Y. Zhang, Y. S. Pyoun, X. J. Cao, B. Wu, R. Murakami: Fatigue properties of sus 304 stainless steel after ultrasonic nanocrystal surface modification (UNSM). International Journal of Modern Physics: Conference Series, Vol. 6, 2012, pp. 330–335.

[39]   M. Yasuoka, P. Wang, K. Zhang, Z. Qiu, K. Kusaka, Y. S. Pyoun, R. Murakami: Improvement of the fatigue strength of SUS304 austenite stainless steel using ultrasonic nanocrystal surface modification. Surface & Coatings Technology, Vol. 218, 2013, pp. 93–98.

[40]   A. H. Clauer, B. P. Fairand: Interaction of laser-induced stress waves with metals. Proc. ASM Conference Applications of Lasers in Materials Processing; Washington DC, 1979.

[41]   C. Rubio-González, C. Felix-Martinez, G. Gomez-Rosas, J. L. Ocaña, M. Morales, J. A. Porro: Effect of laser shock processing on fatigue crack growth of duplex stainless steel. Materials Science and Engineering A, Vol. 528, No. 3, 2011, pp. 914–919.

[42]   A. Amanov, I. S. Cho, D. E. Kim, Y. S. Pyun: Fretting wear and friction reduction of CP titanium and Ti–6Al–4V alloy by ultrasonic nanocrystalline surface modification. Surface & Coatings Technology, Vol. 207, 2012, pp. 135–142.

[43]   I. S. Cho, J. Park, Y. Jeon: Fatigue behaviour of Ti-6Al-4V alloy under combined low and high cycle and ultrasonic loading. International Journal of Materials and Product Technology,Vol. 48, 2014, pp. 18–33.

[44]   A. Amanov, J. Kim, Y. Pyun, T. Hirayama, M. Hino: Wear mechanisms of silicon carbide subjected to ultrasonic nanocrystalline surface modification technique. Wear, 2014, pp. 1–9.

[45] B. Wu, P. Wang, Y. S. Pyoun, J. Zhang, R. Murakami: Effect of ultrasonic nanocrystal surface modification on the fatigue behaviors of plasma-nitrided S45C steel. Surface & Coatings Technology, Vol. 213, 2012, pp. 271–277.

[46] S. J. Hong, G. H. Hwang, W. K. Han, S. G. Kang: Cyclic oxidation behavior of Pt-modified aluminide coating treated with ultrasonic nanocrystal surface modification (UNSM) on Ni-based superalloy. Surface & Coatings Technology, Vol. 205, No. 8–9, 2011, pp. 2714–2723.

[47] A. Amanov, Y. S. Pyun, S. Sasaki: Effects of ultrasonic nanocrystalline surface modification (UNSM) technique on the tribological behavior of sintered Cu-based alloy. Tribology International, Vol. 72, 2014, pp. 187–197.

[48] A. Amanov, O. V. Penkov, Y. S. Pyun, D. E. Kim: Effects of ultrasonic nanocrystalline surface modification on the tribological properties of AZ91D magnesium alloy. Tribology International, Vol. 54, 2012, pp. 106–113.

[49] C. Ye, A. Telang, A. S. Gill, S. Suslov, Y. Idell, K. Zweiacker, J. M. K. Wiezorek, Z. Zhou, D. Qian, S. R. Mannava, V. K. Vasudevan: Gradient nanostructure and residual stresses induced by ultrasonic nano-crystal surface modification in 304 austenitic stainless steel for high strength and high ductility. Material Science & Engineering A, Vol. 613, 2014, pp. 274–288.

[50] B. P. Fairland, A. H. Clauer: Laser generation of high-amplitude stress waves in materials. Journal of Applied Physics, Vol. 50, 1979, pp. 1497–1502.

[51] B. P. Fairland, B. A. Wilcox, W. J. Gallagher, D. N. Williams: Laser shock-induced microstructural and mechanical property changes in 7075 aluminum. Journal of Applied Physics, Vol. 43, 1972, pp. 3893–3895.

[52] B. P. Fairand, A. H. Clauer, B. A. Wilcox: Laser shock hardening of weld zones in Aluminum alloys. Metallurgical Transactions A, Vol. 8A, 1976, pp. 1871–1876.

[53] A. H. Clauer, B. P. Fairand, and B. A. Wilcox: Pulsed laser induced deformation in an Fe-3 wt Pct Si alloy. Metallurgical Transactions A, Vol. 8, No. 1, 1977, pp. 119–125.

[54] C. Montross, T. Wei, L. Ye, G. Clark, Y. Mai: Laser shock processing and its effects on microstructure and properties of metal alloys: A review. International Journal of Fatigue, Vol. 24, No. 2002, 2006, pp. 1021–1036.

[55] P. Peyre, R. Fabbaro: Laser shock processing: A review of the physics and applications. Optical and Quantum Electronics, Vol. 27, 1995, pp. 1213–1229.

[56] P. Peyre, X. Scherpereel, L. Berthe, C. Carboni, R. Fabbro, G. Béranger, C. Lemaitre: Surface modifications induced in 316L steel by laser peening and shot-peening. Influence on pitting corrosion resistance. Materials Science and Engineering: A, Vol. 280, No.2, 2000, pp. 294–302.

[57] A. H. Clauer: Laser shock of peening for fatigue resistance. surface performance of titanium, The Minerals, Metals and Materials Society (TMS), 1996, pp. 217–230.

[58] X. C. Zhang, Y. K. Zhang, J. Z. Lu, F. Z. Xuan, Z. D. Wang, S. T. Tu: Improvement of fatigue life of Ti–6Al–4V alloy by laser shock peening. Materials Science and Engineering A, Vol. 527, No. 15, 2010, pp. 3411–3415.

[59] Y. Guo, R. Caslaru: Fabrication and characterization of micro dent arrays produced by laser shock peening on titanium Ti–6Al–4V surfaces. Journal of Materials Processing Technology, Vol. 211, No. 4, 2011, pp. 729–736.

[60] N. S. Brar, A. Hopkins, M. W. Laber: Laser shock peening of titanium 6-4 alloy. AIP Conference Proceedings, Vol. 505, No. 1, 2000, pp. 435–438.

[61] G. Tani, L. Orazi, A. Fortunato, A. Ascari, G. Campana: Warm laser shock peening-new developments and process optimization. CIRP Annals - Manufacturing Technology, Vol. 60, No.1, 2011, pp. 219–222.

[62] C. Rubio-González, G. Gomez-Rosas, J. Ocaña, C. Molpeceres, A. Banderas, J. Porro,

M. Morales: Effect of an absorbent overlay on the residual stress field induced by laser shock processing on aluminum samples. Applied Surface Science, Vol. 252, No. 18, 2006, pp. 6201–6205.

[63] H. Chen, A. Claudet, T. Zaleski, C. Dane, L. Lane, L. Hackel, F. Harris, J. Halpin: Laser process form thick, curved metal parts. Science and Technology Review, 2003, pp. 16-17.

[64] O. Hatamleh: A comprehensive investigation on the effects of laser and shot peening on fatigue crack growth in friction stir welded AA 2195 joints. International Journal of Fatigue, Vol. 31, No. 5, 2009, pp. 974–988.

[65] O. Hatamleh, A. DeWald: An investigation of the peening effects on the residual stresses in friction stir welded 2195 and 7075 aluminum alloy joints. Journal of Materials Processing Technology, Vol. 209, No. 10, 2009 pp. 4822–4829.

[66] C. Montross, V. Florea, M. Swain: The influence of coatings on subsurface mechanical properties of laser peened 2011-T3 aluminum. Journal of Materials Science, Vol. 36, 2011, pp. 1801–1807.

[67] G. J. Cheng, M. A. Shehadeh: Dislocation behavior in silicon crystal induced by laser shock peening-A multiscale simulation approach. Scripta Materialia, Vol. 53, No. 9, 2005, pp. 1013–1018.

[68] X. Hong, S. Wang, D. Guo, H. Wu, J. Wang, Y. Dai, X. Xia, Y. Xie: Confining medium and absorptive overlay: Their effects on a laser-induced shock wave. Optics and lasers in Engineering, Vol. 29, 1998, pp. 447–455.

[69] Z. Zhou, S. Bhamare, G. Ramakrishnan, S. R. Mannava, K. Langer, Y. Wen, D. Qian, V. K. Vasudevan: Thermal relaxation of residual stress in laser shock peened Ti–6Al–4V alloy. Surface & Coatings Technology, Vol. 206, No. 22, 2012, pp. 4619–4627.

[70] Y. Cao, Y. Shin, B. Wu: Parametric study on single shot and overlapping laser shock peening on various metals via modeling and experiments. Journal of Manufacturing Science and Engineering, Vol. 132, No. 6, 2010, pp. 061010-7.

[71] J. Ruschau, R. John, S. R. Thompson, T. Nicholas: Fatigue crack nucleation and growth rate behavior of laser shock peened titanium. International Journal of Fatigue, Vol.21, 1999, pp. 199–209.

[72] B. N. Mordyuk, Y. V. Milman, M. O. Iefimov, G. I. Prokopenko, V. V. Silberschmidt, M. I. Danylenko, A. V. Kotko: Characterization of ultrasonically peened and laser shock peened surface layers of AISI 321 stainless steel. Surface & Coatings Technology., Vol. 202, No. 19, 2008, pp. 4875–4883.

[73] U. Trdan, J. Grum: Evaluation of corrosion resistance of AA6082-T651 aluminium alloy after laser shock peening by means of cyclic polarisation and ElS methods. Corrosion Science, Vol. 59, 2012, pp. 324–333.

[74] S. Kalainathan, S. Sathyajith, S. Swaroop: Effect of laser shot peening without coating on the surface properties and corrosion behavior of 316L steel. Optics and lasers in Engineering, Vol. 50, No. 12, 2012, pp. 1740–1745.

[75] L. Wagner, M. Mhaede, M. Wollmann, I. Altenberger, Y. Sano: Surface layer properties and fatigue behavior in Al 7075-T73 and Ti-6Al-4V: Comparing results after laser peening; shot peening and ball-burnishing. International Journal of Structural Integrity, Vol. 2, No. 2, 2011, pp. 185–199.

[76] C. Sudha, P. Parameswaran, R. Krishnan, S. Dash, M. Vijayalakshmi: Effect of Laser Shock Processing on the Microstructure of 304(L) Austenitic Stainless Steel. Materials and Manufacturing Processes, Vol. 25, No. 9, 2010, pp. 956–964.

[77] D. Grevey, L. Maiffredy, A. Vannes: Laser shock on a TRIP alloy: mechanical and metallurgical consequences. Journal of Material Science, Vol. 27, 1992, pp. 2110–2116.

[78] Y. Sano, M. Obata, T. Kubo, N. Mukai, M. Yoda, K. Masaki, Y. Ochi: Retardation of crack initiation and growth in austenitic stainless steels by laser peening without protective coating. Materials Science and Engineering: A, Vol. 417, No. 1–2, 2006, pp. 334–340.

[79] A. Kruusing: Underwater and water-assisted laser processing: Part 1-general features, steam cleaning and shock processing. Optics and Lasers in Engineering, Vol. 41, No. 2, 2004, pp. 307–327.

[80] R. Thareja, S. Shukla: Synthesis and characterization of zinc oxide nanoparticles by laser ablation of zinc in liquid. Applied Surface Science, Vol. 253, No. 22, 2007, pp. 8889–8895.

[81] X. Ling, W. Peng, G. Ma: Influence of laser peening parameters on residual stress field of 304 stainless steel. Journal of Pressure Vessel Technology, Vol. 130, No. 2, 2008, pp. 021201-1.

[82] C. Ye, S. Suslov, B. J. Kim, E. A. Stach, G. J. Cheng: Fatigue performance improvement in AISI 4140 steel by dynamic strain aging and dynamic precipitation during warm laser shock peening. Acta Materialia., Vol. 59, No. 3, 2011, pp. 1014–1025.

[83] Y. Jiang, Y. Huang, H. Jin, Y. Gu, A. Ren, L. Huang, X. Qian: Research on precision control of sheet metal forming by laser shock waves with semi-die. Optics Laser Technology, Vol. 45, 2013, pp. 598–604.

[84] S. A. Martinez, S. Sathish, M. P. Blodgett, M. J. Shepard: Residual stress distribution on surface-treated Ti-6AI-4V by x-ray diffraction. Experimental Mechanics, Vol. 43, 2003, pp. 141–147.

[85] S. Srinivasan, D. B. Garcia, M. C. Gean, H. Murthy, T. N. Farris: Fretting fatigue of laser shock peened Ti–6Al–4V. Tribology International, Vol. 42, No. 9, 2009, pp. 1324–1329.

[86] P. Prevéy, D. Hornbach, P. Mason: Thermal residual stress relaxation and distortion in surface enhanced gas turbine engine components. In 17th Heat Treating Society Conference and Exposition and the 1st International Induction Heat Treating Symposium, 1998, pp. 3–12.

[87] F. Baoxiang, Y. Guanjun, M. Xiaonan, Y. Lanlan, W. Xiaodong: Research development of shot peening strenthening of titanium alloys. Titanium Industry Progress. Titanium Industry Progress, No. 03, 2008, pp. 1–5.

[88] P. R. Smith, M.J. Shepard, P.S. Prevey, A. H. Clauer: Effect of power density and pulse repetition on laser shock peening of Ti-6AI-4V. Journal of Materials Engineering and Performance Vol. 9, No. 1, 2000, pp. 33–37.

[89] R. Fabbro, J. Fournier, P. Ballard, D. Devaux, J. Virmont: Physical study of laser-produced plasma in confined geometry. Journal of Applied Physics, Vol. 68, 1990, pp. 775–784, 1990.

[90] Z. Cao, H. Xu, S. Zou, Z. Che: Investigation of surface integrity on TC17 Titanium alloy treated by square-spot laser shock peening. Chinese Journal of Aeronautics, Vol. 25, No. 4, 2012, pp. 650–656.

[91] J. Vaccari: Laser shocking extends fatigue life. American Machinist, 1992, pp. 21–23.

[92] S. Mannava: On the fly laser shcok peening-General Electric Company. US Patent 5,756,965, 1998.

[93] G. Gomez-Rosas, C. Rubio-Gonzalez, J. Ocaña, C. Molpeceres, J. A. Porro, W. Chi-Moreno, M. Morales: High level compressive residual stresses produced in aluminum alloys by laser shock processing. Applied Surface Science, Vol. 252, No. 4, 2005, pp. 883–887.

[94] A. Chahardehi, F. P. Brennan, A. Steuwer: The effect of residual stresses arising from laser shock peening on fatigue crack growth. Engineering Fracture Mechanics, Vol. 77, No. 11, 2010, pp. 2033–2039.

[95] Y. Zhang, J. You, J. Lu, C. Cui, Y. Jiang, X. Ren: Effects of laser shock processing on stress corrosion cracking susceptibility of AZ31B magnesium alloy. Surface Coatings Technology, Vol. 204, No. 24, 2010, pp. 3947–3953.

[96] N. Scherpereel, P. Peyre, R. Fabbro, G. Lederer, N. Celati: Modifications of mechanical and electrochemical properties of stainless steel surfaces by laser shock processing. SPIE Proceedings, lasers in material processing, Munich, Germany, Vol. 3097 , 1997, pp. 546–557.

[97] M. Yoda, B. Newton: Underwater Laser Peening. Welding and Repair Technology for Power Plants Eighth International EPRI Conference, Fort Myers, Florida, 2008, pp. 1–10.

[98] H. Amar, V. Vignal, H. Krawiec, C. Josse, P. Peyre, S. N. da Silva, L. F. Dick: Influence of the microstructure and laser shock processing (LSP) on the corrosion behaviour of the AA2050-T8 aluminium alloy. Corrosion Science, Vol. 53, No. 10, 2011, pp. 3215–3221.

[99] L. Berthe, R. Fabbro, P. Peyre, C. Braham, J. Le: Corrosion Reactivity of Laser-Peened Steel Surfaces. Journal of Materials Engineering and Performance, Vol. 9, 2000, pp. 656–662.

[100] S. Mannava: Technique to prevent or divert cracks-General Electric Company. US Patent 5,569,018, 1996.

[101] C. Dane, L. Hackel, J. Daly, J. Harirson: Laser peening of metals enabling laser technology. Advanced Materials and Processes, 1997, pp. 13–27.

[102] S. Mannava, S. Ferrigno: Laser shock peening for gas turbine engine vane repair-General Electric Company. US Patent 5,675,892, 1997.

[103] S. Mannava, S. Ferrigno, W. D. Cowie: Laser shock peening for gas turbine engine weld repair-General Electric Company. US Patent 5,846,057, 1998.

[104] K. G. Budinski, M. K. Budinski: Engineering materials-properties and selection, 9th Edition, Prentice Hall, New York, USA, 2010.

[105] N. Fujisawa, R. Morita, A. Nakamura: Critical consideration on wall thinning rate by liquid droplet impingement erosion. E-Journal of Advanced Maintenance, Vol. 4, No. 2, 2012, pp. 79–87.

[106] S. Yerramareddy: Effect of operational variables, microstructure and mechanical properties on the erosion of Ti-6Al-4V. Wear, Vol. 142, No. 1, 1991, pp. 253–263.

[107] B. Luiset, F. Sanchette, A. Billard, D. Schuster: Mechanisms of stainless steels erosion by water droplets. Wear, Vol. 303, No. 1–2, 2013, pp. 459–464.

[108] F. J. Heymann: Toward quantitative prediction of liquid impact erosion, Characterization and determination of erosion resistance, ASTM STP 474, American Society for Testing Materials. 1970, pp. 212-248.

[109] M. Ahmad, M. Casey, N. Sürken: Experimental assessment of droplet impact erosion resistance of steam turbine blade materials. Wear, Vol. 267, No. 9–10, 2009, pp. 1605–1618.

[110] A. Thiruvengadam, S. L. Rudy: Experimental and analytical investigations on multiple liquid impact erosion. National Aeronautics and Space Administration (NASA), 1969, pp. 1-93.

[111] G. Hoff, G. Landbein, H. Rieger: Material destruction due to liquid impact in Erosion by Cavitation or Impingement: A symposium presented at the 6-9th annual meeting, American Society for Testing and Materials, Atlanta City, New Jersey, 26th Jun. - 1st Jul. 1966, pp. 42–69.

[112] T. Keil, P. F. Pelz, J. Kadavelil, J. Necker, W. Moser, D. Christ: Droplet Impact vs Cavitation Erosion. Warwick innovative manufacturing research center (WIMRC) 3rd International Cavitation Forum, University of Warwick, UK, Jul. 4-6th 2011, pp. 1–8.

[113] T. Sanada, K. Ando, T. Colonius: A Computational Study of high-speed droplet impact. Fluid Dynamics and Materials Processing, Vol. 7, No. 4, 2011, pp. 329–340.

[114] J. E. Field: The physics of liquid impact, shock wave interactions with cavities, and the implications to shock wave lithotripsy. Physics in Medicine and Biology, Vol. 36, No. 11, 1991, pp. 1475–1484.

[115] Q. Zhou, N. Li, X. Chen, T. Xu, S. Hui, D. Zhang: Analysis of water drop erosion on turbine blades based on a nonlinear liquid–solid impact model. International Journal of Impact Engineering, Vol. 36, No. 9, 2009, pp. 1156–1171.

[116] M. Rein: Phenomena of liquid drop impact on solid and liquid surfaces. Fluid Dynamics Research, Vol. 12, No. 2, 1993, pp. 61–93.

[117] S. Hattori, M. Takinami: Comparison of cavitation erosion rate with liquid impingement erosion rate. Wear, Vol. 269, No. 3–4, 2010, pp. 310–316.

[118] N. Fujisawa, T. Yamagata, S. Takano, K. Saito, R. Morita, K. Fujiwara, F. Inada: The influence of material hardness on liquid droplet impingement erosion. Nuclear Engineering and Design, Vol. 288, 2015, pp. 27–34.

[119] Y. I. Oka, S. Mihara, H. Miyata: Effective parameters for erosion caused by water droplet impingement and applications to surface treatment technology. Wear, Vol. 263, No. 1–6, 2007, pp. 386–394.

[120] N. Fujisawa, T. Yamagata, K. Hayashi, T. Takano: Experiments on liquid droplet impingement erosion by high-speed spray. Nuclear Engineering and Design, Vol. 250, 2012, pp. 101–107.

[121] T. Ikohagi: On evaluation of LDI erosion rate based on fluid/solid coupled simulation. In Proceeding of 8th International Conference Flow Dynamics, 2011, pp. 402–403.

[122] N. Fujisawaa, T. Yamagata, K. Saito, K. Hayashi: The effect of liquid film on liquid droplet impingement erosion. Nuclear Engineering and Design, Vol. 265, 2013, pp. 909–917.

[123] H. Rieger: The damage to metals on high speed impact with water drops. Proceedings of the Rain Erosion Conference held at Meersburg (edited by A.A. Fyall and R.B. King), Royal Aircraft Establishment, Farnborough, England, 1965, pp. 107–113.

[124] W. F. Adler: Analysis of particulate erosion. Wear, Vol. 37, No. 2, 1976, pp. 345–352.

[125] G. P. Thomas: The initial stages of deformation in metals subjected to repeated liquid impact. Philosophical Transactions A, Royal Society of London, Vol. 260, 1996, pp. 140–143.

[126] J. E. Field, M. B. Lesser, J. P. Dear: Studies of two-dimensional liquid-wedge impact and their relevance to liquid-drop impact problems. In Proceedings of the Royal Society of London. Series A, Mathematical and Physical Sciences, London, UK, 8th Oct. 1985, Vol. 401, No. 1821, pp. 225–249.

[127] H. H. Shi, J. P. Dear: Oblique high-speed liquid-solid impact. The Japan Society of Mechanical Engineers, Vol. 35, No. 3, 1992, pp. 285-295.

[128] J. E. Field, D. A. Gorham, J. T. hagan, M. J. Mattewson, M. V. Swain, S. Van der Zwaag: Liquid jet impact and damage assessment for brittle solids. In 5th International conference on Erosion by solid and liquid impact, Cambrigde, UK, 3-6th Sept. 1979, pp. 1–11.

[129] V. A. Joshi: Titanium alloys: An atlas of structures and fracture features, CRC Press, Taylor & Francis Group, USA. 2006.

[130] M. S. Mahdipoor, D.Kevorkov, P. Jedrzejowski, M. Medraj: Water droplet erosion mechanism of nearly fully-lamellar gamma TiAl alloy. Materials and Design, Vol. 89, No. 2, 2015, pp. 81–87.

[131] M. B. Lesser, J. E. Field: The impact of compressible liquids. Annual Review Fluid Mechanics, Vol. 15, 1983, pp. 97–122.

[132] C. T. Kwok (Editor): Laser surface modification of alloys for corrosion and erosion resistance. 1st edition, Woodhead Publishing, 2012, pp. 155–174.

[133] A. K. Gujba, L. Hackel, D. Kevorkov, M. Medraj: Water droplet erosion behaviour of Ti-6Al-4V and mechanisms of material removal at the early and advanced stages. Wear, Vol. 358-359, 2016, pp. 109-122.

[134] ASM aerospace specification metals: Titanium Ti-6Al-4V (Grade 5). ASM Material Data Sheet. Available online: www.aerospacemetals.com.

[135] S. Spanrad, J. Tong: Characterisation of foreign object damage (FOD) and early fatigue crack growth in laser shock peened Ti–6Al–4V aerofoil specimens. Materials Science and Engineering A, Vol. 528, No. 4–5, 2011, pp. 2128–2136.

[136] M. E. Hilley (Editor): Residual stress measurement by X-ray diffraction - (SAE) J784a: Report of iron and steel technical committee approved September 1960 and last revised by fatigue design and evaluation committee August 1971, Society of Automotive Engineers (Publisher), 1971, pp. 1-119.

[137] L. M. Gammon, R. D. Briggs, J. M. Packard, K. W. Batson, R. Boyer, C. W. Domby: Metallography and microstructures of titanium and its alloys. ASM Handbook, Vol. 9, 2004, pp. 899-917.

[138] A. Amanov, S. Sasaki: Frictional behavior of duplex nano-corrugated and nanostructured cu alloy produced by UNSM. Procedia Engineering, Vol. 68, 2013, pp. 491–496.

[139] A. Amanov, I. S. Cho, D. E. Kim: Effectiveness of high-frequency ultrasonic peening treatment on the tribological characteristics of Cu-based sintered materials on steel substrate. Materials and Design, Vol. 45, 2013, pp. 118–124.

[140] N. Al-Aqeeli, K. Abdullahi, A. S. Hakeem, C. Suryanarayana, T. Laoui, S. Nouari: Synthesis, characterisation and mechanical properties of SiC reinforced Al based nanocomposites processed by MA and SPS. Powder Metallurgy, Vol. 56, No. 2, 2013, pp. 149–157.

[141] N. Al-Aqeeli, K. Abdullahi, C. Suryanarayana, T. Laoui, S. Nouari: Structure of mechanically milled CNT-reinforced Al-alloy nanocomposites. Materials and Manufacturing Processes, Vol. 28, No. 9, 2013, pp. 984–990.

[142] K. Abdullahi, N. Al-Aqeeli: Mechanical alloying and spark plasma sintering of nano-SiC reinforced Al–12Si–0.3Mg Alloy. Arabian Journal of Science and Engineering, Vol. 39, No. 4, 2014, pp. 3161–3168.

[143] I. A. Chou, H. M. Chan M. P. Harmer: Machining induced surface residual stress behavior in Al_2O_3-SiC nanocomposites. Journal of the American Ceramic Society, Vol. 79, 1996, pp. 2403–2409.

[144] A. Amanov, I. S. Cho, Y. S. Pyoun, C. S. Lee, I. G. Park: Micro-dimpled surface by ultrasonic nanocrystal surface modification and its tribological effects. Wear, Vol. 286–287, 2012, pp. 136–144.

148

[145] A. Amanov, Y. S. Pyoun, I. S. Cho, C. S. Lee, I. G. Park: The evaluation of the micro-tracks and micro-dimples on the tribological characteristics of thrust ball bearings. Journal of Nanoscience and Nanotechnology, Vol. 11, 2011, pp. 701–705.

[146] Y. Zaden, V. Songmene, R. Khettabi, J. Masounave: Surface integrity of Al6061-T6 drilled in wet, semi-wet and dry conditions. In Proceedings of the 37th International MATADOR Conference, Manchester, UK, July 25-27th, 2012, pp. 131–134.

[147] N. Yasugahira, K. Namura, R. Kaneko, T. Satoh: Erosion resistance of titanium alloys for steam turbines blades as measured by water droplet impingement. In Titanium Steam Turbine Blading, PaloAlto, 2988, Pergamo, New York., 1990, pp. 385–401.

[148] A. K. Gujba, Z. Ren, Y. Dong, C. Ye, M. Medraj: Effect of ultrasonic nanocrystalline surface modification on the water droplet erosion performance of Ti-6Al-4V. Surface & Coatings Technology (accepted for publication), 2016.

[149] I. Altenberger, R. K. Nalla, Y. Sano, L. Wagner, R. O. Ritchie: On the effect of deep-rolling and laser-peening on the stress-controlled low- and high-cycle fatigue behavior of Ti–6Al–4V at elevated temperatures up to 550°C. International Journal of Fatigue, Vol. 44, 2012, pp. 292–302.

[150] K. K. Liu, M. R. Hill: The effects of laser peening and shot peening on fretting fatigue in Ti–6Al–4V coupons. Tribology International, Vol. 42, No. 9, 2009, pp. 1250–1262.

[151] Y. K. Gao: Improvement of fatigue property in 7050–T7451 aluminum alloy by laser peening and shot peening. Materials Science and Engineering A, Vol. 528, No. 10–11, 2011, pp. 3823–3828.

[152] S. Zabeen, M. Preuss, P. J. Withers. Residual stresses caused by head-on and 45° foreign object damage for a laser shock peened Ti–6Al–4V alloy aerofoil. Materials Science and Engineering A, Vol. 560, 2013, pp. 518–527.

[153] B. Lin, C. Lupton, S. Spanrad, J. Schofield, J. Tong: Fatigue crack growth in laser-shock-peened Ti–6Al–4V aerofoil specimens due to foreign object damage. International Journal of Fatigue, Vol. 59, 2014, pp. 23–33.

[154] M. J. Shepard, P. R. Smith, M. S. Amer: Introduction of compressive residual stresses in Ti-6Al-4V simulated airfoils via laser shock processing. Journal of Materials Engineering and Performance, Vol. 10, No. 6, 2001, pp. 670–678.

[155] E. Zolotoyabko, J. L. M. Rupp, L. J. Gauckler: Interrelationship between grain size-induced and strain-induced broadening of X-ray diffraction profiles: What we can learn about nanostructured materials?. Scripta Materialia, Vol. 66, No. 3–4, 2012, pp. 190–193.

[156] P. Peyre, R. Fabbro, P. Merrien, H. Lieurade: Laser shock processing of aluminium alloys. Application to high cycle fatigue behaviour. Materials Science and Engineering A, Vol. 210, 1996, pp. 102–113.

[157] P. Peyre, A. Sollier, I. Chaieb, L. Berthe, E. Bartnicki, C. Braham, R. Fabbro: FEM simulation of residual stresses induced by laser Peening. The European Physical Journal Applied Physics, Vol. 88, 2003, pp. 83–88.

[158] P. Prevey: Current applications of X-ray diffraction residual stress measurement. Developments in Materials Characterization Technologies - ASM International, Materials Park, OH, 1996, pp. 103-110.

[159] L. Hackel, S. Marley, A. Rubenchik: Reduction of cavitation erosion by laser peening. SNAME Annual Maritime Convention (SMC) Houston, TX, United States, October 22-24th, 2014, pp. 1-10.

[160] G. Hammersley, L. A. Hackel, F. Harris: Surface prestressing to improve fatigue strength of components by laser shot peening. Optics and Lasers in Engineering, Vol. 34, No. 4–6, 2000, pp. 327–337.

[161] Y. Zhao: Effects of laser shock peening on residual stress, texture and deformation microstructure of Ti-6Al-4V Alloy. PhD Dissertation, University of Cincinnati 2012.

[162] O. Hatamleh: The effects of laser peening and shot peening on mechanical properties in friction stir welded 7075-T7351 aluminum. Journal of Materials Engineering and Performance, Vol. 17, No. 281, 2008, pp. 688–694.

[163] J. Chávez, E. Rodríguez, M. Flores, J. Ibarra-Montalvo, O. Jiménez, G. Gómez-Rosas: On the properties and resistance to abrasive wear of surface-modified Ti-6Al-4V alloy by laser shock processing. Superficies y Vacio, Vol. 27, No. 2, 2014, pp. 54–60.

[164] C. Cellard, D. Retraint, M. François, E. Rouhaud, D. Le Saunier: Laser shock peening of Ti-17 titanium alloy: Influence of process parameters. Materials Science and Engineering A, Vol. 532, 2012, pp. 362–372.

[165] E. V. Petunlna, V. L. Poplayskaya: Strength increase of titanium-base alloys by cold working. Metal Science and Heat Treatment of Metals, Vol. 1, No. 10, 1959, pp. 24–27.

[166] S. Nagarjuna, K. Balasubramanian, D. S. Sarma: Effect of prior cold work on mechanical properties and structure of an age-hardened Cu-1.5wt % Ti alloy. Journal of Materials Science Vol. 2, No. 32, 1997, pp. 3375–3385.

[167] B. Baufeld, O. Van der Biest: Mechanical properties of Ti-6Al-4V specimens produced by shaped metal deposition. Science and Technology Of Advanced Materials, Vol. 10, 2009, pp. 1–10.

[168] R. K. Gupta, V. A. Kumar, C. Mathew, G. S. Rao: Strain hardening of Titanium alloy Ti-6Al-4V sheets with prior heat treatment and cold working. Materials Science and Engineering A, Vol. 662, 2016, pp. 537–550.

[169] C. Ye, Y. Liao, G. J. Cheng: Warm laser shock peening driven nanostructures and their effects on fatigue performance in aluminium alloy 6160. Advanced Engineering Materials, Vol. 12, No. 4, pp. 291-297, 2010.

[170] Y. Liao, S. Suslov, C. Ye, G. Cheng: The mechanisms of thermal engineered laser shock peening for enhanced fatigue performance. Acta Materialia, Vol. 60, No. 13–14, 2012, pp. 4997–5009.

[171] R. Rhode, J. Johnson: Dynamic deformation twinning in shock loaded iron. Journal of Applied Physics, Vol. 42, 1971, pp. 4171–4182.

[172] Laser Research Center, Lidaris Ltd, Vilnius University: http://lidaris.com/glossary-2/fluence/. 2013, assesed on Oct. 10, 2013.

[173] C. Yang, P. D. Hodgson, Q. Liu, L. Ye: Geometrical effects on residual stresses in 7050-T7451 aluminum alloy rods subject to laser shock peening. Journal of Materials Processing Technology, Vol. 201, No. 1–3, 2008, pp.303–309.

[174] Z. Hong, Y. Chengye: Laser shock processing of 2024-T62 aluminum alloy. Materials Science and Engineering A, Vol. 257, No. 2, 1998, pp. 322–327.

[175] C. Zi-Wen, C. Zhi-Gang, Z. Shi-Kun, F. Qun-Xing: Numerical simulation of residual stress field induced by laser shock processing with square spot. Journal of Shanghai University, Vol. 15, No. 9140, 2011, pp. 553–556.

[176] M. P. Sealy, Y. B. Guo: Surface integrity and process mechanics of laser shock peening of novel biodegradable magnesium-calcium (Mg-Ca) alloy. Journal of the Mechanical Behaviour of Biomedical Materials, Vol. 3, No. 7, 2010, pp. 488–496.

[177] C. Bolis, L. Berthe, M. Boustie, M. Arrigoni, S. Barradas, M. Jeandin: Physical approach to adhesion testing using laser-driven shock waves. Journal of Physics D: Applied Physics, Vol. 40, No. 10, 2007, pp. 3155–3163.

Appendices

Appendices contain additional information about different sections of this thesis. The appendices are divided into four, Appendix A, B, C and D. The following sections discuss each appendix.

<u>Appendix A</u>

Appendix A contains additional information about the LSP process parameters and equations used by different authors. Table A-1 summarizes these equations for instance; power density is expressed as a function of frequency, pulse time, power and spot area as given in Equation (1). Other parameters are the laser fluence as given in Equation (2), the load or pressure (P), which must exceed the dynamic yield strength for plastic deformation given by different authors in Equations (3)–(9). Equation (10) shows the reduced shock impedance (Z) for the target material (Z_1) and confining medium (Z_2) which is related to the density and speed of sound in the material. Table A-2 lists typical values of acoustic shock impedance for various confining media and target materials. Furthermore, Equation (11) shows the Hugoniot Elastic Limit (*HEL*), which is the ultimate stress a material can withstand under compression without internal rearrangement [171]. The process optimization could be more complicated especially when many parameters are involved. For instance, shock pressure representation was inconsistent as found in the literature. Equations (3)–(9) indicate how the constants were varied based on the experimental observations. The variations of constants were attributed to the type of coating, confining medium and target material properties. This suggests that selecting the most effective processing parameters is paramount.

Table A-1: Summary of laser processing equations used by different authors

Equation No.	Parameter	Equation	Ref.
1	Intensity	$I\left(\dfrac{GW}{cm^2}\right) = \dfrac{P_{avg}}{f\,(pt)\,a}$	[59]
2	Laser Fluence	$Fluence\left(\dfrac{J}{cm^2}\right) = \dfrac{Laser\ pulse\ energy\ (J)}{focal\ spot\ area\ (cm^2)}$	[172]
3	Pressure	$P = A\left(\dfrac{\alpha}{2\alpha + 3}\right)^{1/2} Z^{1/2}I^{1/2}$	[55]
4	Pressure	$P(GPa) = 0.01\left(\dfrac{\alpha}{2\alpha + 3}\right)^{1/2} Z^{1/2}I^{1/2}$	[156,173]
5	Pressure	$P(GPa) = 1.02I^{1/2}$	[156,173]
6	Pressure	$P(Pa) = 0.25(IMA)^{1/2}$	[174]
7	Pressure	$P = 5.47\left(\dfrac{\alpha}{2\alpha + 3}\right)^{1/2} I^{1/2}$	[175]
8	Pressure	$P\,(kbar) = BI^{1/2}$	[55]
9	Pressure	$P = (AZI)^{1/2}$	[72]
10	Reduced Impedance	$\dfrac{2}{Z} = \dfrac{1}{Z_1} + \dfrac{1}{Z_2}$	[173]
11	Hugoniot Elastic Limit	$HEL = \dfrac{1 - \vartheta}{1 - 2\vartheta}\sigma_y^{dyn}$	[173]

Where, I is the laser power density in GW/cm^2, P_{avg} is the average power output in W, f is the laser frequency in Hz, pt is the pulse time in ns, a is the laser spot area in cm^2, B is 21 or 10.1 for glass- or water-confined modes, respectively, A is absorption coefficient for surface coating, M is transmission coefficient for transparent overlay, α is the ratio of thermal to internal energy, Z, is the reduced shock impedance of the target material and confinement medium, ϑ is Poisson's ratio, σ_y^{dyn} is the dynamic yield strength at high strains.

Table A-2: Typical values of Z_1 and Z_2 as reported by different authors

Target material	Z_1 x 10^6 (g/cm^{2}s) (Reference)	Confining medium	Z_2 x 10^6 (g/cm^{2}s) (Reference)
Ti-6Al-4V	2.75 [69]	Water	0.17 [69]
AA7050-T7451	1.50 [173]	Perpex	0.32 [68]
SS304	3.61 [81]	Silicon rubber	0.47 [68]
Mg-Ca	0.88 [176]	K9 Glass	1.14 [68], 1.5 [81]
AISI 4140	3.96 [82]	Quartz Glass	1.31 [68]
Cu	0.16 [177]	Pb Glass	1.54 [68]
SS321	4.00 [72]	BK Glass	1.44 [82]

Appendix B

Appendix B contains additional information on the dimensions of sample geometries, T-shaped and airfoil, used for the WDE tests. Figures B-1 and B-2 show the dimensions and typical machined T-shaped flat and airfoils geometries, respectively.
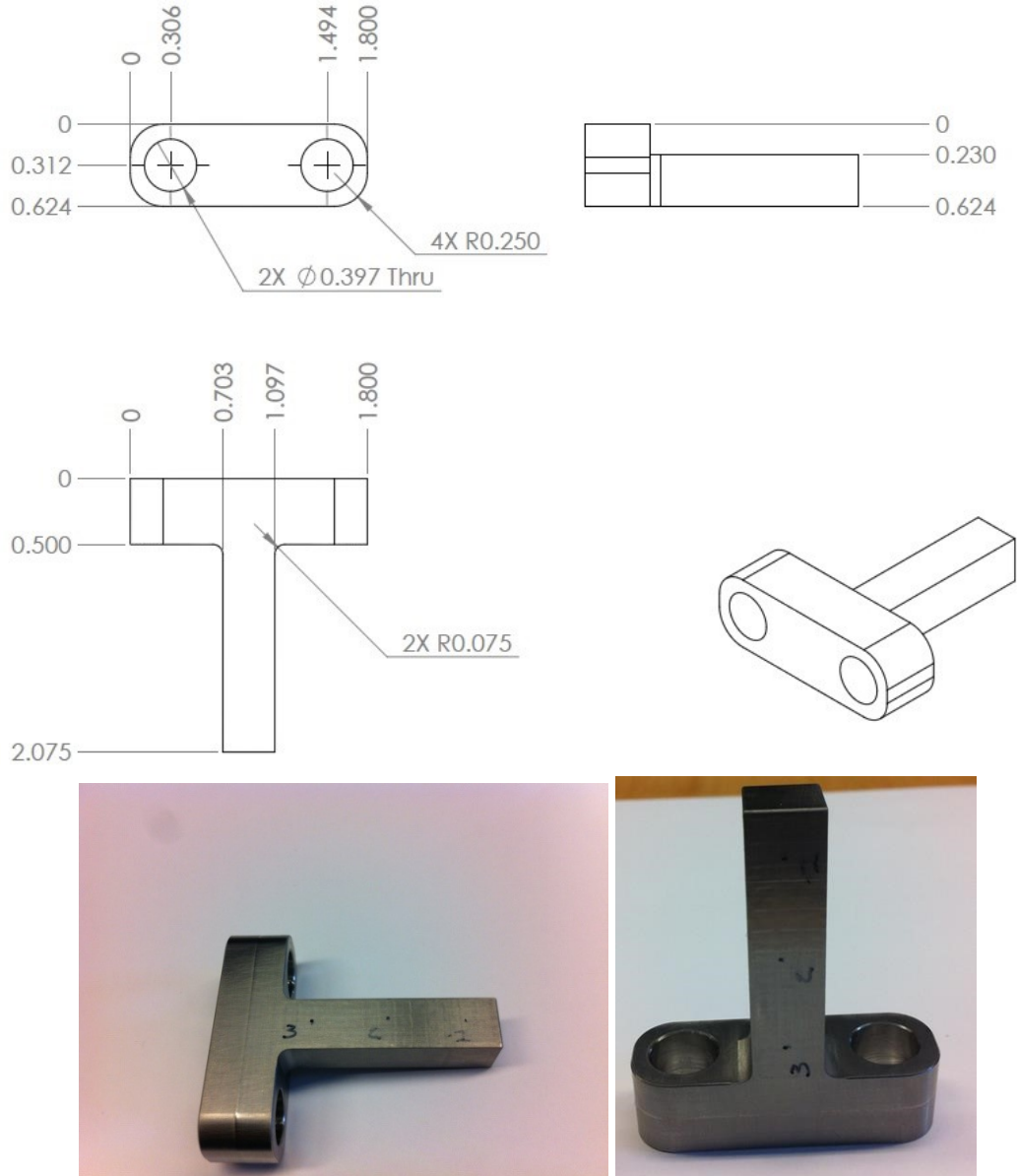

Figure B-1: T-shaped Ti-6Al-4V sample geometry with dimensions in inches.
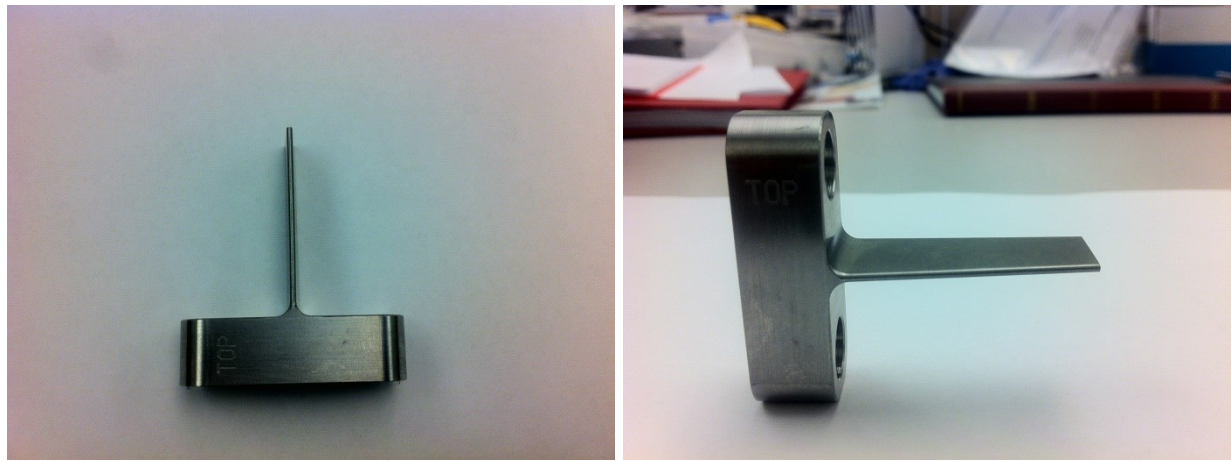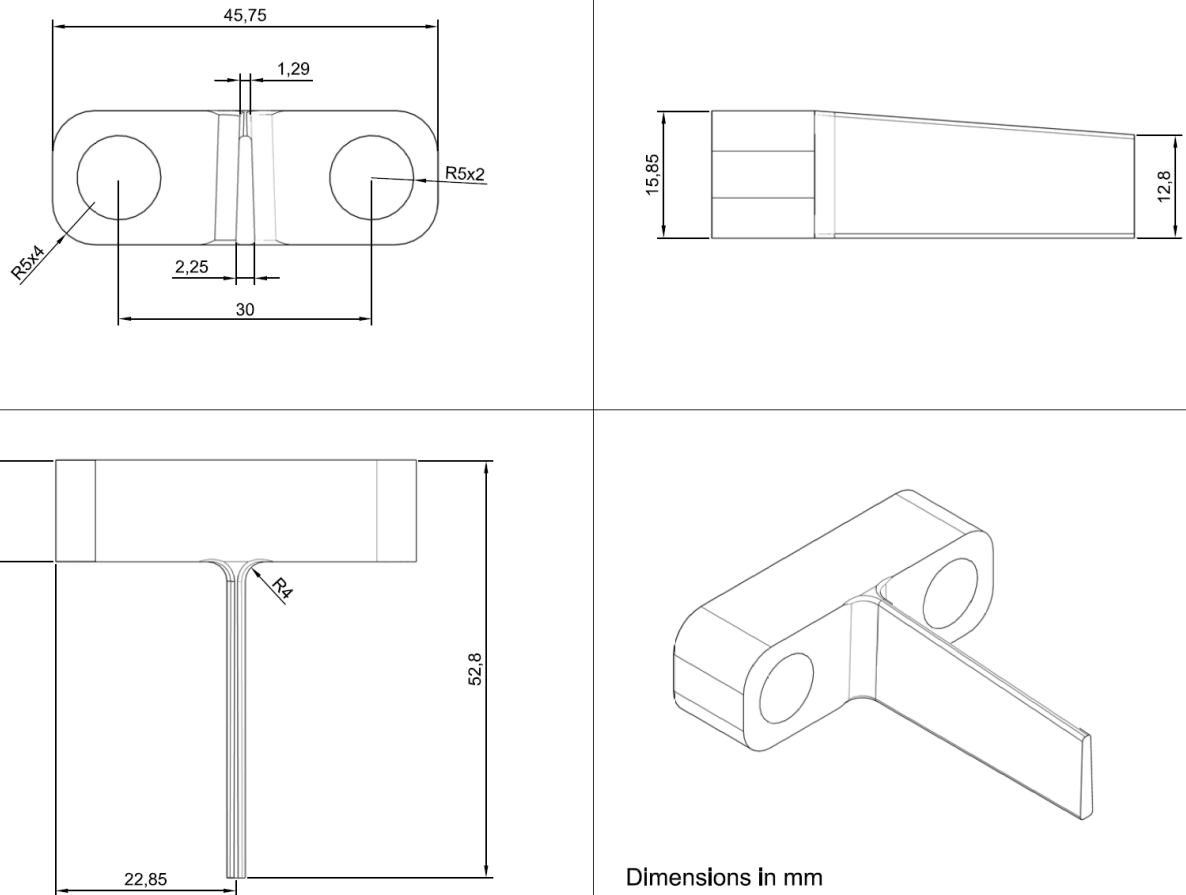
Figure B-2: Airfoil Ti-6Al-4V sample geometry with dimensions in mm.

Appendix C

Appendix C highlights further details on the effect of UNSM process on the WDE performance of Ti-6Al-4V. Results from both sample geometries are presented.

C-1: WDE performance of UNSM and As-M T-shaped sample conditions

Similar to the analyses made in Figure 3-10 (section 3.3.3) and Table 3-4, the influence of impact speed on the erosion crater behaviour of As-M and UNSM was studied. Also, the accumulated material loss, crater width and depth were observed after certain exposure times/number of impingements at different impact speeds. Figure C-1shows the polished cross-sectional views of the As-M and UNSM erosion craters at impact speeds of 250, 300 and 350 m/s halted after 310, 70 and 30 minutes, respectively. Table C-1 shows the accumulated material loss, crater width and depth at various impact speeds. It can be seen from Table C-1 that increasing the impact speed showed significant mass loss and increase in crater dimensions even with fewer number of impingements/exposure time. This trend is in general agreement with the data presented in Table 3.4 which indicates a linear relationship between the impact speed and crater dimension. Comparing the As-M and UNSM conditions, it can be seen that As-M condition showed higher mass losses and crater dimensions. However, at 350 m/s, UNSM condition showed a little deeper crater (Table C-1) than the As-M condition. This might be due to the sectioned area on the UNSM where significant damage had occurred. Nevertheless, the significant mass losses observed at 350 m/s could suggest that the crater dimensions are highly representative. Based on Figure C-1 and Table C-1, it can be confirmed that the UNSM condition had enhanced WDE performance than the As-M condition.

$$186 \times 10^5 \qquad 50.4 \times 10^5 \qquad 25.2 \times 10^5 \text{ Impgmts}$$
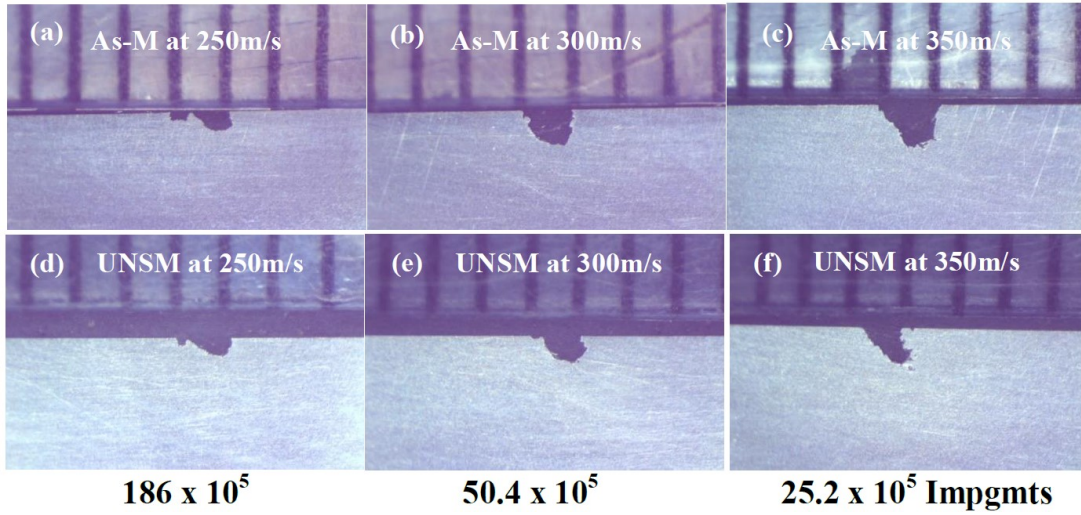
Figure C-1: OM images showing the influence of impact speeds on the As-M and UNSM crater width and depth. The scale shown in each image is in mm.

Table C-1: Summary of the observed accumulated material loss, crater width and depth for As-M and UNSM samples at different speeds

Speed (m/s)	Experiment stopped after		Accumulated mass loss (g)		Crater width (mm)		Crater depth (mm)	
	Time (mins)	N_{imp} x 10^5	As-M	UNSM	As-M	UNSM	As-M	UNSM
250	340	186	0.0170	0.0133	1.33	1.16	0.392	0.360
300	70	50	0.0269	0.0215	1.07	1.07	0.769	0.568
350	30	25	0.0353	0.0320	1.36	0.87	0.841	0.886

C-2: WDE performance of UNSM and As-M airfoil sample conditions

Based on the observed trend in Figure 4-17b (region A), another airfoil sample was UNSM treated. However, in this treatment, the edge of the airfoil was not treated i.e. about 0.5 mm away from the edge was untreated. Figure C-2 shows the WDE performance of the UNSM airfoil without edge treatment *versus* As-M airfoil tested at 300 m/s. It can be seen clearly that not treating the edge of the airfoil proves to be beneficial in mitigating the erosion damage especially at the advanced stages. Region B (Figure C-2a) shows that both UNSM and As-M conditions had

similar erosion behaviour during the early stages. However, after 60 x 10^4 cycles, the UNSM airfoil showed mildly enhanced performance at the advanced stage which confirms the hypothesis observed in Figure 4-17b (Region A). The ER_{inst} graph shown in Figure C-2b also revealed that the UNSM airfoil without edge treatment has slower erosion rates compared to As-M condition. This is due to the fact that compressive residual stresses are through the thickness of the airfoil.
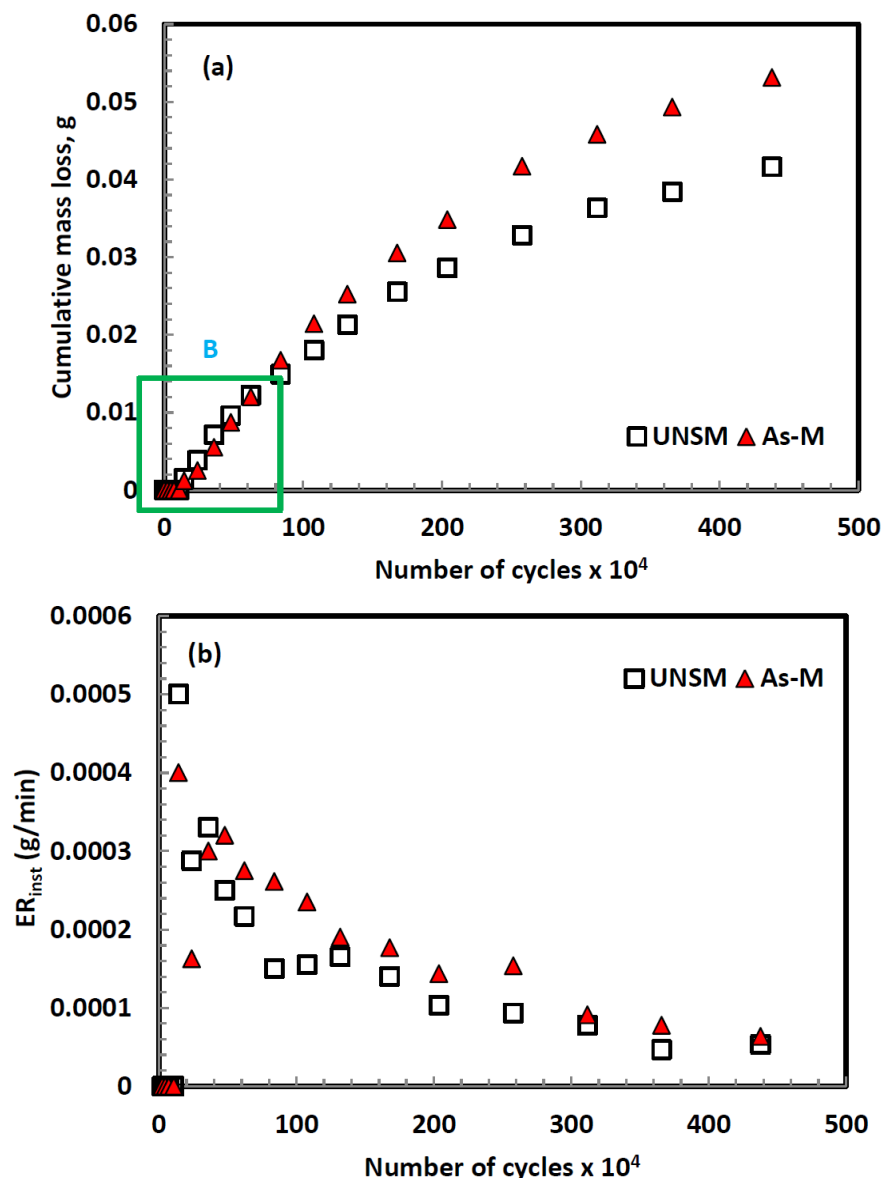

Figure C-2: WDE performance of UNSM airfoil with untreated edge *versus* As-M at 300 m/s.

Figure C-3a shows the macrographs of the UNSM airfoil with the untreated edge, whereas Figure C-3b shows the erosion evolution and progression. However, the macrograph clearly indicates better WDE performance and resistance on the UNSM airfoil as compared with the As-M at advanced stage. This is also consistent with the WDE curves in Figure C-2.
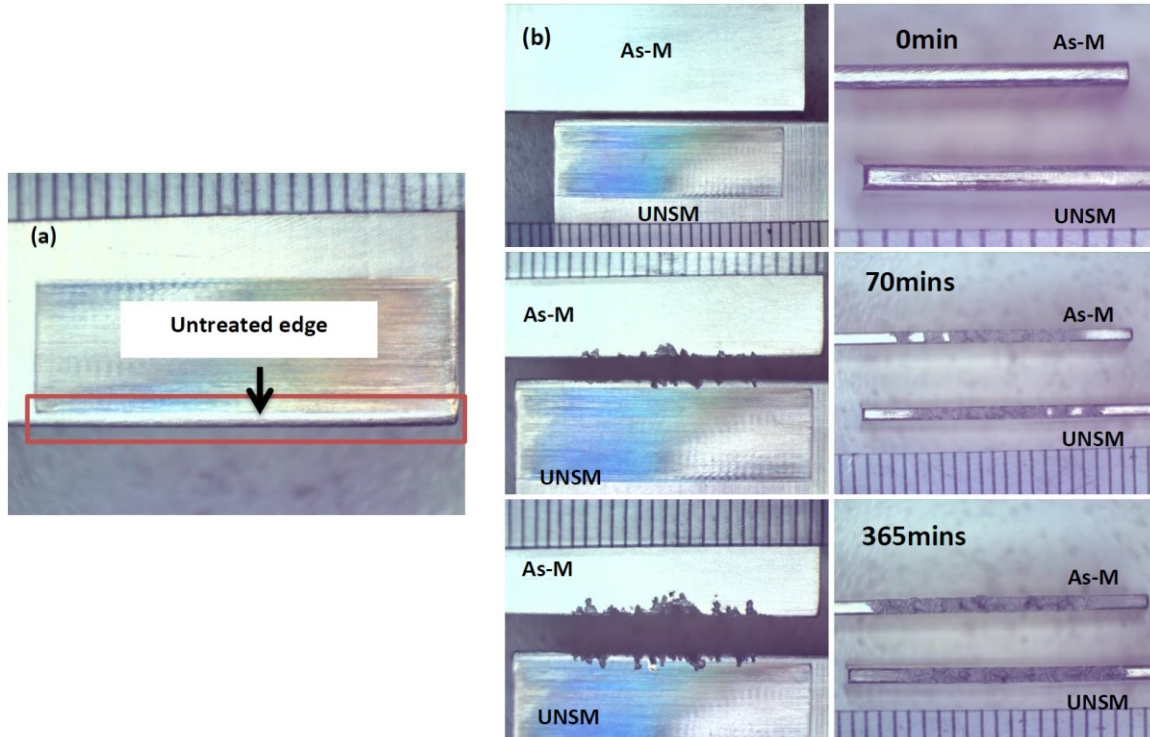

Figure C-3: Optical macrographs showing (a) the untreated airfoil edge and (b) the erosion evolution and progression on As-M and UNSM (with untreated edge) airfoil samples at 300 m/s. The scale shown in each image is in mm.

Appendix D

Appendix C presents additional information regarding the effect of LSP and its attributes on the WDE performance of Ti6Al-4V.

D-1: WDE performance of SR, As-M, SR+LSP and LSP surface conditions

Other surface conditions have been employed during the current research. For instance, stress relieved (SR) and stress relieved plus laser shock peening (SR+LSP) surface conditions were explored. The purpose of having different surface conditions is to have different levels of compressive residual stresses. For the SR condition, As-M sample was heat treated in an oven (Thermolyne Oven model FD1535M) at a temperature of 1100°F (590°C) for 2 hrs. This approach relieved the compressive residual stresses induced during machining. The SR condition showed close to zero compressive residual stress (-29.14±5.8 and -22.2±17.83MPa in the 0° and 90° directions, respectively). For the SR+LSP, SR sample was laser peened using similar LSP parameters mentioned in section 5.2.2. The WDE performance of T-shaped SR *versus* LSP and As-M *versus* SR+LSP was investigated at various impact speeds. Figure D-1a also shows the WDE performance of SR *versus* LSP conditions at 275 and 350 m/s. Again, the influence of the LSP and its attributes on the WDE performance was not observed, thus similar trend was observed as in Figure 5-10. Figure D-1b shows similar WDE behaviour and performance for the SR+LSP and As-M conditions at 250 and 300 m/s. Based on the graphs presented in Figures D-1 and 5-10, the As-M, LSP, SR and SR+LSP conditions had similar WDE performance irrespective of the test condition for the T-shaped sample.
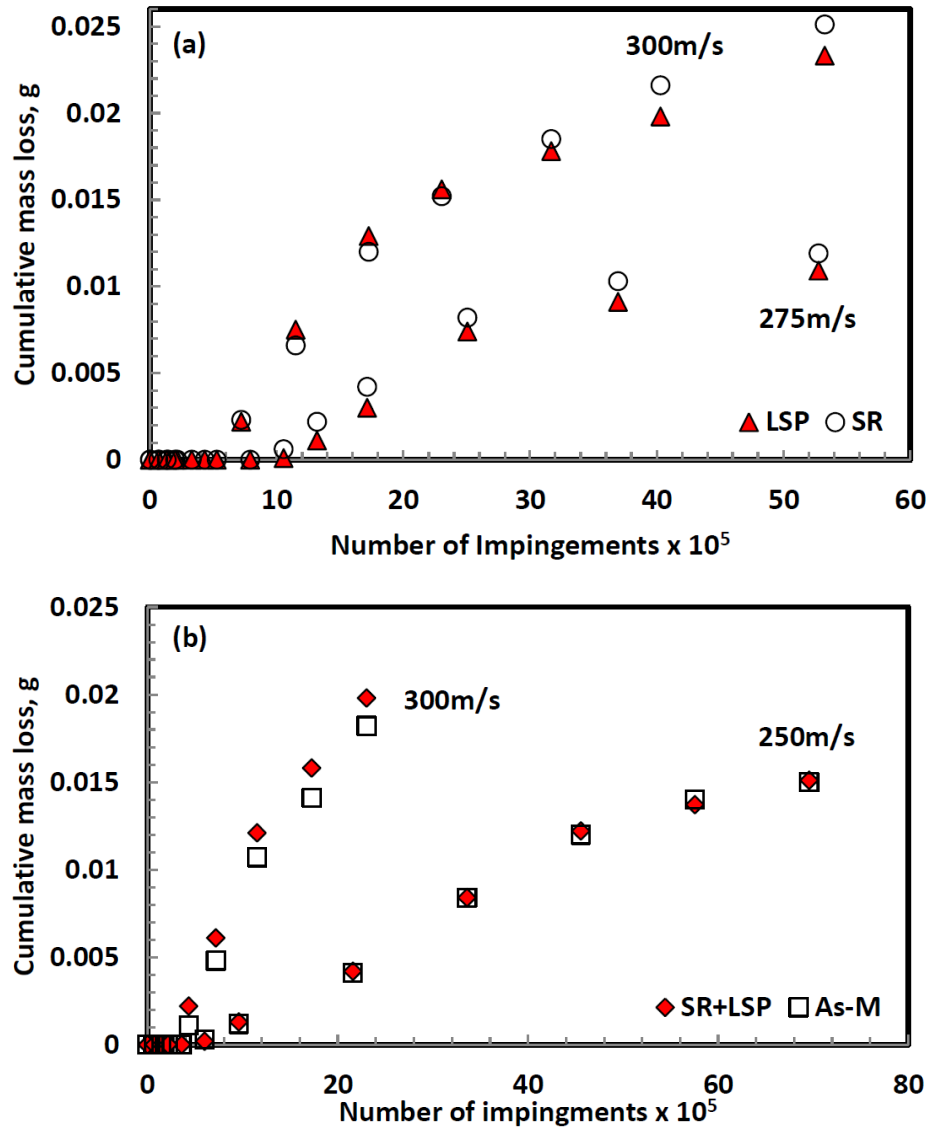
Figure D-1: WDE curves for (a) SR *versus* LSP at 275 m/s and 300 m/s and (b) SR+LSP *versus* As-M at 250 m/s and 300 m/s.

Also, another laser peening test was also conducted with a low energy laser at The University of Akron, Ohio, USA. Parameters used are; Nd:YAG laser, Aluminum, Glass, 4 GW/cm^2, 5 ns and 75 % overlapping. The peened sample was WDE tested against As-M condition at 300 m/s using 463 μm droplet size. Figure D-2 shows the WDE curve and it can be seen that similar WDE performance was observed for both conditions at all stages of the erosion. The little difference observed in the graphs is considered within the experimental errors.
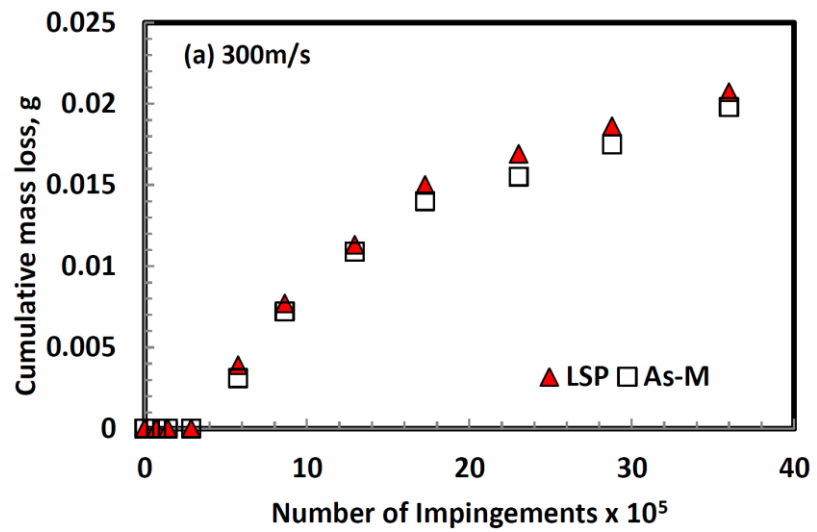
Figure D-2: WDE curve for As-M *versus* LSP conditions at 300 m/s. LSP treatment with low energy laser.